



UNIVERSITY OF  
BATH

**The Smart Lacrosse Ball – Position Tracking Proof-of-Concept Design**

Sebastian Di Siena

Student Number: 189250261

MEng Integrated Mechanical and Electrical Engineering

MEng Final Project Report

Academic Year: 2022/23

Supervisor: Dr Jonathan Graham-Harper-Cater

Assessor: Nick Evans

**Number of Words: 11590**

## Abstract

---

During the period of 1980 to 2008 10 deaths have been recorded due to commotio cordis caused by blunt trauma from a lacrosse ball, where 4 cases included goalkeepers who were wearing commercially available chest protection. Moreover, among 20 high school sports, women's lacrosse exhibited the highest concussion rate, with 72.7% (2008-2019) of concussions caused by ball or stick contact. To safeguard players and mitigate the risk of fatal incidents and long-term injuries, data specific to the lacrosse ball can inform lacrosse protection manufacturers to aid with the development of protective and preventative measures within the sport.

To acquire this data, this report proposes a proof-of-concept design to extract information from a lacrosse ball in practice, more specifically, a position tracking system. This design incorporates an Inertial Measurement Unit (IMU) and Ultra-Wide Band (UWB) sensor to locate the system in 3-Dimension (3-D) space. Using a method that determines the orientation of the system, the acceleration can be referenced to the global coordinate system to derive the 3-D position. The sensors selected utilise dead reckoning (IMU) and trilateration (UWB) methods to localise the position of the system in 3-D space.

Results demonstrated the system's swift response to any changes in orientation and produced an average absolute error of  $1.35^\circ$  in roll, pitch, and yaw when performing accuracy testing. This system performed reliably when determining orientation, remaining unaffected to vibrations, electromagnetic interference and drift in the output data, which are common issues with IMUs. Position testing revealed that the systems maximum Y and Z values closely matched the maximum tested values, with the X position value reading approximately 10cm greater. However, calibration issues with the IMU sensor effected the system's sensitivity with the detection in the nuances in the actual 3-D trajectory.

## Acknowledgements

---

First and foremost, I would like to thank my project supervisor, Dr. Jonathan Graham-Harper-Cater, for allowing me to pursue this 'student-initiated project', and for his invaluable guidance and support throughout.

I am also indebted to my family for their unwavering support and motivation throughout my entire academic career. Their belief in my ability has been a driving force behind my pursuit of success, and I owe everything to them.

Lastly, I would like to extend my appreciation to my colleagues who have accompanied me on this university journey at Bath. You have all made this entire experience not only educational, but also immensely enjoyable.

# Contents

---

<b>Abstract</b>	<b>2</b>
<b>Acknowledgements</b>	<b>3</b>
<b>List of Figures</b>	<b>5</b>
<b>List of Tables</b>	<b>7</b>
<b>List of Equations</b>	<b>9</b>
<b>List of Acronyms</b>	<b>10</b>
<b>1 Introduction</b>	<b>12</b>
1.1 Data Collection in Sports . . . . .	12
1.1.1 Tennis - Hawk-Eye . . . . .	12
1.1.2 Rugby Union - Catapult . . . . .	12
1.1.3 Football - KINEXON . . . . .	12
1.2 Project Overview . . . . .	12
1.3 Project Aims and Objectives . . . . .	14
1.4 Report Layout . . . . .	14
1.5 Background Knowledge . . . . .	15
1.5.1 Dead Reckoning . . . . .	15
1.5.2 Trilateration . . . . .	15
1.6 Relevant Literature . . . . .	16
1.6.1 Camera Detection . . . . .	16
1.6.2 Inertial Measurement Unit (IMU) . . . . .	16
1.6.3 GPS . . . . .	17
1.6.4 Ultra-Wide Band (UWB) . . . . .	17
1.6.5 Optimal Solution . . . . .	18
<b>2 Microcontroller and Design Environment Selection</b>	<b>19</b>
2.1 Design Environment Selection . . . . .	19
<b>3 Onboard IMU - Dead Reckoning Method</b>	<b>20</b>
3.1 IMU Functionality . . . . .	20
3.1.1 MEMS Gyroscope . . . . .	20
3.1.2 MEMS Accelerometer . . . . .	20
3.1.3 MEMS Magnetometer . . . . .	21
3.2 IMU Selection . . . . .	22
3.3 IMU Setup . . . . .	22
3.3.1 IMU Calibration . . . . .	23
3.4 IMU Position Detection Algorithm . . . . .	24
3.4.1 Euler Rotation Matrix Method . . . . .	25
3.4.2 Quaternion Rotation Matrix Method . . . . .	26
3.5 IMU Live Orientation . . . . .	26
3.5.1 Accelerometer Data . . . . .	26
3.5.2 Gyroscope Data . . . . .	27
3.5.3 Magnetometer Data . . . . .	27
3.5.4 Complementary Filters . . . . .	27
3.5.5 Quaternion Data . . . . .	28
3.6 Onboard IMU Testing Plan . . . . .	29
3.6.1 Calibration Testing Plan . . . . .	29

3.6.2	Orientation Testing Plans . . . . .	29
3.6.3	Position Testing Plans . . . . .	30
<b>4</b>	<b>UWB Module - Trilateration Method</b>	<b>32</b>
4.1	ToF Methods . . . . .	32
4.1.1	One-Way Ranging . . . . .	32
4.1.2	TWR . . . . .	32
4.2	Trilateration . . . . .	33
4.2.1	Localisation in 2-Dimension (2-D) . . . . .	33
4.2.2	Localisation in 3-D . . . . .	35
4.3	UWB System Design . . . . .	35
4.3.1	UWB Selection . . . . .	36
4.3.2	DWM3000 Selection . . . . .	37
4.3.3	UWB Setup . . . . .	38
4.3.4	UWB Testing . . . . .	39
<b>5</b>	<b>Results</b>	<b>40</b>
5.1	Onboard IMU Calibration Results . . . . .	40
5.2	Onboard IMU Orientation Results . . . . .	40
5.2.1	Accelerometer Orientation Results . . . . .	40
5.2.2	Gyroscope Orientation Results . . . . .	44
5.2.3	Magnetometer Orientation Results . . . . .	47
5.2.4	Complementary Filter Orientation Results . . . . .	50
5.2.5	Quaternion Orientation Results . . . . .	54
5.3	Onboard IMU Position Results . . . . .	59
5.3.1	Euler and Quaternion Rotation Matrix Position Results . . . . .	59
<b>6</b>	<b>Discussion</b>	<b>60</b>
6.1	IMU Orientation Results . . . . .	60
6.1.1	Accelerometer Orientation Results . . . . .	60
6.1.2	Gyroscope Orientation Results . . . . .	60
6.1.3	Magnetometer Orientation Results . . . . .	60
6.1.4	Complementary Filter Orientation Result . . . . .	60
6.1.5	Quaternion Orientation Results . . . . .	61
6.2	IMU Position Results . . . . .	61
6.3	Testing Setup . . . . .	62
6.4	Project Aims and Objectives . . . . .	62
<b>7</b>	<b>Conclusion and Future Work</b>	<b>63</b>
7.1	Conclusion . . . . .	63
7.2	Future Work . . . . .	63
<b>Bibliography</b>		<b>64</b>
<b>Appendix</b>		<b>68</b>

## List of Figures

---

1.1	Lacrosse player, Lyle Thompson, scoring against the Waterdogs Lacrosse Club [6] . . . . .	13
1.2	Standard 'radar gun' currently used to determine shot speed [9] . . . . .	13
1.3	Visualisation of drift error in dead reckoning solution for aviation applications [10] . . . . .	15
1.4	The working principle of trilateration in two dimensions. Knowing the distances from three different reference points (V1, V2, V3) with known coordinates it is possible to localize the position of an unknown point on the intersection of three circumferences [11]	16
1.5	Initial proof-of-concept design showing the structure of the system with the UWB and IMU sensors . . . . .	18
2.1	ESP32-S3-DevKitC board with annotations outlining components [20] . . . . .	19
3.1	Bosch BNO055 Intelligent 9-Axis Absolute Sensor system architecture, outlining the communication and separation of each internal sensor [21] . . . . .	20
3.2	MEMS Gyroscope internals and functionality . . . . .	21
3.3	MEMS Accelerometer internals and functionality . . . . .	21
3.4	Illustration of a ferromagnetic MEMS magnetometer design [26] . . . . .	21
3.5	MIKROE BMI270 IMU [27] . . . . .	22
3.6	IMU schematic and physical setup . . . . .	23
3.7	Illustration of the relationship between the local to the global coordinate system. In this case the object with the North-East-Up axes represents the IMU and the sphere is representing the global coordinate system [29] . . . . .	24
3.8	Illustration of the live position detection method used within the IMU section of the design . . . . .	25
3.9	Basic example of a complementary filter that attenuates high and low-frequency noise from 2 inputs ( $x_1$ and $x_2$ ) to produce a clean output signal ( $x$ ) . . . . .	28
3.10	Live orientation calculation through complementary filter implementation . . . . .	28
3.11	Orientation testing setup example where the IMU is pitched at 90° . . . . .	30
3.12	Position testing setup to measure the IMU's position in 3-D space (30cmx30cmx30cm area) . . . . .	31
4.1	Single and Double-Sided TWR Systems . . . . .	33
4.2	2-D localisation with numerous ANs . . . . .	34
4.3	Proof-of-concept design for the UWB subsystem outlining locations of the ANs around the lacrosse field to localise the lacrosse ball (tag) in 3-D space, illustrating the setup in practice . . . . .	36
4.4	Makerfabs' ESP32 UWB DW3000(Ultra Wideband) device [47] . . . . .	37
4.5	Mikroelektronika's UWB Click [49] . . . . .	37
4.6	Schematic diagrams for the AN and tag for proof-of-concept system . . . . .	38
4.7	Physical setup of the DWM3000EVB using the SPI protocol . . . . .	38
5.1	IMU calibration values when following the calibration testing plan outlined in table 7.2	40
5.2	Roll (red) and pitch (blue) outputs from accelerometer data. IMU was rolled and pitched to 90° and -90° and vibrated to show the effects of noise with the results . . . . .	41
5.3	IMU rolled (red) and pitched (blue) to 90° and -90° rapidly to test the response of the accelerometer . . . . .	41
5.4	Raw pitch (red) and filtered pitch (blue) values from the accelerometer showing the effectiveness of a low-pass filter on the orientation data. IMU was pitched from 90° to -90° range and vibrated to show how the filtering improves the stability of the output . . . . .	42
5.5	Raw roll (red) and filtered roll (blue) values from the accelerometer showing the effectiveness of a low-pass filter on the orientation data. IMU rolled from 90° to -90° range and vibrated to show how the filtering improves the stability of the output . . . . .	42
5.6	Error in recorded pitch and roll from IMU accelerometer . . . . .	43
5.7	IMU accelerometer pitch. First two peaks are in the range from an actual pitch of 0° to 180 degrees° and the second two peaks are in the range from an actual pitch of 0° to -180° . . . . .	44

5.8	Raw pitch output from the gyroscope data. IMU was pitched within the -180° and 180° range, followed by quick adjustments to the IMU pitch to determine the response speed	44
5.9	Raw roll output from the gyroscope data. IMU was rolled within the -180° and 180° range, followed by quick adjustments to the IMU roll to determine the response speed	45
5.10	Raw yaw output from the gyroscope data. IMU was yawed within the -180° and 180° range, followed by quick adjustments to the IMU yaw to determine the response speed	45
5.11	IMU subjected to sudden changes in IMU orientation to observe the effect of gyroscopic drift on the output orientation data . . . . .	46
5.12	Error in recorded pitch, roll, and yaw from IMU gyroscope . . . . .	47
5.13	Magnetometer and gyroscope combination to calculate IMU yaw values. IMU was yawed within the -180° and 180° range, followed by quick adjustments to the IMU yaw to determine the response speed . . . . .	48
5.14	Magnetometer and gyroscope combination displaying the effect of roll and pitch on the yaw output . . . . .	48
5.15	Magnetometer and gyroscope combination displaying the effect of electromagnetic interference on the yaw output . . . . .	49
5.16	Average absolute error of 2.03° for the magnetometer and gyroscope combination to calculate IMU yaw . . . . .	49
5.17	Complementary filter orientation results for roll, pitch, and yaw in the 180° and -180° range. Results to also show the effectiveness of the design against sources of error within the IMU sensor . . . . .	50
5.18	Error in recorded pitch and roll from IMU complementary filter . . . . .	51
5.19	Live animation of numerous 3-D orientation plots from the complementary filter method (transparent axes are the reference axes for orientation adjustments) . . . . .	52
5.20	Pitch calculated from quaternion data. First positive and negative peaks are at an actual pitch of 90°and -90°. The following sets of peaks are within the range of 180° to -180° . . . . .	54
5.21	Pitch calculated from the quaternion data following instantaneous changes to IMU pitch within the range of 90° and -90° . . . . .	54
5.22	Roll calculated from quaternion data. First positive and negative peaks are at an actual roll of 90°and -90°. The following sets of peaks are within the range of 180° to -180° . . . . .	55
5.23	Roll calculated from the quaternion data following instantaneous changes to IMU Roll within the range of 180° and -180° . . . . .	55
5.24	Yaw calculated from quaternion data. First positive and negative peaks are at an actual yaw of 90°and -90°. The following sets of peaks are within the range of 180° to -180° . . . . .	56
5.25	Yaw calculated from the quaternion data following instantaneous changes to IMU yaw within the range of 90° and -90° . . . . .	56
5.26	Error in recorded pitch and roll from IMU quaternions . . . . .	57
5.27	Live animation of numerous 3-D orientation plots from the quaternion method (transparent axes are the reference axes for orientation adjustments) . . . . .	58
5.28	Euler Position Testing: 30cmx30cmx30cm . . . . .	59
5.29	Quaternion Position Testing: 30cmx30cmx30cm . . . . .	59
6.1	IMU accelerometer and system calibration values during the position testing using the quaternion data . . . . .	61

## List of Tables

---

1.1	Project aims and objectives . . . . .	14
4.1	Comparison of main UWB system manufacturers to support with UWB selection [44]	36
6.1	Review of project aims and objectives . . . . .	62
8.1	Testing Plans . . . . .	68
8.2	IMU Accelerometer Testing Plan . . . . .	69
8.3	IMU Gyroscope Testing Plan . . . . .	70
8.4	IMU Magnetometer Testing Plan . . . . .	71
8.5	IMU Complementary Filter Testing Plan . . . . .	72
8.6	IMU Quaternion Testing Plan . . . . .	73
8.7	IMU Position Testing Plan . . . . .	74
8.8	IMU Position Testing Plan . . . . .	75
8.9	Project Costing Table . . . . .	76

## List of Equations

---

- Equation (3.1): Equations of motion: acceleration equation
- Equation (3.2): Equations of motion: velocity equation
- Equation (3.3): Equations of motion: displacement equation
- Equation (3.4): Rotation matrix for rotation about the X axis
- Equation (3.5): Rotation matrix for rotation about the Y axis
- Equation (3.6): Rotation matrix for rotation about the Z axis
- Equation (3.7): Euler ZYX convention
- Equation (3.8): Euler rotation matrix to convert local to the global coordinate system
- Equation (3.9): Conversion of the local acceleration to global acceleration
- Equation (3.10): Normalised quaternion representation
- Equation (3.11): Quaternion rotation matrix to convert local to the global coordinate system
- Equation (3.12): Roll angle from accelerometer data
- Equation (3.13): Pitch angle from accelerometer data
- Equation (3.14): Roll angle from gyroscope data
- Equation (3.15): Pitch angle from gyroscope data
- Equation (3.16): Yaw angle from gyroscope data
- Equation (3.17): Horizontal X component for the Earth's magnetic field
- Equation (3.18): Horizontal Y component for the Earth's magnetic field
- Equation (3.19): Yaw angle from magnetometer data
- Equation (3.20): Complementary filter used to calculate pitch angles from accelerometer and gyroscope pitch values
- Equation (3.21): Complementary filter used to calculate roll angles from accelerometer and gyroscope roll values
- Equation (3.22): Roll angle conversion from quaternion data
- Equation (3.23): Pitch angle conversion from quaternion data
- Equation (3.24): Yaw angle conversion from quaternion data
- Equation (4.1): Distance calculation using ToF of UWB signal
- Equation (4.2): One-way ranging ToF calculation
- Equation (4.3): Single-sided TWR ToF calculation
- Equation (4.4): Symmetrical double-sided TWR ToF calculation
- Equation (4.5): Asymmetrical double-sided TWR ToF calculation
- Equation (4.6): Equation relating the 2-D position of AN1 to the tag

Equation (4.7): Equation relating the 2-D position of AN2 to the tag

Equation (4.8): Equation relating the 2-D position of AN3 to the tag

Equation (4.9): Supporting equation no.1 with 2-D trilateration position derivation

Equation (4.10): Supporting equation no.2 with 2-D trilateration position derivation

Equation (4.11): Supporting equation no.3 with 2-D trilateration position derivation

Equation (4.12): Supporting equation no.4 with 2-D trilateration position derivation

Equation (4.13): X position of tag in 2-D trilateration

Equation (4.14): Y position of tag in 2-D trilateration

Equation (4.15): X position of tag in 3-D trilateration

Equation (4.16): Y position of tag in 3-D trilateration

Equation (4.17): Z position of tag in 3-D trilateration

Equation (4.18): Supporting equation no.1 with 3-D trilateration position derivation

Equation (4.19): Supporting equation no.2 with 3-D trilateration position derivation

Equation (4.20): Supporting equation no.3 with 3-D trilateration position derivation

## List of Acronyms

---

**2-D** 2-Dimension.

**3-D** 3-Dimension.

**AN** Anchor Node.

**ANs** Anchor Nodes.

**DoF** Degree of Freedom.

**GNSS** Global Navigation Satellite System.

**GPIO** General Purpose Input/Output.

**GPS** Global Positioning System.

**HPF** High-Pass Filter.

**IMU** Inertial Measurement Unit.

**IoT** Internet of Things.

**LPF** Low-Pass Filter.

**LV** Low Voltage.

**MEMS** Micro-electromechanical Systems.

**NCAA** National Collegiate Athletics Association.

**NLL** National Lacrosse League.

**PCB** Printed Circuit Board.

**PCBs** Printed Circuit Boards.

**PLL** Premier Lacrosse League.

**RTK** Real-Time Kinematic Positioning.

**SPI** Serial Peripheral Interface.

**ToF** Time of Flight.

**TWR** Two-Way Rangning.

**UWB** Ultra-Wide Band.

## Introduction

---

### 1.1 Data Collection in Sports

Data in sport is incredibly valuable for teams and individuals to gain a competitive edge over sporting rivals. This data is so significant that the Strategic Market Research LLP have forecast a value of \$16.5 billion by 2030 in the sports analytics market [1]. Such data has a multitude of use cases from performance tracking to fan engagement and sports officiating. Below are some examples of data collection within sports, outlining their specific approaches with achieving similar outcomes to further advance their respective sports.

#### 1.1.1 Tennis - Hawk-Eye

A system used in Tennis is the Hawk-Eye solution which is used to track the trajectory of the ball using 10 high resolution cameras at 60Hz [2] to obtain data on the ball's location, speed, and trajectory. This data is calculated by a centralised system which processes the wealth of images captured. This information is then used to support with the officiating of the matches through line-calling (determines whether the ball is within the boundaries of the court). This data can also be used by coaches and players to analyse performance and indicate areas of improvement from shot speed and spin data alongside the trajectory information. This system also further enhances the viewing experience for fans through providing a unique and informative aspect to the sport, enticing new fans.

#### 1.1.2 Rugby Union - Catapult

Catapult is a Global Positioning System (GPS) technology company who develops wearable devices to be inserted into the back of player's shirts to determine key technical and physical demands on the field. This device can detect scrums, kicks and contact during training and games through bespoke algorithms. This data can inform the coaches and training staff of player load to ensure injuries are avoided, whilst also reviewing effort and fatigue levels to support with player rehabilitation from injuries [3]. Since this device can be inserted into all player shirts, it provides a wealth of information on a player specific basis.

#### 1.1.3 Football - KINEXON

KINEXON uses an ultra-wideband radio frequency and an IMU to produce a smart football which records live position and motion data. Such data allows for the monitoring of player and team performance, whilst improving tactical understanding and supporting with game officiating. This product was implemented into the 2022 Qatar World Cup football displaying the technology's value within sport [4].

### 1.2 Project Overview

Lacrosse, also known as 'the fastest game on two feet', is a culmination of numerous sports such as basketball, ice hockey, and football. Similarly to these sports, the aim is to score more goals than the opposing team by throwing a ball into the opposition's net using a lacrosse stick during the period of the match, as shown in Figure 1.1, where the average shot speed in the men's National Collegiate Athletics Association (NCAA) and professional lacrosse is in excess of  $85 \pm 4$  mph [5].



Figure 1.1: Lacrosse player, Lyle Thompson, scoring against the Waterdogs Lacrosse Club [6]

Recording key metrics from a lacrosse ball can provide substantial insight into data such as ball position, pass and shot distance, ball speed, ball force and shot accuracy throughout the duration of a game and training session. On an individual player basis, data can provide an insight into performance progression across numerous training sessions therefore, influencing training methods and identifying areas which require development. Professional lacrosse leagues, Premier Lacrosse League (PLL) and National Lacrosse League (NLL), can significantly improve viewer engagement with this data by increasing game immersion, similarly to Hawk-Eye's method in tennis through live statistics. Since the game is incredibly fast, newer fans may find the sport hard to follow, so providing the ability to review what has unfolded within a game allows for a better viewer experience. On a team basis, data provides coaching staff on tactic effectiveness, influencing strategies for upcoming matches. To promote health and safety of lacrosse athletes, recording and reviewing the forces players are exposed to by the lacrosse ball allows for the early identification of suspected concussions from ball-to-head impact. Studies have shown that high school women's lacrosse recorded the highest concussion rate compared to 20 other sports, with ball contact accounting for 72.7% of all concussions [7]. In addition, between 1980 and 2008, there were 10 recorded deaths due to commotio cordis caused by blunt trauma from a lacrosse ball [8]. Should such data be made available for lacrosse protection manufacturers, more robust products can be designed to reduce risk of death within the sport.



Figure 1.2: Standard 'radar gun' currently used to determine shot speed [9]

Bespoke methods to obtain and record these metrics are not currently present in the sport of lacrosse. Standard 'radar guns', shown in Figure 1.2, are currently being used to record ball speed by positioning the gun directly behind the centre of the goal. This is a general product that is used for numerous applications, so has inherent issues and limitations when being used within the lacrosse use case.

### 1.3 Project Aims and Objectives

As outlined within 1.2, all key metrics and use cases of data in the sport of lacrosse are reliant and derived from ball positional information. Therefore, this project aims to design and develop a proposed tracking system to record the position of a lacrosse ball in 3-D space. The system aims to function within individual training and in-game environments, and therefore relies on little infrastructure to operate. Once this proof-of-concept design is validated, future work on the packaging of this system within a lacrosse ball can be explored.

Based on this problem statement, the following table (Table 1.1) provides insight into the general project aims and objectives used to determine the success of the proof-of-concept design.

Table 1.1: Project aims and objectives

Aim No.	Name	Description
1	Calibration	System can be calibrated easily during use to ensure output data is correct
2	Data Acquisition	Data is recorded live from the system to provide relevant data with determining position in 3-D space
3	Accuracy	Position data is accurate to $\pm 0.10\text{m}$
4	Reliability	System performs reliably over an extended period with no significant error with the output data
5	Infrastructure	Minimal infrastructure required to allow the system to function and collect relevant data
6	Cost	Project cost remains under the allocated project budget
7	Safety	Use of Low Voltage (LV) across the system to prevent any risk to health

As stated in Table 1.1, the proof-of-concept design is required to determine the ball position in 3-D space whilst remaining accurate and reliable. Since this device will be used in a proximity to players, during operation the system must not risk the safety of others should any issues occur. As this device will function in both individual and group applications, the system must require little infrastructure, to reduce setup time, and overall product cost must be kept to a minimum to ensure for accessibility for both use cases.

### 1.4 Report Layout

This report is split into three further overarching sections following this introduction. The remaining elements of the introduction include the general background knowledge around typical position detection methods, and a literature review to support with the overall system design direction. Following this introduction, the three sections convey the method, system design, results from design validation and testing, and the discussion and conclusion reviewing the design and project success.

**Methods:** This section includes all methodology and decisions associated with this 'proof-of-concept' design. It explores the two methods of position detection used in this design, dead reckoning and trilateration, and proposes solutions for these methods. It further introduces the testing plan used to validate the design and the coding language used to develop the results.

**Results:** Using the proposed design and testing plan, results are presented for each element of the design.

**Discussion, Conclusion and Future Work:** This section reviews the results and the project execution, outlining limitations and areas to improve the design. This is where the results will be reviewed against the project aims, proposing future work and developments to be made.

## 1.5 Background Knowledge

The following, dead reckoning and trilateration, are both general position detection algorithms explored in this report. Below is the background knowledge to understand the functionality and limitations associated with both methods. As the design and method develops in this report, more background knowledge and information are provided and explained.

### 1.5.1 Dead Reckoning

Dead reckoning is a navigation method for a moving object to estimate its current position in space based on the previous recorded positions and velocity vectors over an elapsed period. This method is typically known for the process of deducing a ship's position based on its course and speed at sea.

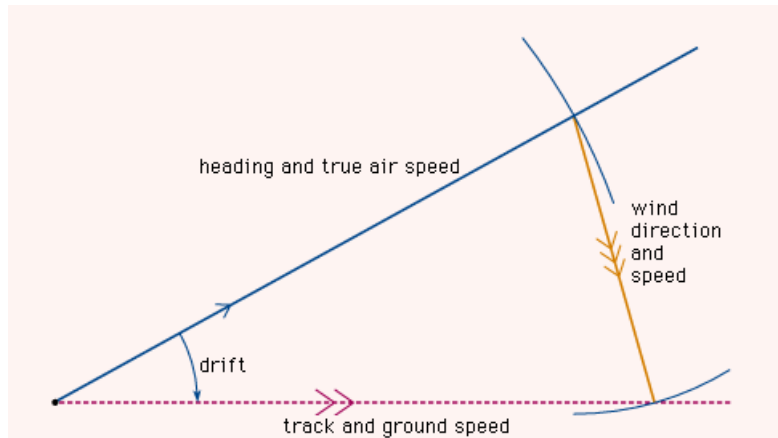


Figure 1.3: Visualisation of drift error in dead reckoning solution for aviation applications [10]

Since this method is reliant on the velocity vector, should either component of the recorded data (magnitude or direction) be slightly inaccurate, over time, numerous data point errors can compound and result in a final position that is highly inaccurate, where this drift error is shown in Figure 1.3. Therefore, to combat this issue, this positioning method should be accompanied alongside another to ensure no positional drift occurs, providing accurate and reliable output data.

### 1.5.2 Trilateration

This method determines the location of an object in space through the measuring of distances between the object and three other known reference points (Figure 1.4). This method is based on the principle that the object must be located at a point which is equidistant from the known reference points. Should the smallest error in reference point locations be present, object position calculations will be inaccurate and incorrect.

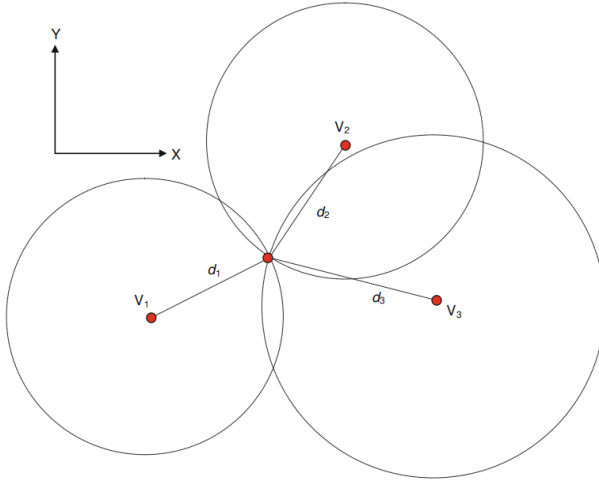


Figure 1.4: The working principle of trilateration in two dimensions. Knowing the distances from three different reference points ( $V_1$ ,  $V_2$ ,  $V_3$ ) with known coordinates it is possible to localize the position of an unknown point on the intersection of three circumferences [11]

## 1.6 Relevant Literature

When reviewing current position detection solutions in literature, the following solutions implement the dead reckoning and trilateration methods previously discussed. With the review of these solutions, alongside the project aims and objectives outlined in 1.3, an optimal solution was selected for this specific design.

### 1.6.1 Camera Detection

Similar to that used in Hawk-Eye's solution for tennis ball data acquisition, 1.1.1, this method determines object position through the analysis of images and video frames obtained by one or more cameras. It assigns objects based on known references and uses the numerous frames to track object displacement.

Research was conducted in 2020 [12] on producing a multi-camera 3-D ball tracking framework for sports video recordings. This research produced accurate 3-D and 2-D ball trajectory data which was robust to environmental interference in basketball. Alongside this, a visual-based localisation system was researched for indoor multi-rotor unmanned aerial vehicles by the University of Padova [13], where the results concluded an error mean of 0.11m, proving to be successful. However, since these tests were designed for an indoor environment, the system was not exposed to any significant changes in light conditions and interference from rain.

For high accuracy results, a vast array of expensive cameras is required to collect a plethora of high resolution images, where each camera requires a specific setup to ensure the system is fully calibrated. This combination makes this solution unsuitable from a cost, infrastructure, and setup perspective, and therefore not achieving the project aims and objectives previously stated in Table 1.1. Since lacrosse is also typically an outdoor winter season sport, conditions vary significantly which can introduce challenges for this method where this system is sensitive to lighting conditions and motion blur.

### 1.6.2 Inertial Measurement Unit (IMU)

The method for position detection using IMU sensors falls under the dead reckoning process, outlined in 1.5.1. Using the orientation and velocity vectors recorded by the IMU sensor, the current position of the IMU in space can be deduced. IMUs are cheap and plentiful in supply, therefore being an

accessible solution for this positioning problem so a significant number of literature sources surround this specific method.

With the ambition to improve autonomous vehicle technology within the vehicle localisation system, research was conducted by the Konya Technical University on dead reckoning localisation using IMU sensors [14]. Findings from their practical vehicle testing demonstrated success of this system, with an average error in rotation and translation of 1.03 degrees and 1.04 meters respectively [14]. However, the IMU error values were obtained by comparing the positional data against ground truth values for the vehicle path. This ground truth was determined by the fusion of a Global Navigation Satellite System (GNSS) Real-Time Kinematic Positioning (RTK), IMU sensor and visual odometry (estimating position by using camera data) [14]. Since this ground truth path was defined by a combination of other sensors, should this method define the vehicle path inadequately and inaccurately, the calculated error of the IMU path could differ significantly from the true path suggesting limitations in results.

Studies and research into the motion analysis of football kicks using an IMU sensor have also been conducted [15]. Using a 6-Degree of Freedom (DoF) IMU, gyroscope and accelerometer data were fused to calculate the velocity of the foot during the kicking motion of a football. Results concluded that the approximate error in maximum foot velocity and height of the back swing was 4% and 2% respectively [15]. However, whilst these results are incredibly accurate, they were obtained through the comparison of the IMU data to data collected from two high-speed cameras, which were used to track the 'golden patterns' for the experiment. Since the reference foot velocity and back swing height was obtained from cameras, it is assumed that the method to determine this data is flawless and accurate, however, this is likely not the case.

The accessibility of this sensor, low cost, and relatively high accuracy makes this solution optimal for this proof-of-concept design. As outlined previously in 1.5.1, this system is inherent to drift errors in position results which is unfavourable.

### 1.6.3 GPS

As opposed to 1.6.2, this method of position detection is based on trilateration rather than dead reckoning. This method determines the position of an object on the Earth's surface by measuring the distance between the object, GPS receiver, and a minimum of four GPS satellites. This method relies on the Time of Flight (ToF) of the transmitted GPS signals to deduce distances between the receiver and satellite.

Using an iPhone 6, the University of Georgia investigated into the accuracy of horizontal positioning using GPS in an urban environment [16]. It was found that the horizontal position accuracy of the GPS system was 7-13m in an urban environment. Testing was also conducted on the accuracy of a Garmin GPS system where an average positional error of 1.724m was recorded [17]. Based on these results in literature this accuracy is not suitable for this project based on the project aims.

### 1.6.4 Ultra-Wide Band (UWB)

Similarly to trilateration using GPS, UWB object localisation uses short-duration pulses of radio waves over a wide frequency to determine the position of the radio wave receiver in space. Unlike GPS's limitations with indoor and noisy scenarios (urban environments and overhead cover), UWB does not suffer the same issues. In this localisation method, numerous anchors are placed within a given area and the position of a mobile tag is determined by ToF and trilateration.

Research into this area has shown a mean of 7cm error in localisation [18], presenting the UWB superiority with accuracy of position data. Research into this technology in a complex non-line-of-sight environment provided an accuracy of 0.32m displaying the sensors versatility and accuracy in different environments [19]. This method has many advantages over other localisation methods such as use in both indoor and outdoor environments with obstructions (non-line-of-sight), incredibly high accuracy and reliability, making it superior for this project.

### 1.6.5 Optimal Solution

Based on the brief review of current literature on methods used to solve similar localisation problems and the project aims (Table 1.1), a combination of an onboard IMU and UWB transmitters and receivers was selected as the optimum design solution for this proof-of-concept design.

The combination of sensors allows for the advantages of using an IMU, whilst removing drift error from the position data using UWB transmitters and receiver, (combination of dead reckoning and trilateration) which also provides superior positional data accuracy. The minimal infrastructure required to function and affordability also make this solution desirable for this proof-of-concept design. Following this decision in design direction, the following diagram, Figure 1.5, was produced to identify system areas to develop and integrate.

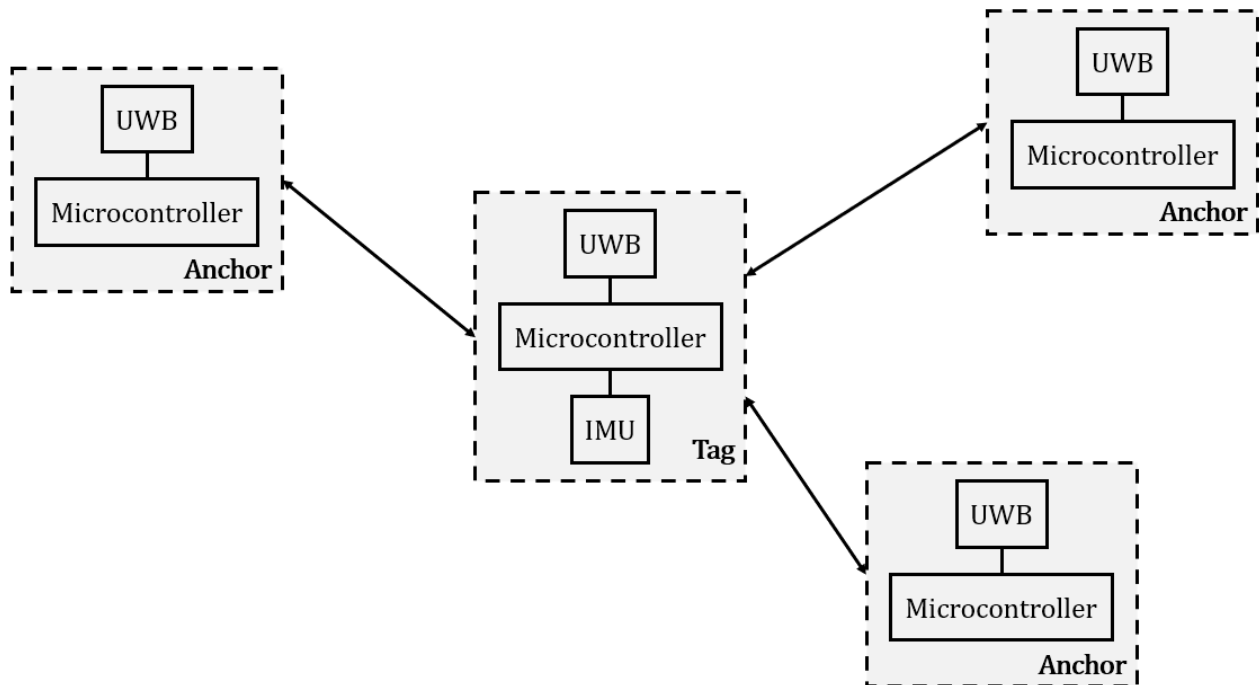


Figure 1.5: Initial proof-of-concept design showing the structure of the system with the UWB and IMU sensors

As presented, the system functions through the use of numerous Anchor Nodes (ANs) (at known positions on the lacrosse field) with identical system hardware structure, and one single tag (lacrosse ball) with an internal IMU to perform dead reckoning alongside the UWB trilateration.

Based on this design, the following sections of this report outlines the methods, design developments, and decisions associated with this proof-of-concept solution.

## Method: Microcontroller and Design Environment Selection

As indicated in Figure 1.5, both anchors and tag modules require a microcontroller to function. Therefore, the subsequent design decision was the selection of microcontroller to be used in the system. A microcontroller is typically used to control numerous elements of an electrical system.

Due to the nature of this proof-of-concept design, size and weight were not crucial aspects to consider within the microcontroller selection criteria, therefore, a microcontroller development board was an optimum solution. Microcontroller development boards are typically used within engineering proof-of-concept projects. This is due to its superiority with prototyping systems since no custom Printed Circuit Boards (PCBs) are required, whilst components and peripherals (motors, sensors, and displays) can be connected to the system with ease. These development boards are simple to operate and function 'out of the box' from the manufacturer, allowing for increased system development time compared to designing a bespoke Printed Circuit Board (PCB) for this system. However, criteria considered in this selection process included: processing power, memory size, number of General Purpose Input/Output (GPIO) ports, power consumption, cost, availability, and compatibility with development tools (design environments).

The microcontroller development boards considered for this system include the Arduino, ESP32, and STM32 products. They are all relatively accessible and in supply, each with a variety of advantages and drawbacks. The ESP32 family of microcontroller boards are the optimal solution for this project due to their wireless connectivity, low-power consumption, extensive number of GPIO pins, and dual-core processor making it superior for Internet of Things (IoT) applications. The ESP-NOW wireless communication protocol gives these boards another standout characteristic to the competition, which allows for quick, direct, and low-power control of smart devices, between the communication of numerous boards through a wireless network without the requirement of a router. The final microcontroller development board selected for this project was the ESP32-S3-DevKitC shown in Figure 2.1.

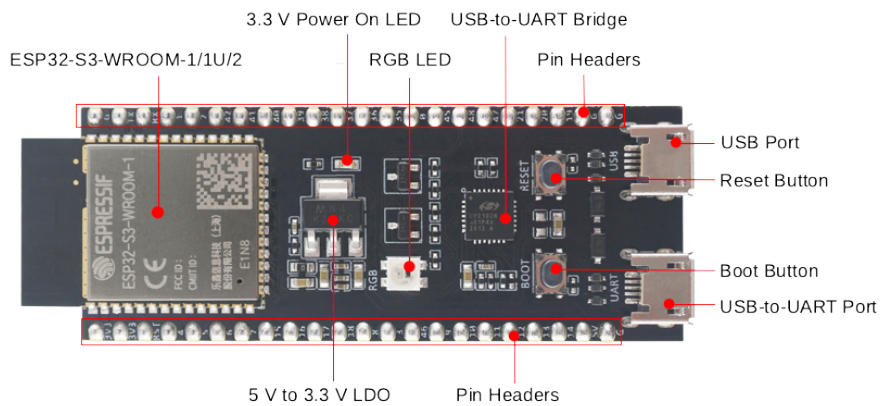


Figure 2.1: ESP32-S3-DevKitC board with annotations outlining components [20]

### 2.1 Design Environment Selection

The PlatformIO IDE (Integrated Design Environment) extension for Microsoft's Visual Studio Code was used to program the ESP32 board, this is due to the many powerful features and tools which make it suitable for more advanced projects, such as a debugger allowing the user to set breakpoints within the code to observe the state variables. Using Visual Studio Code also allows for a seamless transition from the microcontroller source code to other files used in this project since all files can be viewed within the same application. Alongside this the Arduino IDE was also used for its ease of use and simplicity.

## Method: Onboard IMU - Dead Reckoning Method

---

As shown in Figure 1.5, the lacrosse ball (tag) utilises an IMU to perform dead reckoning to localise the ball in space. In practice the IMU will be located within the lacrosse ball (onboard sensor), similarly to the IMU used for the KINEXON football 1.1.3, however, for the scope of this project the mechanical integration of the IMU within the lacrosse ball will not be explored in this report, and only the position and orientation detection is investigated.

### 3.1 IMU Functionality

IMUs typically contain up to three separate sensors, known as Micro-electromechanical Systems (MEMS), within the complete system (gyroscope, accelerometer, and magnetometer), where the complete system is presented in Figure 3.1. These three sensors all have individual functions and objectives explained below. Together, through sensor fusion, the IMU can provide information on object orientation and motion in space, with industrial navigation use cases within the aerospace, automotive, and naval industries.

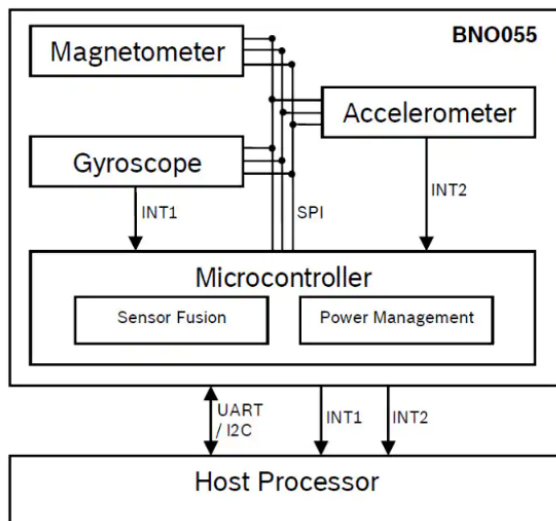


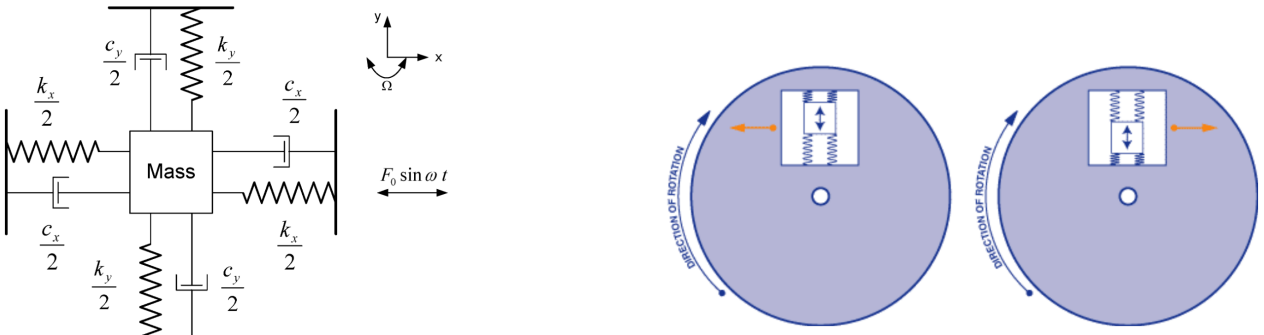
Figure 3.1: Bosch BNO055 Intelligent 9-Axis Absolute Sensor system architecture, outlining the communication and separation of each internal sensor [21]

#### 3.1.1 MEMS Gyroscope

The gyroscope (also known as angular rate sensor) is used to measure and detect angular rotation about the X, Y, and Z axes. The internals of a gyroscope contain a small inertial rotating mass which moves in relation to the gyroscope's angular velocity, Figure 3.2a, where the mass' displacement is converted to an electrical signal which corresponds to a precise angular rotation value, illustrated in Figure 3.2b.

#### 3.1.2 MEMS Accelerometer

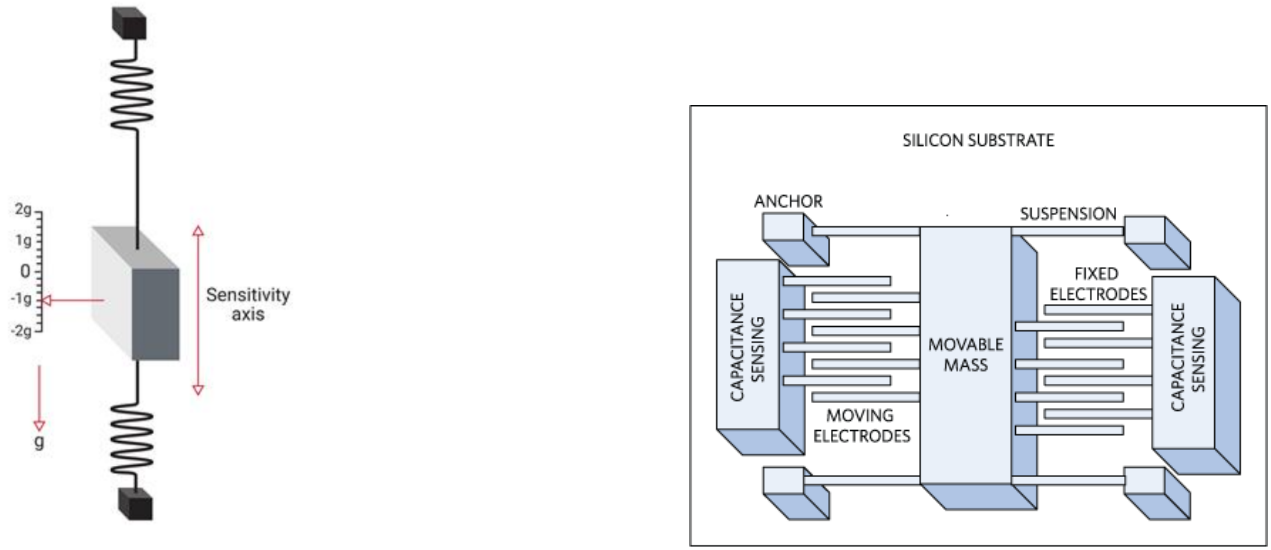
An accelerometer is responsible for measuring inertial acceleration in the X, Y, and Z axes. These sensors utilise a proof mass suspended by springs, which is only able to move along the sensitivity axis, so therefore, the linear acceleration is proportional to the total deflection of the proof mass (Figure 3.3a) which is determined by the capacitor sensing elements integrated within the sensor, shown in Figure 3.3b.



(a) Internal mechanical system of a gyroscope - single-axis mass-spring gyroscope [22]

(b) Internal operational view of a MEMS gyro sensor [23]

Figure 3.2: MEMS Gyroscope internals and functionality



(a) Simple MEMS accelerometer model: proof mass suspended by springs which can only move along the sensitivity axis [24]

(b) Mechanical model of an accelerometer [25]

Figure 3.3: MEMS Accelerometer internals and functionality

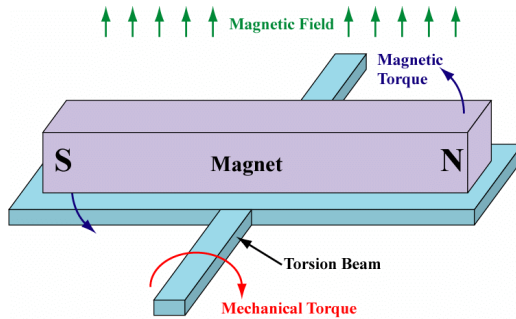


Figure 3.4: Illustration of a ferromagnetic MEMS magnetometer design [26]

### 3.1.3 MEMS Magnetometer

This sensor determines the strength and direction of a magnetic field to provide data on the intensity and heading of a magnetic field in the X, Y, and Z axes (Figure 3.4).

### 3.2 IMU Selection

When selecting the IMU for this project the following criteria were considered with each option: sensor versatility, performance, ease of use, and cost. The first IMU option explored was the MIKROE BMI270 IMU, shown in Figure 3.5. This is a 6-DoF IMU that contains a tri-axial gyroscope and accelerometer (therefore 6-Dof). This product is designed and optimised for wearables such as wrist-worn devices, so the system has a small form factor. Since this solution is a 6-DoF sensor, it was undesirable for this application regardless of the other selection criteria.

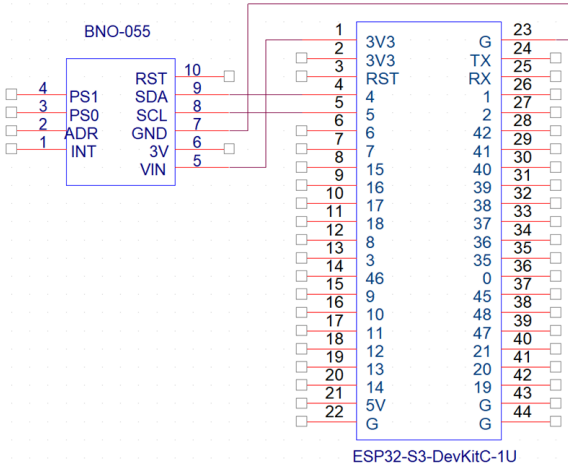


Figure 3.5: MIKROE BMI270 IMU [27]

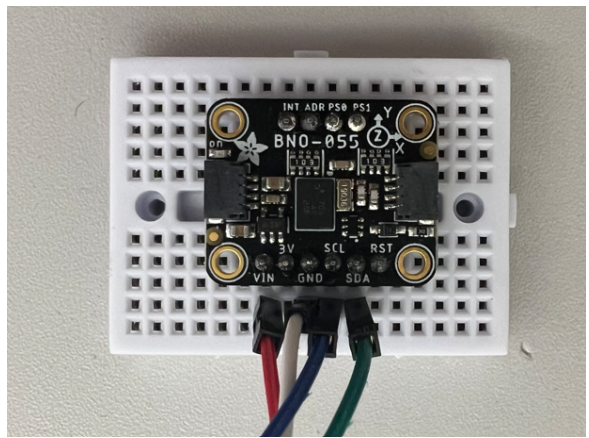
The other option explored was the Adafruit BNO055 IMU. This is a 9-DoF device that contains a tri-axial gyroscope, accelerometer, and magnetometer, making it an incredibly versatile solution for a cost of £24.77 [28]. It has several valuable features that can be used to extract data such as quaternions. It can record acceleration within the  $\pm 16\text{g}$  range, angular rotations in the  $\pm 2000^\circ/\text{s}$ , and magnetic field strength of  $\pm 1300\mu\text{T}$  in the X and Y axes and  $\pm 2500\mu\text{T}$  in the Z-axis. Additionally, the supplier, Adafruit, has published many supporting documents to help with setting up and using this sensor. Due to the ease of use, performance, and low cost, the Adafruit BNO055 IMU was selected for this design.

### 3.3 IMU Setup

When interfacing the Adafruit BNO055 9-DoF IMU with the ESP32-S3-DevKitC microcontroller, the I2C communication protocol was used using the VIN, SDA, SCL and GND IMU pins. Since the ESP32 board has no predefined I2C pins, the SDA and SCL pins were defined in the software as GPIO4 and GPIO5 respectively (project's GitHub repository: <https://github.bath.ac.uk/smads22/MEng-Final-Project>). Figure 3.6a below outlines the schematic diagram for the IMU hardware setup and integration with the microcontroller, with 3.6b displaying the corresponding physical setup used throughout the design development and testing of the IMU system. Alongside this the Adafruit BNO055 library package was installed and included within the IDE.



(a) Schematic diagram of the IMU setup and integration with the ESP32-S3-DevKitC



(b) Physical IMU setup showing the I2C pins used

Figure 3.6: IMU schematic and physical setup

### 3.3.1 IMU Calibration

When the BNO055 IMU is powered up it requires to undergo a full system calibration. This full device calibration is split into four separate calibration registers: gyroscope, accelerometer, magnetometer, and complete system. These individual calibration statuses return values in the range of 0 to 3 which correspond to uncalibrated and fully calibrated data respectively, influencing output data accuracy and reliability. The following sections outline the complete process to calibrate each individual sensor and therefore the complete IMU as stated by the manufacturer.

#### Gyroscope Calibration

1. Start with the IMU placed on a flat surface
2. Leave the device stationary
3. Observe the calibration value, stop this process once the gyroscope is calibrated fully (output value of 3)

#### Accelerometer Calibration

1. Start with the IMU placed on a flat surface
2. Pitch the device 45-degrees and hold at this angle for 3s
3. Increase the pitch to 90-degrees and hold at this angle for 3s
4. Continue this process in 45-degree intervals until the device has performed a full 360-degrees of pitch and returns to its original position in step 1
5. Complete steps 1 to 5 in roll
6. Observe the calibration value, if the accelerometer has not calibrated fully (output value of 3), repeat steps 1 to 5

#### Magnetometer Calibration

1. Perform a ‘figure of 8’ in space
2. Observe the calibration value, stop this process once the magnetometer is calibrated fully (output value of 3)

## Full System Calibration

1. Observe the full system calibration output
2. Repeat calibration if system is not calibrated
3. Stop calibration once all other registers and full system register is calibrated

### 3.4 IMU Position Detection Algorithm

The term coordinate system is typically used in a navigation application and use cases, where this system is used to represent numerous points in space. There are two different types of coordinate systems known as the local and global coordinate systems. The local coordinate system is associated with a given object, an IMU in this case, with axes aligned with the orientation of the object. The other is the global coordinate system which provides a fixed reference and axes for all objects placed within an environment. The relationship between the local and global coordinate systems is illustrated in Figure 3.7 where the object with the North-East-Up and X-Y-Z axes represent the local and global coordinate systems respectively.

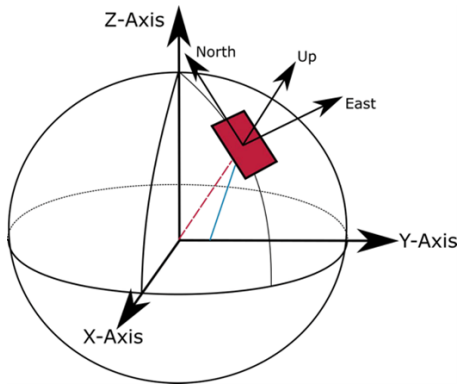


Figure 3.7: Illustration of the relationship between the local to the global coordinate system. In this case the object with the North-East-Up axes represents the IMU and the sphere is representing the global coordinate system [29]

Using the recorded acceleration data in the X, Y, and Z directions, a double integration can be used to derive IMU displacement and therefore, position, expressed in equations (3.1) to (3.3).

$$a(t) = \frac{dv}{dt} = \frac{d^2s}{dt^2} \quad (3.1)$$

$$v(t) = \frac{ds}{dt} = v_0 + \int a dt \quad (3.2)$$

$$s(t) = s_0 + \int v dt \quad (3.3)$$

IMUs record this 3-dimensional acceleration data relative to its varying orientation in its local frame. In order to accurately determine the IMU position and trajectory in space, a relationship needs to be established between the local frame and a fixed frame (global coordinate system). This conversion allows for consistency across numerous sensors with different local coordinate systems. As the overall positioning solution requires data from both the IMU and UWB sensors, Figure 1.5, if both are not referencing the same coordinate system, during sensor fusion significant error will be present resulting in inaccurate and unreliable position data, therefore, not meeting the project aims and objectives.

To convert acceleration data from the IMU's local to the global coordinate system, a 3x3 rotation matrix,  $T_{rot}$ , is required where Euler angles and quaternion data can both be used to determine this

matrix. These methods are further explained in 3.4.1 and 3.4.2 respectively. Overall, to summarise this position derivation algorithm, the following diagram, Figure 3.8, displays this process to calculate the position of the IMU in space using the recorded IMU acceleration data.

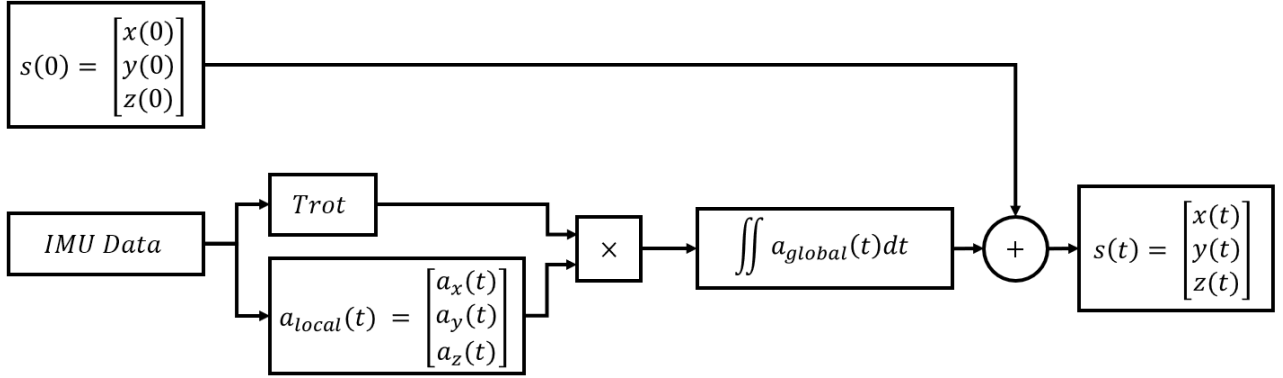


Figure 3.8: Illustration of the live position detection method used within the IMU section of the design

### 3.4.1 Euler Rotation Matrix Method

This method relies on the Euler angles for roll ( $\phi$ ), pitch ( $\theta$ ), and yaw ( $\psi$ ) (rotations about the X, Y, and Z axes respectively) which represents the IMU's orientation. The first step of this method is to compute the individual rotation matrices, these matrices are commonly found in robotic applications with trajectory planning, where the X, Y, and Z rotation matrices are represented in equations (3.4) to (3.6).

$$R(\hat{x}, \phi) = \begin{bmatrix} 1 & 0 & 0 \\ 0 & \cos(\phi) & -\sin(\phi) \\ 0 & \sin(\phi) & \cos(\phi) \end{bmatrix} \quad (3.4)$$

$$R(\hat{y}, \theta) = \begin{bmatrix} \cos(\theta) & 0 & \sin(\theta) \\ 0 & 1 & 0 \\ -\sin(\theta) & 0 & \cos(\theta) \end{bmatrix} \quad (3.5)$$

$$R(\hat{z}, \psi) = \begin{bmatrix} \cos(\psi) & -\sin(\psi) & 0 \\ \sin(\psi) & \cos(\psi) & 0 \\ 0 & 0 & 1 \end{bmatrix} \quad (3.6)$$

The combined rotation matrix,  $Trot$ , is obtained by multiplying the rotation matrices in the X, Y, and Z axes. For this specific use case, the ZYX convention is used, eq (3.7). The full combined rotation matrix is expressed in (3.8) where  $c$  represents  $\cos$  and  $s$  represents  $\sin$ .

$$Trot = R(\hat{z}, \psi) R(\hat{y}, \theta) R(\hat{x}, \phi) \quad (3.7)$$

$$Trot = \begin{bmatrix} c(\psi)c(\theta) & -s(\psi)c(\phi) + c(\psi)s(\theta)s(\phi) & s(\psi)s(\phi) + c(\psi)s(\theta)c(\phi) \\ s(\psi)c(\theta) & c(\psi)c(\phi) + s(\psi)s(\theta)s(\phi) & -c(\psi)s(\phi) + s(\psi)s(\theta)c(\phi) \\ -s(\theta) & c(\theta)s(\phi) & c(\theta)c(\phi) \end{bmatrix} \quad (3.8)$$

Using the combined rotation matrix, the local acceleration of the IMU can be converted to the global coordinate system by multiplying (3.8) by the local acceleration data. Once this global acceleration data is determined, a vector representing gravity (-9.81) can be subtracted to remove the effect of gravity on the position calculation.

$$\begin{bmatrix} a_{xglobal} \\ a_{yglobal} \\ a_{zglobal} \end{bmatrix} = Trot \begin{bmatrix} a_{xlocal} \\ a_{ylocal} \\ a_{zlocal} \end{bmatrix} \quad (3.9)$$

However, this method has one significant limitation that will affect the accuracy of results. Euler angles are victim to gimbal lock, this occurs when two of the three rotational axes become aligned, resulting in a loss of one DoF in the system. This loss in DoF results in the misrepresentation of certain rotational transformations since they can be represented through a singular rotation. The derivation of this gimbal lock is further presented by H. Parwana [30].

### 3.4.2 Quaternion Rotation Matrix Method

First introduced by Sir William Rowan Hamilton in 1843 [31] the quaternion method is a mathematical concept that applies complex numbers to represent rotations in 3-D space. The quaternion represents 4 components ( $w, x, y, z$ ) where,  $w$  is a scalar component that corresponds to the amount of rotation about an axis, and  $(x, y, z)$  is the vector component which corresponds to the axis of rotation and direction of the rotation in 3-D space. Unlike the Euler angle method, quaternions are not affected by gimbal lock since they are not reliant on a fixed sequence of rotations, like that in the Euler angle method shown in equation (3.7), as they are represented by both the scalar and vector components [30]. Additionally, quaternions are significantly more computationally efficient and more stable than the Euler method to represent rotation transformations (3.4.1), therefore, resulting in greater industrial adoption.

The first step of this method is to determine the combined rotation matrix is to obtain the normalised quaternion, which represents the IMU's local orientation relative to the global coordinate system. This normalised quaternion can be extracted directly from the BNO055 IMU through the `.getQuat(void)` function.

$$q = (w, x, y, z) \quad (3.10)$$

Using this normalised quaternion, the 3x3 rotation matrix used to convert local accelerations to the global coordinate system is displayed in equation (3.11), as derived by Jay A. Farrell [32].

$$Trot = \begin{bmatrix} w^2 + x^2 - y^2 - z^2 & 2(xy - wz) & 2(xz + wy) \\ 2(xy + wz) & w^2 - x^2 + y^2 - z^2 & 2(yz - wx) \\ 2(xz - wy) & 2(yz + wx) & w^2 - x^2 - y^2 + z^2 \end{bmatrix} \quad (3.11)$$

## 3.5 IMU Live Orientation

As presented in equation (3.8), values for IMU orientation are required (roll, pitch and yaw) to produce the rotation matrix which is used to convert local acceleration to the global coordinate system. These orientation values can be obtained through the use of the three onboard sensors and the quaternion `.getQuat(void)` function. Whilst orientation values are not required for the quaternion rotation matrix method, 3.4.2, the performance can be directly compared to the orientation values used within the Euler method, better informing on the most suitable solution for this localisation problem.

### 3.5.1 Accelerometer Data

Utilising the three sensors described in 3.1, values for pitch, roll and yaw can be determined. Accelerometer data can be used to calculate roll and pitch values through the following trigonometric equations [33]:

$$\phi_{accel} = \tan^{-1}\left(\frac{a_y}{a_z}\right) \quad (3.12)$$

$$\theta_{accel} = \tan^{-1}\left(\frac{-a_x}{\sqrt{a_y^2 + a_z^2}}\right) \quad (3.13)$$

As the accelerometer measures the acceleration due to gravity along the X, Y, and Z axes it is unable to measure yaw angles. This is because yaw is the rotation about the Z (vertical) axis, which is parallel to the direction of gravity. Accelerometers also have numerous limitations, whilst they are quick in response, they are extremely sensitive to vibrations and noise resulting in false output data.

### 3.5.2 Gyroscope Data

Since the gyroscope measures the rate of rotation about the three axes (angular velocity,  $\omega$ ), integrating these outputs will produce the total angular rotation about each axis (roll, pitch, and yaw values) in time. These expressions are shown below.

$$\phi_{gyro}(t) = \phi(0) + \int_0^t \omega_x(t) dt \quad (3.14)$$

$$\theta_{gyro}(t) = \theta(0) + \int_0^t \omega_y(t) dt \quad (3.15)$$

$$\psi_{gyro}(t) = \psi(0) + \int_0^t \omega_z(t) dt \quad (3.16)$$

Gyroscopes are insensitive to noise however drift over time so is unable to be a standalone solution for all orientation calculations.

### 3.5.3 Magnetometer Data

Using the magnetometer data recorded in the X, Y, and Z axes (denoted by  $m_x$ ,  $m_y$ , and  $m_z$  respectively), the horizontal X and Y components for the Earth's magnetic field can be calculated, equations (3.17) and (3.18). Using these values, the yaw angle can be derived in equation (3.19) [34].

$$x_h = m_x \cos(\theta) + m_y \sin(\theta) \sin(\phi) - m_z \sin(\theta) \cos(\phi) \quad (3.17)$$

$$y_h = m_y \cos(\phi) + m_z \sin(\phi) \quad (3.18)$$

$$\psi_{mag} = \tan^{-1} \left( \frac{y_h}{x_h} \right) \quad (3.19)$$

However, magnetometers have limitations, they are extremely sensitive to their environment which introduces errors into the output data, these errors are due to hard and soft iron bias. Hard iron bias is the offset in magnetometer readings due to the presence of a nearby permanent magnetic or ferromagnetic materials which interfere with sensor readings. Soft iron bias is the non-linear distortion in magnetometer readings due to temporarily magnetised materials in the sensor's proximity [34]. Alongside this equations (3.17) and (3.18) outline that the magnetometer yaw value is reliant on roll and pitch values, from another sensor, therefore introducing another possible cause of error within the output data.

### 3.5.4 Complementary Filters

As previously stated, each sensor has its own limitations and drawbacks. Whilst accelerometers are quick in response, they are highly sensitive to vibrations, gyroscopes are not influenced by noise however values drift over time, and the magnetometer can accurately measure yaw values however are subject to electromagnetic interference. Therefore, if all sensor outputs are combined to retain sensor advantages and remove limitations and inaccuracies, output orientation data will be superior.

To achieve this, a complementary filter is used. This filter is a computationally inexpensive sensor fusion technique that uses a High-Pass Filter (HPF) and Low-Pass Filter (LPF). These filters take two inputs and attenuates high and low-frequency noise from the input signals to produce a clean output shown in Figure 3.9.

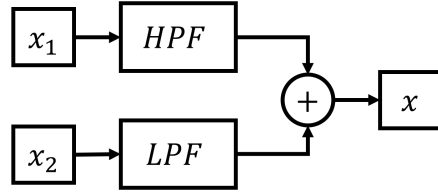


Figure 3.9: Basic example of a complementary filter that attenuates high and low-frequency noise from 2 inputs ( $x_1$  and  $x_2$ ) to produce a clean output signal ( $x$ )

As explained, accelerometer data is subject to high-frequency noise (vibrations), and the gyroscope is subject to low-frequency noise (drift). Passing accelerometer data through a HPF and gyroscope through a LPF will attenuate this noise providing accurate pitch and roll values, represented in equations (3.20) and (3.21), where  $\frac{1}{1+Ts}$  and  $\frac{Ts}{1+Ts}$  are a first-order low and high pass filter respectively [35].

$$\theta_{comp} = \frac{1}{1+Ts}\theta_{accel} + \frac{Ts}{1+Ts}\theta_{gyro} \quad (3.20)$$

$$\phi_{comp} = \frac{1}{1+Ts}\phi_{accel} + \frac{Ts}{1+Ts}\phi_{gyro} \quad (3.21)$$

Similarly, using a complementary filter on the yaw output from the gyroscope and magnetometer will allow for data that is less sensitive to iron bias and drift, therefore, providing a more accurate yaw output in various conditions. However, since the practical use case of the complete system will be on a lacrosse field, interaction with ferromagnetic materials or electromagnetic interference, external to the ball, will be extremely limited, reducing the likelihood of iron bias.

Through the implementation of these complementary filters, Figure 3.10 represents the complete method to determine orientation values from the raw IMU sensor data, where the orientation values will be used within the Euler rotation matrix method 3.4.1.

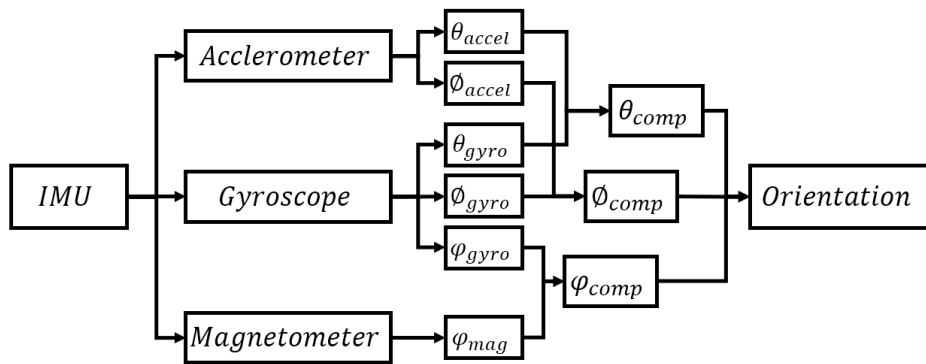


Figure 3.10: Live orientation calculation through complementary filter implementation

### 3.5.5 Quaternion Data

As previously stated, it is not essential to calculate orientation values directly for the quaternion rotation matrix method 3.4.2, however, obtaining these values allows for a tangible comparison to be made between this method and its Euler method counterpart. As derived in 'Universal approach to derivation of quaternion rotation formulas' [36], quaternion data can be converted to Euler angles to directly compare against orientation data obtained from the raw IMU data. These conversions are shown below in equations (3.22), (3.23), and (3.24).

$$\phi = \tan^{-1}\left(\frac{2(wx + yz)}{1 - 2(x^2 + y^2)}\right) \quad (3.22)$$

$$\theta = \sin^{-1}(2(wy - xz)) \quad (3.23)$$

$$\psi = \tan^{-1}\left(\frac{2(wz + xy)}{1 - 2(y^2 + z^2)}\right) \quad (3.24)$$

## 3.6 Onboard IMU Testing Plan

This section outlines all testing planned to validate each element of the onboard IMU design and methodology. Due to the simplicity and ease of use, the Python programming language was used to implement these designs alongside the design environment selected in 2.1. Detailed testing plans are shown in Appendix A, outlining the test name, test description and instructions, and aims of each test.

### 3.6.1 Calibration Testing Plan

Calibration testing is used to ensure the IMU can be calibrated easily to provide accurate and reliable data. Since this is also a key element within the project aims, the validation of the calibration method is crucial.

### 3.6.2 Orientation Testing Plans

Following the structure of the IMU Live Orientation design (3.5), each element explored in the methodology was tested to ensure the system performs as expected and justifies the design decisions made for determining the IMU's orientation. For all testing that requires the measurement of angles, a simple protractor method was used to determine actual IMU angles about each axis, shown in Figure 3.11. Testing plans and aims associated with the accelerometer, gyroscope, magnetometer, complementary filter, and quaternion orientation methods are outlined in Tables 8.2, 8.3, 8.4, 8.5, and 8.6 respectively within Appendix A. Below are the summarised testing plans, outlining the aims for each element of the design. These tests were conducted to determine the optimal solution for deriving the IMU's orientation.

#### Accelerometer Testing Plan

The tests completed on this element of the design was to evaluate the effectiveness of determining IMU pitch and roll using the accelerometer values from the IMU. Other factors such as orientation response and error due to mechanical noise were also explored, comparing the same data against filtered results. Testing was concluded with investigation into the accuracy of orientation values to compare the method to other proposed designs.

#### Gyroscope Testing Plan

Similarly to testing conducted on the accelerometer design, the gyroscope was tested to validate the method to determine the IMU's roll, pitch, and yaw and the response of this system. Due to the limitations with the gyroscope, the effect of drift was also investigated, and the accuracy of the orientation outputs were evaluated.

#### Magnetometer Testing Plan

Testing for this element of the design utilised the gyroscope roll and pitch values to obtain the IMU yaw (due to equations (3.17) and (3.18) requiring roll and pitch to obtain yaw). Results were collected for this method to evaluate the success with detecting changes in IMU yaw, effect of roll and pitch on yaw, and accuracy of output data. Due to the limitations in the magnetometer due to electromagnetic noise, the design was also tested to determine the robustness against iron bias.

### **Complementary Filter Testing Plan**

Combining the outputs from different methods to obtain the roll, pitch, and yaw values for the IMU, testing was conducted to determine the success of this design against different orientation values. The response of the design was also evaluated and tested against sources of errors and shortcomings present in the other methods to determine the success of the design. Finally, the accuracy of the design was tested, and orientation visualised in a 3-D animation.

### **Quaternion Testing Plan**

The final set of tests were conducted on the quaternion orientation design. Similarly to all previous testing plans, the output roll, pitch, and yaw values were reviewed against the systems performance, response, and accuracy to allow for comparisons against the other methods. Similarly to the complementary filter testing plan, the testing was concluded with the 3-D animations to visualise the real-time orientation of the IMU.

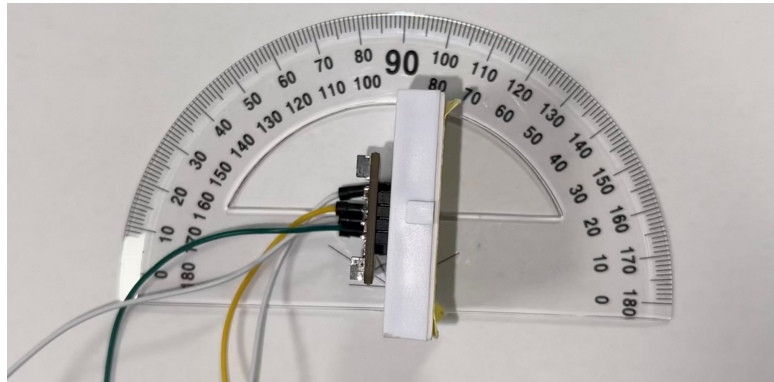


Figure 3.11: Orientation testing setup example where the IMU is pitched at  $90^\circ$

#### **3.6.3 Position Testing Plans**

To validate the methodology and design explored for the IMU position detection algorithm using the onboard IMU (3.4), a proposed testing plan and testing setup (Figure 3.12) were produced to support with the verification of the design. The testing plan was implemented for both Euler and quaternion positioning methods to compare the effectiveness of each design when localising the IMU in 3-D space using the same raw IMU data in the form of a .csv file. The IMU was translated from each corner of a 30x30x30cm cube to record raw IMU data, which was further processed to plot positional results and compared to the actual IMU trajectory.

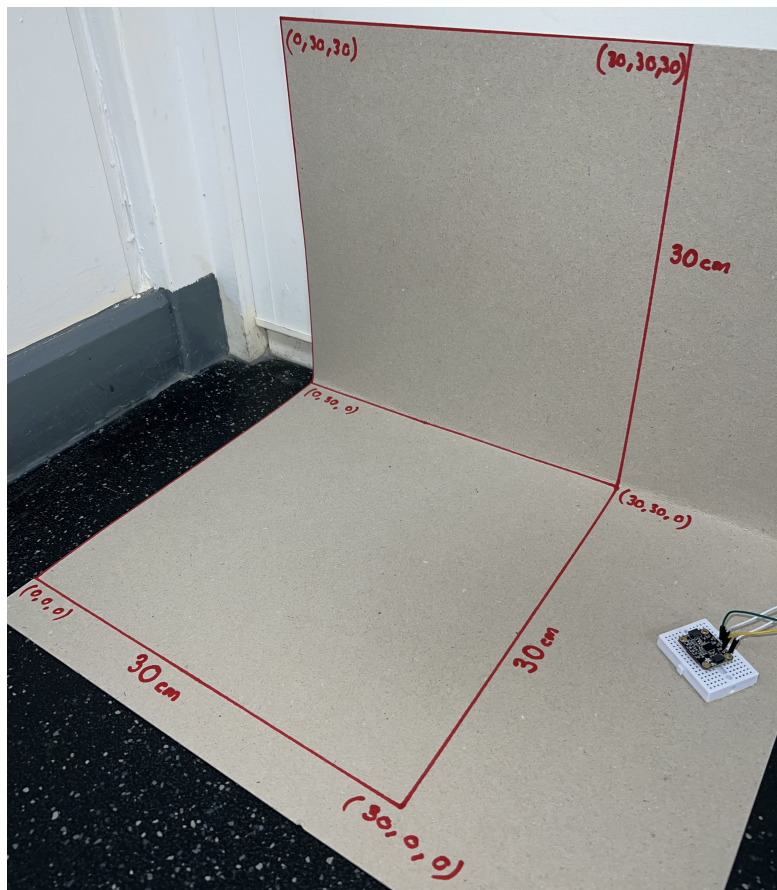


Figure 3.12: Position testing setup to measure the IMU's position in 3-D space (30cmx30cmx30cm area)

## Method: UWB Module - Trilateration Method

---

As shown in Figure 1.5, the other element of this complete system is the UWB sensors. This section of the report outlines the UWB functionality, operation, sensor selection, and method to determine the ball's location in three-dimensional space using the trilateration method previously outlined in 1.5.2.

### 4.1 ToF Methods

In UWB localisation, multiple Anchor Node (AN) devices are placed in the experiment area where a tag is used to communicate with the anchors. This communication allows for the tag to be localised and position determined. The anchors communicate with the tag through UWB radio wave signals and the ToF of this signal is used to determine the distance from each individual AN to the tag [37].

Since radio signals travel at the speed of light ( $c = 2.99 \times 10^8 m/s$  [38]), using the ToF of the signal, the following equation can be used to relate the distance ( $D$ ) travelled by the signal from the anchor to the tag.

$$D = c(ToF) \quad (4.1)$$

#### 4.1.1 One-Way Ranging

As shown in equation (4.1), the ToF of the signal is crucial with determining the distance of the tag from the AN. This method of calculating the ToF is the simplest, which uses the time at which the signal was sent from the AN ( $T_s$ ) and the time at which the tag receives the signal ( $T_r$ ). This method is summarised in equation (4.2).

$$ToF = T_r - T_s \quad (4.2)$$

Whilst this method is computationally efficient, it requires for both tag and AN to have synchronised clocks to minimise error in ToF results. Should the ToF be incorrect by 0.001s, this equates to an approximate distance error of 299km (equation (4.1)) showing the significance of accurate time measurements.

#### 4.1.2 TWR

The Two-Way Ranging (TWR) system is a method of ranging using two transceivers, devices that can act as both transmitters and receivers. TWR calculates the ToF through the use of the reply time of a device (time elapsed from receiving a signal to replying) and the round-trip time (time elapsed from sending a signal and receiving the signal from the other transceiver), which negates the effect of unsynchronised clocks that is present in the One-Way Ranging method in 4.1.1. There are further adaptations of this method that can be used which are explained further.

#### Single-Sided TWR

This method is the simplest of the three TWR methods explored, where the AN sends a signal to the tag which replies with a corresponding signal. The ToF is then calculated using the difference between the total time from the first signal and the reply time from the tag. The equation and illustration of this method are shown below in equation (4.3) and Figure 4.1a [39].

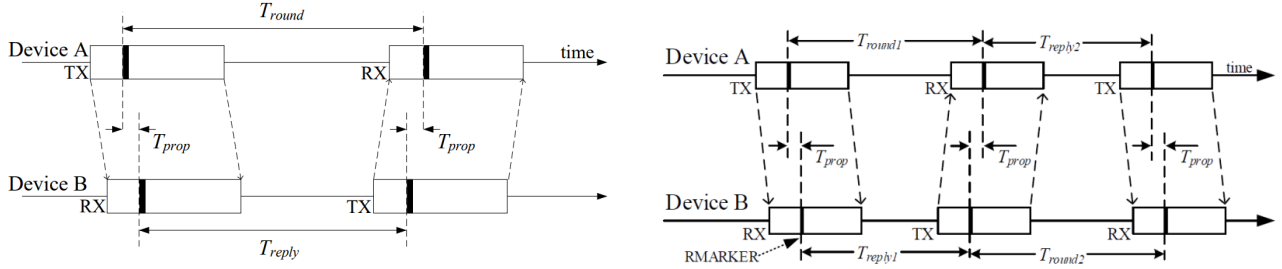
$$ToF = \frac{T_{total} - T_{reply}}{2} \quad (4.3)$$

## Symmetrical Double-Sided TWR

Unlike to single-sided TWR, this system sends another signal back to the original transceiver to record the ToF. The first transceiver transmits a signal to another transceiver, which receives the first signal and immediately responds with another transmitted signal to the original transceiver recording the round trip time, shown in Figure 4.1b.

$$ToF = \frac{T_{total1} - T_{reply1} + T_{total2} - T_{reply2}}{4} \quad (4.4)$$

This method is more stable than the single-sided TWR method. This is due to the greater number of measurements taken and deriving ToF as the average of the three transmissions, compared to the two transmissions that occur in single-sided TWR [40]. However, symmetrical double-sided TWR has the restriction that  $T_{reply1}$  and  $T_{reply2}$  has to be equal which adds a constraint to the system.



(a) Illustration of a Single-Sided TWR system, where  $T_{round}$  and  $T_{prop}$  are  $T_{total}$  and  $2(ToF)$  respectively from equation (4.3) [39]

(b) Illustration of a symmetrical double-sided TWR, where  $T_{round}$ ,  $T_{prop}$ , and  $T_{reply}$  denote  $T_{total}$ ,  $4(ToF)$  and the reply times [40]

Figure 4.1: Single and Double-Sided TWR Systems

## Asymmetrical Double-Sided TWR

The asymmetrical double-sided is the final TWR method explored. This is similar to the symmetrical double-sided TWR method, however, the asymmetry of the system allows for the removal of the constraint  $T_{reply1}$  and  $T_{reply2}$  being equal, which allows for reduced errors and optimal results in situations where the reply times are unequal [40]. The formula for ToF is shown in equation (4.5)

$$ToF = \frac{T_{total1} \times T_{total2} - T_{reply1} \times T_{reply2}}{T_{total1} + T_{total2} + T_{reply1} + T_{reply2}} \quad (4.5)$$

## 4.2 Trilateration

As shown in equation (4.1), once distance,  $D$ , is calculated through ToF calculations, trilateration can be used to determine the location of the tag in space with relation to the other anchors.

### 4.2.1 Localisation in 2-D

When localising an object in 2-D, if the distance between the anchor and tag is known through equation (4.1), the position of the tag must be situated at a point along the circular perimeter  $D$  from the anchor, shown in Figure 4.2a. Implementing another AN to the system produces the output shown in 4.2b, illustrating that the tag must be located at either point  $T1$  or  $T2$ . Repeating this process with the addition of another AN in the complete system allows for the tag to be localised in 2-D space, where the intersection of all circles is the precise location of the tag ( $T$ ), shown in Figure 4.2c. This figure shows that in order to localise the tag in 2-D space, at least three ANs are required.

Using these three distances ( $D1$ ,  $D2$ , and  $D3$ ) and known 2-D position of each AN ( $x_1$ ,  $x_2$ ,  $x_3$ ,  $y_1$ ,  $y_2$ ,  $y_3$ ), the following equations can be solved to determine the precise location of the tag in 2-D space:

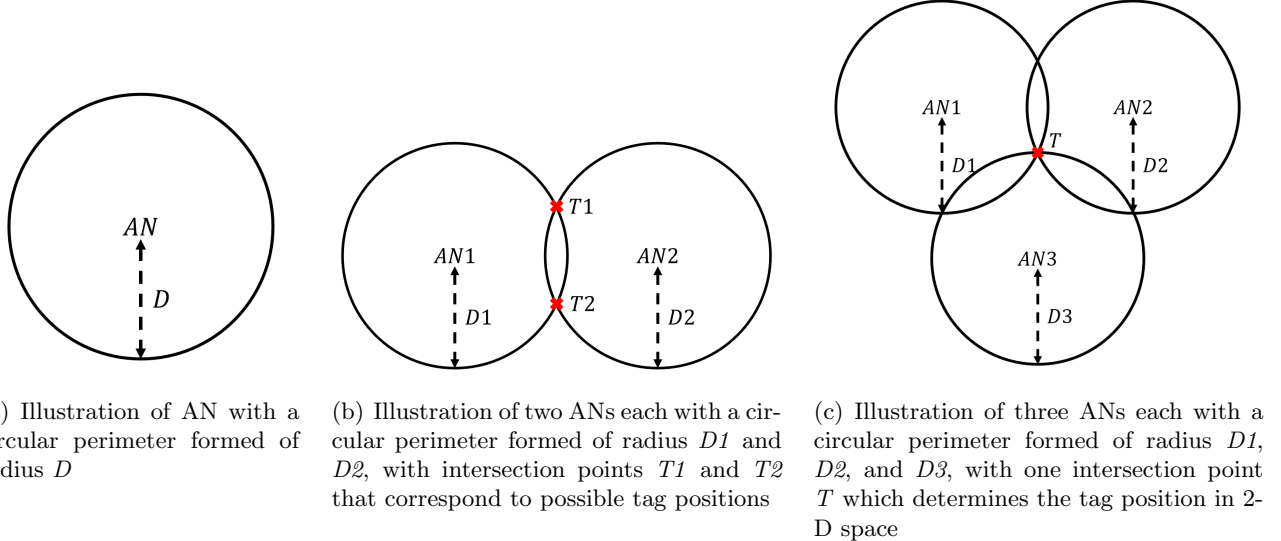


Figure 4.2: 2-D localisation with numerous ANs

$$(x - x_1)^2 + (y - y_1)^2 = D_1^2 \quad (4.6)$$

$$(x - x_2)^2 + (y - y_2)^2 = D_2^2 \quad (4.7)$$

$$(x - x_3)^2 + (y - y_3)^2 = D_3^2 \quad (4.8)$$

These equations are converted to linear equations by subtraction and substitution [41].

$$2x(x_2 - x_1) + 2y(y_2 - y_1) = \alpha \quad (4.9)$$

$$2x(x_3 - x_1) + 2y(y_3 - y_1) = \beta \quad (4.10)$$

where

$$\alpha = (D_1^2 - D_2^2) - (x_1^2 - x_2^2) - (y_1^2 - y_2^2) \quad (4.11)$$

$$\beta = (D_1^2 - D_3^2) - (x_1^2 - x_3^2) - (y_1^2 - y_3^2) \quad (4.12)$$

The following are the solved equations for the X and Y position of the tag [41].

$$x = f(D_1, D_2, D_3) = \frac{\begin{bmatrix} \alpha & 2(y_2 - y_1) \\ \beta & 2(y_3 - y_1) \end{bmatrix}}{\begin{bmatrix} 2(x_2 - x_1) & 2(y_2 - y_1) \\ 2(x_3 - x_1) & 2(y_3 - y_1) \end{bmatrix}} \quad (4.13)$$

$$y = g(D_1, D_2, D_3) = \frac{\begin{bmatrix} 2(x_2 - x_1) & \alpha \\ 2(x_3 - x_1) & \beta \end{bmatrix}}{\begin{bmatrix} 2(x_2 - x_1) & 2(y_2 - y_1) \\ 2(x_3 - x_1) & 2(y_3 - y_1) \end{bmatrix}} \quad (4.14)$$

#### 4.2.2 Localisation in 3-D

In addition to the localisation in 2-D space, 4.2.1, the altitude/height of the tag (lacrosse ball) also needs to be determined. This is completed in a similar process as to the 2-D localisation, however, a fourth AN is added to the system to produce another linear equation to solve for the tag's Z position. The full derivation of this method is outlined by H.Kim [41]. Below are the final equations relating to the X, Y, and Z position of the tag using trilateration.

$$\hat{x} = \hat{f}(D1, D2, D3, D4) = \frac{\begin{bmatrix} \alpha & 2(y_2 - y_1) & 2(z_2 - z_1) \\ \beta & 2(y_3 - y_1) & 2(z_3 - z_1) \\ \gamma & 2(y_4 - y_1) & 2(z_4 - z_1) \end{bmatrix}}{\begin{bmatrix} 2(x_2 - x_1) & 2(y_2 - y_1) & 2(z_2 - z_1) \\ 2(x_3 - x_1) & 2(y_3 - y_1) & 2(z_3 - z_1) \\ 2(x_4 - x_1) & 2(y_4 - y_1) & 2(z_4 - z_1) \end{bmatrix}} \quad (4.15)$$

$$\hat{y} = \hat{g}(D1, D2, D3, D4) = \frac{\begin{bmatrix} 2(x_2 - x_1) & \alpha & 2(z_2 - z_1) \\ 2(x_3 - x_1) & \beta & 2(z_3 - z_1) \\ 2(x_4 - x_1) & \gamma & 2(z_4 - z_1) \end{bmatrix}}{\begin{bmatrix} 2(x_2 - x_1) & 2(y_2 - y_1) & 2(z_2 - z_1) \\ 2(x_3 - x_1) & 2(y_3 - y_1) & 2(z_3 - z_1) \\ 2(x_4 - x_1) & 2(y_4 - y_1) & 2(z_4 - z_1) \end{bmatrix}} \quad (4.16)$$

$$\hat{z} = \hat{h}(D1, D2, D3, D4) = \frac{\begin{bmatrix} 2(x_2 - x_1) & 2(y_2 - y_1) & \alpha \\ 2(x_3 - x_1) & 2(y_3 - y_1) & \beta \\ 2(x_4 - x_1) & 2(y_4 - y_1) & \gamma \end{bmatrix}}{\begin{bmatrix} 2(x_2 - x_1) & 2(y_2 - y_1) & 2(z_2 - z_1) \\ 2(x_3 - x_1) & 2(y_3 - y_1) & 2(z_3 - z_1) \\ 2(x_4 - x_1) & 2(y_4 - y_1) & 2(z_4 - z_1) \end{bmatrix}} \quad (4.17)$$

where

$$\alpha = (D1^2 - D2^2) - (x_1^2 - x_2^2) - (y_1^2 - y_2^2) - (z_1^2 - z_2^2) \quad (4.18)$$

$$\beta = (D1^2 - D3^2) - (x_1^2 - x_3^2) - (y_1^2 - y_3^2) - (z_1^2 - z_3^2) \quad (4.19)$$

$$\gamma = (D1^2 - D4^2) - (x_1^2 - x_4^2) - (y_1^2 - y_4^2) - (z_1^2 - z_4^2) \quad (4.20)$$

### 4.3 UWB System Design

As shown in Figure 4.3, four ANs will be placed around the pitch on each corner of the field, to record 3-D tag (ball) position and efficiently cover the whole area. Lacrosse fields do not have exact dimensions, however, are maintained within a certain range for each venue so the system must be setup with the correct parameters prior to collecting data. The asymmetrical double-sided TWR is proposed for this design due to its low error and high accuracy compared to the other methods explored in 4.1. Whilst this method is more computationally demanding, use alongside the IMU system will allow for extremely accurate and fast results.

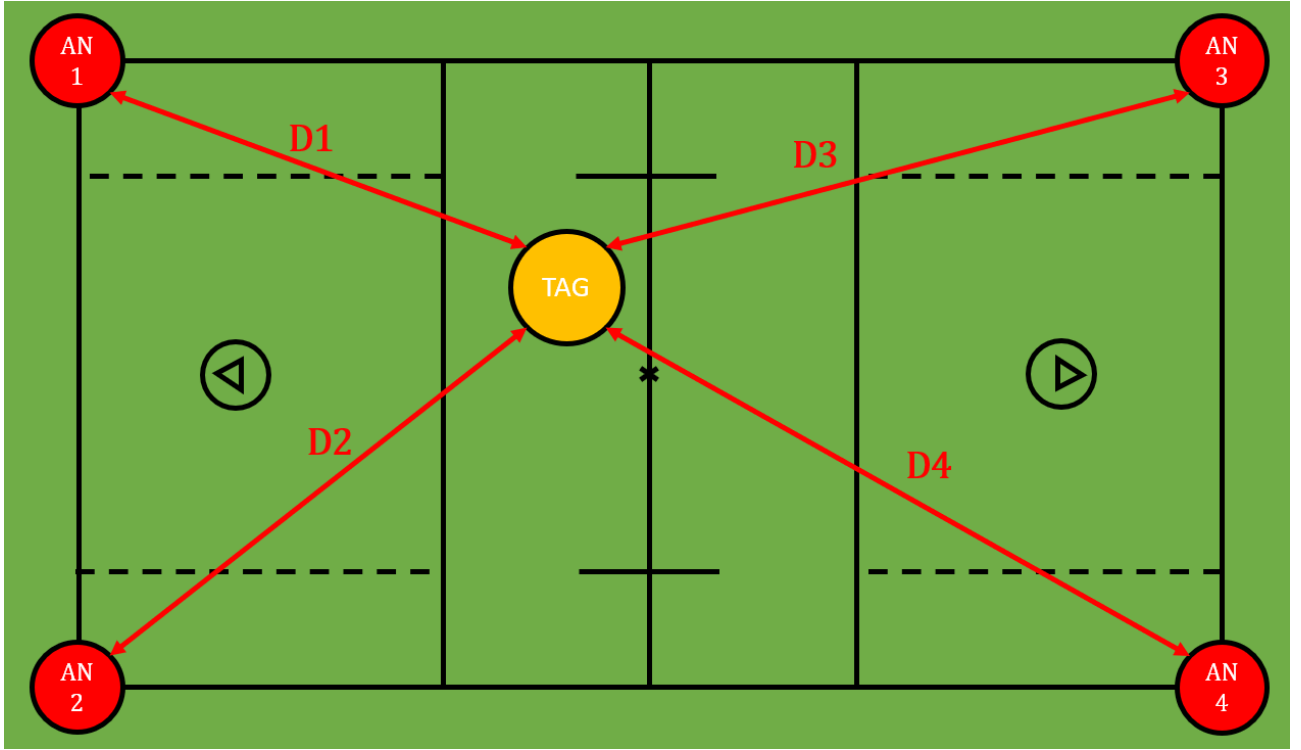


Figure 4.3: Proof-of-concept design for the UWB subsystem outlining locations of the ANs around the lacrosse field to localise the lacrosse ball (tag) in 3-D space, illustrating the setup in practice

#### 4.3.1 UWB Selection

Numerous options for UWB solutions are on the market, as shown in Table 4.1. Based on this information the Decawave manufacturer (acquired by Qorvo) was selected as the optimal solution for this design. This is due to the accuracy and significant range of the device whilst also being readily available from local suppliers. The typical lacrosse field is 110m long and 60m wide [42], making the 290m range of the Decawave system suitable for this application. A.Jiménez's [43] research into these manufacturers' technologies displayed the superiority of the Decawave UWB system in accuracy and reliability, therefore, further justifying selection for this design.

Table 4.1: Comparison of main UWB system manufacturers to support with UWB selection [44]

Specifications	Manufacturers		
	Decawave	BlinkSight	BeSpoon
Accuracy	10cm	10cm	10cm
Range	290m	200m	600m
Current Consumption	30mA	30mA	30mA
Availability	High	Low	Low

Decawave manufacture multiple solutions for UWB technology, DWM1000 and the most recent DWM3000 UWB chip, released in 2020 [45]. Decawave have stated that the DWM3000 has higher accuracy with results and faster Serial Peripheral Interface (SPI) speeds whilst consuming less power during operation [45]. T. Polonelli's accuracy and power consumption testing concluded the same results with found that both devices had similar precision in measurement ranges above one meter, whilst the DWM3000 performs 33.2% better over short distances, whilst consuming 50% less power than the DWM1000 [46]. Based on these factors the DWM3000 UWB chip was selected for this project due to its superior power efficiency, helping to ensure the device will last the duration of a full lacrosse game.

#### 4.3.2 DWM3000 Selection

The DWM3000 is available as a standalone chip from numerous suppliers, however, requires for a custom PCB to be designed and manufactured to allow for testing and integration with a microcontroller. Therefore, for the scope of this project, pre-made module options were explored to allow for increased design time for this method. Since size and weight were not significant factors for this proof-of-concept design, this further justifies the selection for a pre-made module over the design of a custom project specific PCB.

The first option explored was the ESP32 UWB DW3000 (Ultra Wideband) microcontroller, shown in Figure 4.4. This product incorporates the DWM3000 UWB chip with the ESP32 microcontroller, with supporting libraries provided by the supplier, Makerfabs). This product is shipped from the United States with a product cost of \$45.80 [47]. Due to the possible extended lead time from the supplier in the United States, this option was not preferable. Alongside this, the cost to purchase enough modules for the complete system equated to approximately 70% of the project budget, therefore, not allowing for contingency within the project. Lastly, since the microcontroller was previously selected and purchased during the early stages of the project, resorting to this product was not a financially viable option.

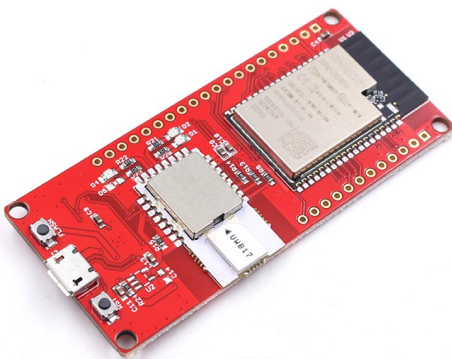


Figure 4.4: Makerfabs' ESP32 UWB DW3000(Ultra Wideband) device [47]

The follow option explored was the MikroElektronika UWB Click which is a small and lightweight package using Decawave's UWB chip shown in Figure 4.5. This product is designed for use with the supplier's 'mikroBUS' system for their microcontroller products, however, the SPI interface is used so is compatible with the ESP32-S3-DevKit microcontroller selected for this project. However, this product retails for £76.51 [48] which is 20% greater than the total allocated project budget making this solution undesirable. Therefore, this product was not selected, and cheaper alternatives were explored.

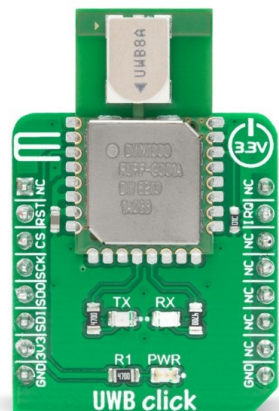
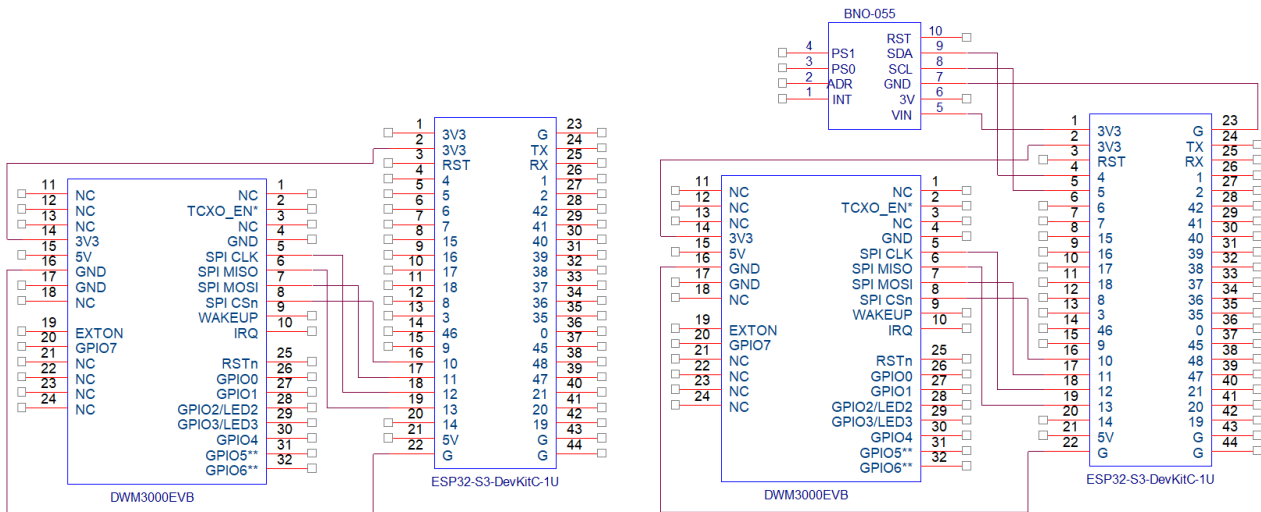


Figure 4.5: Mikroelektronika's UWB Click [49]

The final option explored for the DWM3000 selection was the Qorvo DWM3000EVB. This product is an evaluation board that utilises the SPI protocol making it ideal for this proof-of-concept design, since size and weight are not crucial. The cost of this product is £28.04 which is significantly cheaper than the other product options explored whilst retaining the same functionality. This product was the most financially viable solution, so was selected for this design.

#### 4.3.3 UWB Setup

When integrating the DWM3000EVB to the ESP32-S3-DevKitC the SPI protocol is used. Pins 10, 11, 12 and 13 are used on the microcontroller for both tag and AN. The tag system also incorporates the IMU connected to the microcontroller as previously stated in 3.3. The corresponding schematic diagram for the AN and tag designs are shown in Figures 4.6a and 4.6b respectively, with the physical setup of the DWM3000EVB shown in Figure 4.7



#### **4.3.4 UWB Testing**

Ultimately, no testing was conducted using the UWB sensors due to the lack of firmware support from the DWM3000EVB manufacturer. The microcontroller selected for this project, ESP32-S3-DevKitC, is not supported for this product so relevant libraries to integrate the microcontroller and UWB sensor were not available. Alongside this, developing the libraries for this sensor was not in the original project scope, resulting in limited resource to develop supporting libraries. Since this product was released relatively recently, a lack of open-source support was available. All factors resulted in no testing and validation of this design.

## Results

---

Based on the design and method outlined in 3, the following results were collected to review all aspects within the initial design to obtain the lacrosse ball's position in 3-D space. This results section is split into the IMU calibration, IMU orientation, and IMU position results. As previously stated, due to lack of supporting firmware published from the DWM3000EVB manufacturer, Quovo, no results were obtained for the trilateration method for localisation in 3-D space.

### 5.1 Onboard IMU Calibration Results

Figure 5.1 below displays the four IMU calibration registers reaching a value of 3 when the corresponding register is fully calibrated, where 'Acc Cal', 'Gyro Cal', 'Mag Cal', and 'System Cal' correspond to the accelerometer, gyroscope, magnetometer and IMU system calibration values respectively.

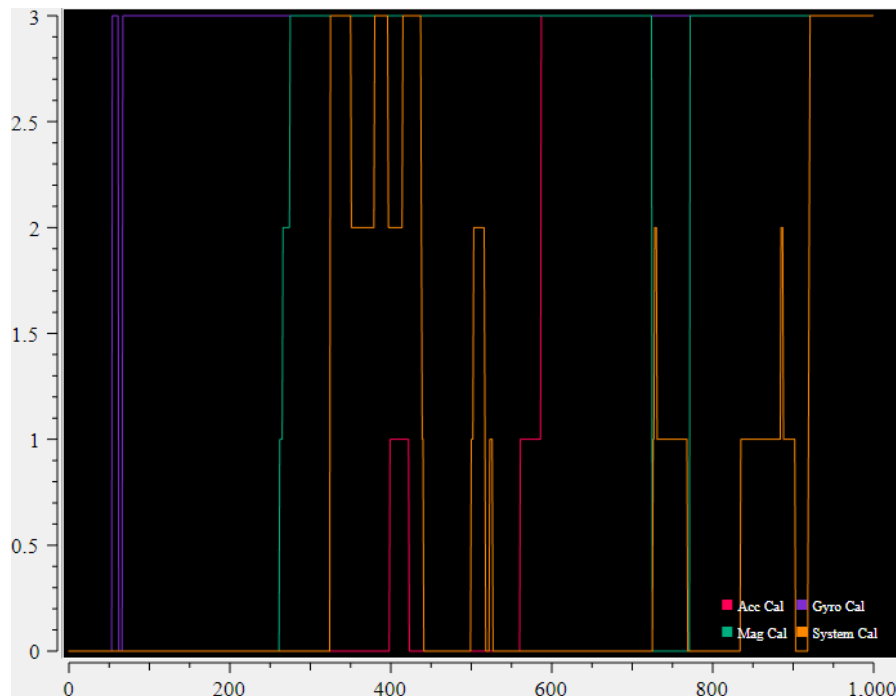


Figure 5.1: IMU calibration values when following the calibration testing plan outlined in table 7.2

### 5.2 Onboard IMU Orientation Results

Based on the testing plans described in 3.6, the following results were collected to validate and review the IMU orientation methodology and design.

#### 5.2.1 Accelerometer Orientation Results

When collecting the results for the accelerometer orientation values (method described in section 3.5.1), the first results collected were the raw roll and pitch outputs, displayed in Figure 5.2 and 5.3, which correspond to the 'Raw Pitch and Roll (-90° to 90°)' and 'Raw Pitch and Roll Response' tests from the IMU Accelerometer Testing Plan, Table 8.2.

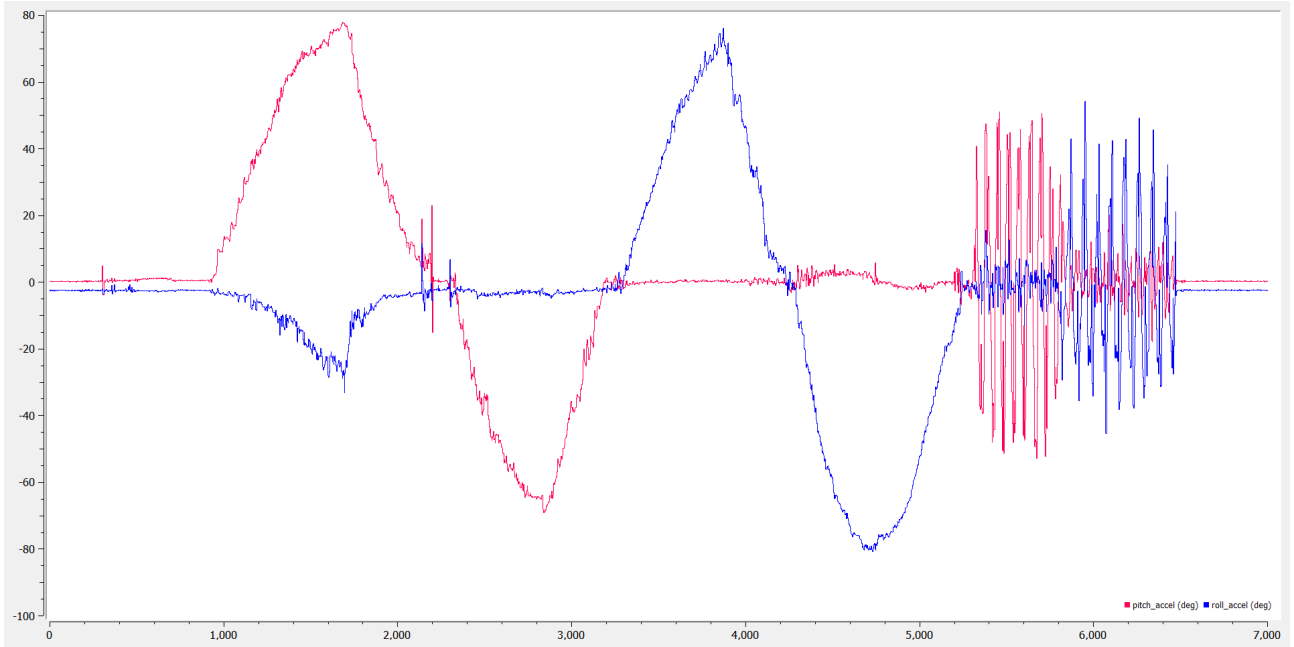


Figure 5.2: Roll (red) and pitch (blue) outputs from accelerometer data. IMU was rolled and pitched to 90° and -90° and vibrated to show the effects of noise with the results

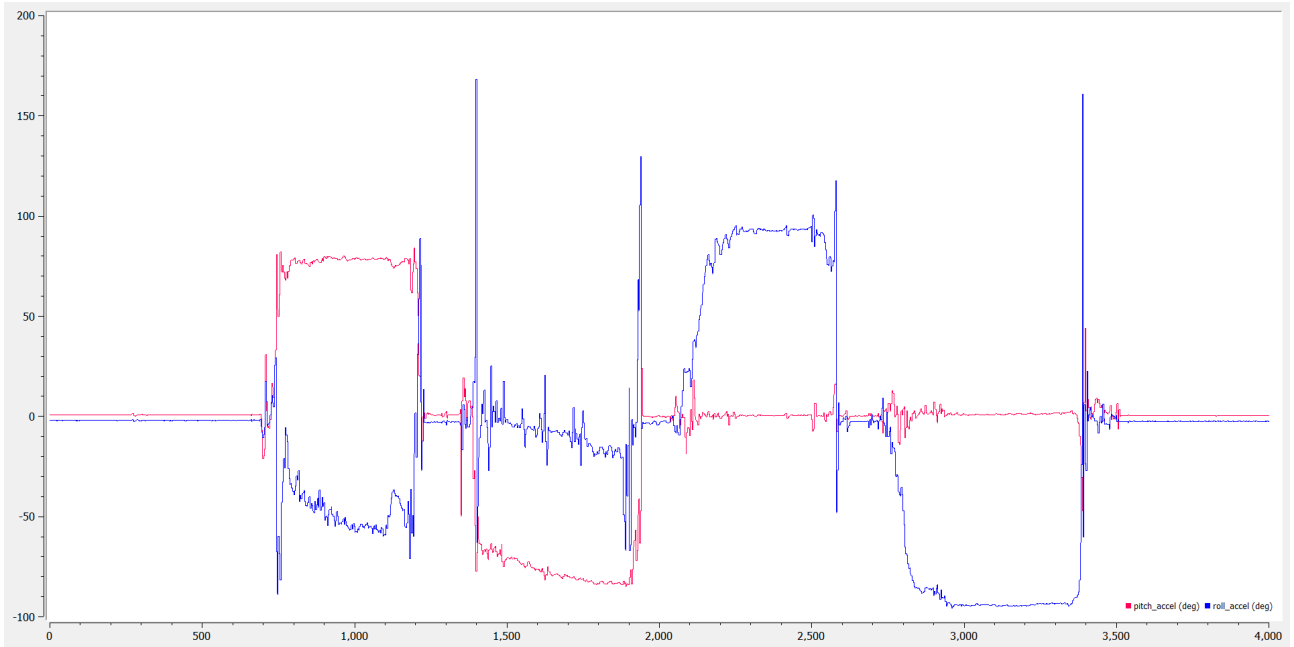


Figure 5.3: IMU rolled (red) and pitched (blue) to 90° and -90° rapidly to test the response of the accelerometer

Figure 5.2 and 5.3 show that the accelerometer pitch and roll can represent the orientation changes that the IMU is subject to. However, the effect of vibrations is highly influential in both sets of results. In Figure 5.2, the plots for roll and pitch are not smooth with small fluctuations from the actual orientation value. Alongside this, when the IMU experiences minor vibrations both, roll and pitch values are effected significantly, as shown in the noisy data at the end of the plot in Figure 5.2. This is shown with a greater impact when the IMU experiences sudden and sharp changes to orientation in Figure 5.3, where high amplitude spikes are present in the output plot, for example, when the IMU is pitched to 90° the sudden change and vibration cases a spike in roll which is inaccurate.

Following these results, the same process was repeated for the filtered accelerometer data using a LPF, where 5.4 displays the raw pitch (red) and filtered pitch (blue) to investigate into the effectiveness of the filter on the noisy accelerometer data, this was also repeated for roll data displayed in 5.5. These results correspond with the 'Filtered Pitch and Roll' test outlined in Table 8.2.

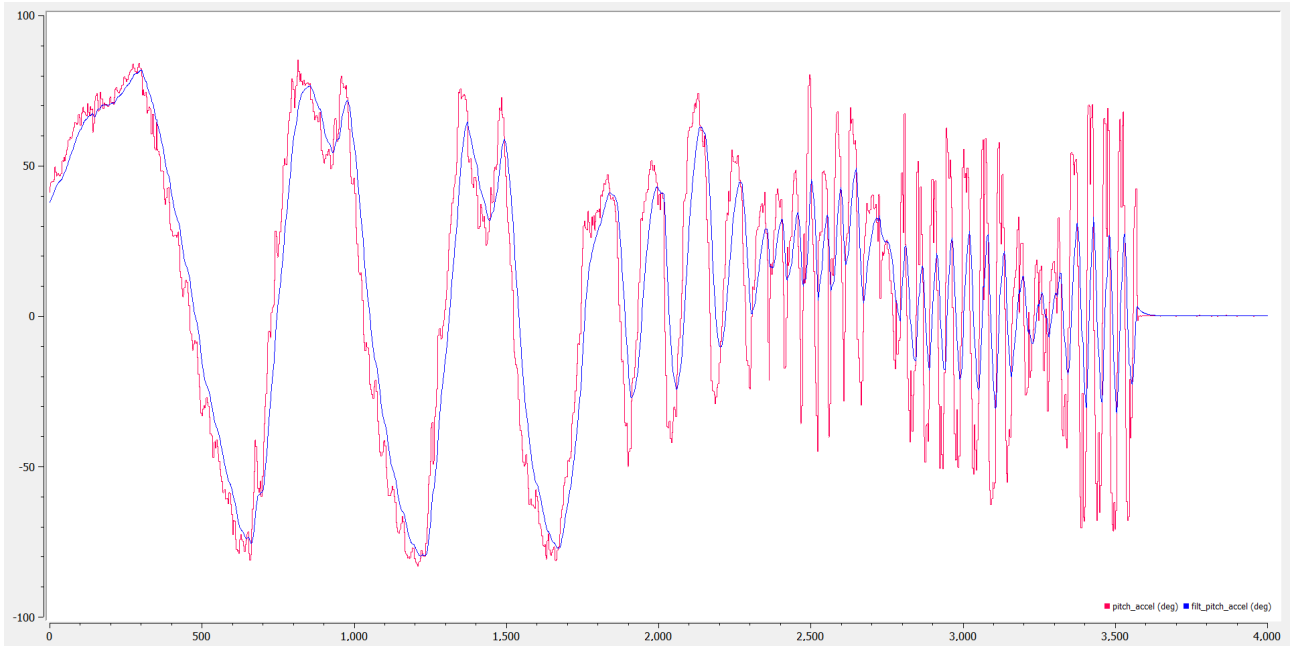


Figure 5.4: Raw pitch (red) and filtered pitch (blue) values from the accelerometer showing the effectiveness of a low-pass filter on the orientation data. IMU was pitched from 90° to -90° range and vibrated to show how the filtering improves the stability of the output

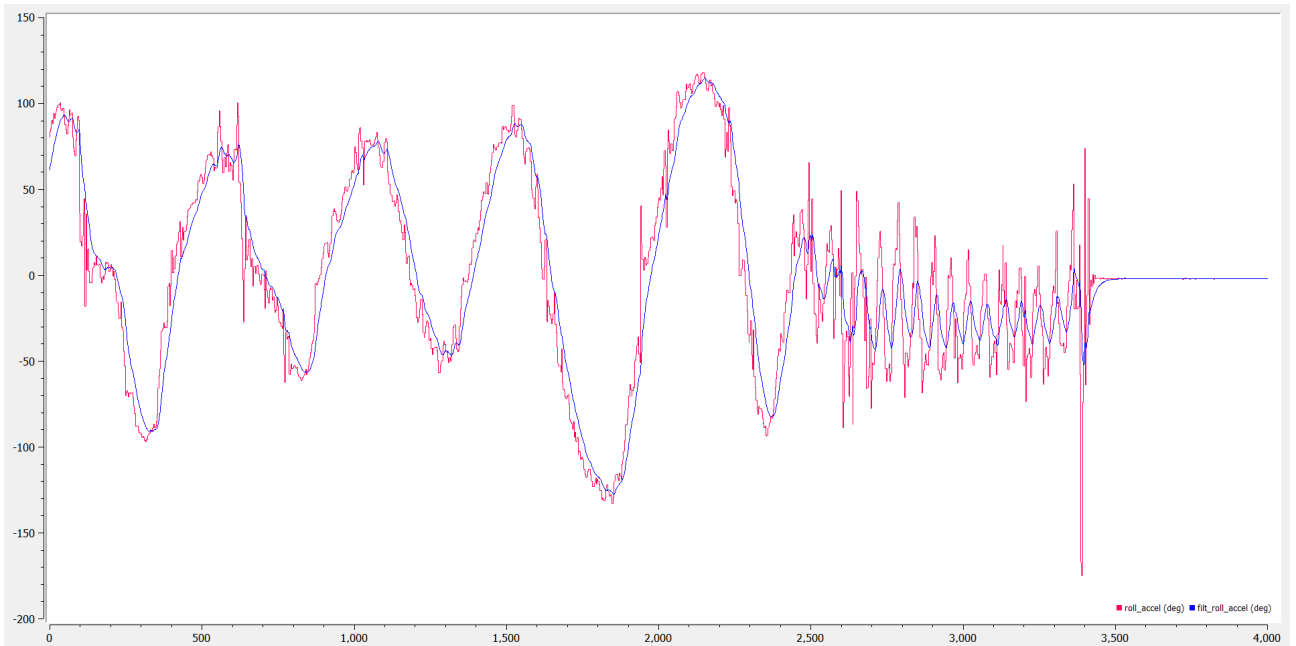


Figure 5.5: Raw roll (red) and filtered roll (blue) values from the accelerometer showing the effectiveness of a low-pass filter on the orientation data. IMU rolled from 90° to -90° range and vibrated to show how the filtering improves the stability of the output

Both figures show that the LPF implemented in the accelerometer orientation output provides a much smoother and stable plot whilst retaining the full magnitude of the pitch and roll angles that

are present in the raw plot. The effectiveness of the LPF is also shown when the IMU experiences harsh vibrations at the end of each plot where the magnitude of the filtered spike in orientation is much lower, therefore reducing the error in the results.

The final test conducted within the accelerometer testing plan was the 'Pitch and Roll Accuracy' test, where the accelerometer pitch and roll measurements had an average error of  $56.38^\circ$  and  $1.95^\circ$  respectively, shown in Figure 5.6.

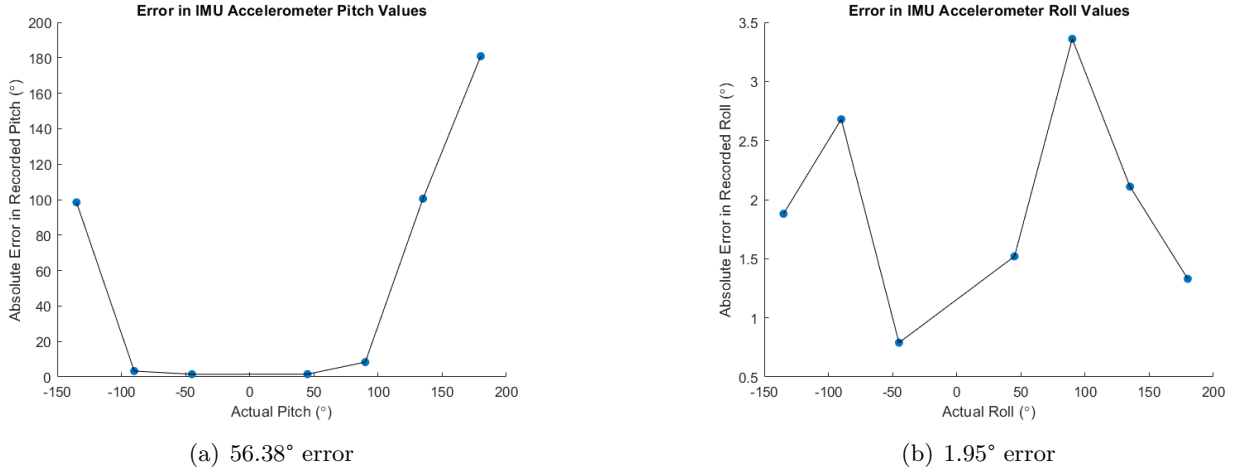


Figure 5.6: Error in recorded pitch and roll from IMU accelerometer

The results for roll error were promising, with an average recorded absolute error of  $1.95\%$ , however, it is shown that for pitch values outside the  $90^\circ$  to  $-90^\circ$  range, the recorded absolute error is significant, resulting in a an average absolute error in roll of  $56.38\%$ .

Additional testing was conducted on the accelerometer design that was not originally included within the testing plan. Following the observation of high error in IMU pitch outside the  $90^\circ$  and  $-90^\circ$  range, an additional test was conducted to investigate into this issue. These results contain the accelerometer pitch data when the IMU was pitched to  $180^\circ$  then back to rest and to  $-180^\circ$ . Figure 5.7 produced two positive and two negative peaks, where the first two peaks correspond to the IMU pitching from  $0^\circ$  to  $180^\circ$  and the following two negative peaks were formed when the IMU was pitched from  $0^\circ$  to  $-180^\circ$ .

As presented in Figure 5.7, when the IMU reaches a pitch value greater than  $90^\circ$  the output pitch value shows the IMU tending to  $0^\circ$  at  $180^\circ$  of actual IMU pitch. The same situation occurs when the IMU is pitched in the negative direction.

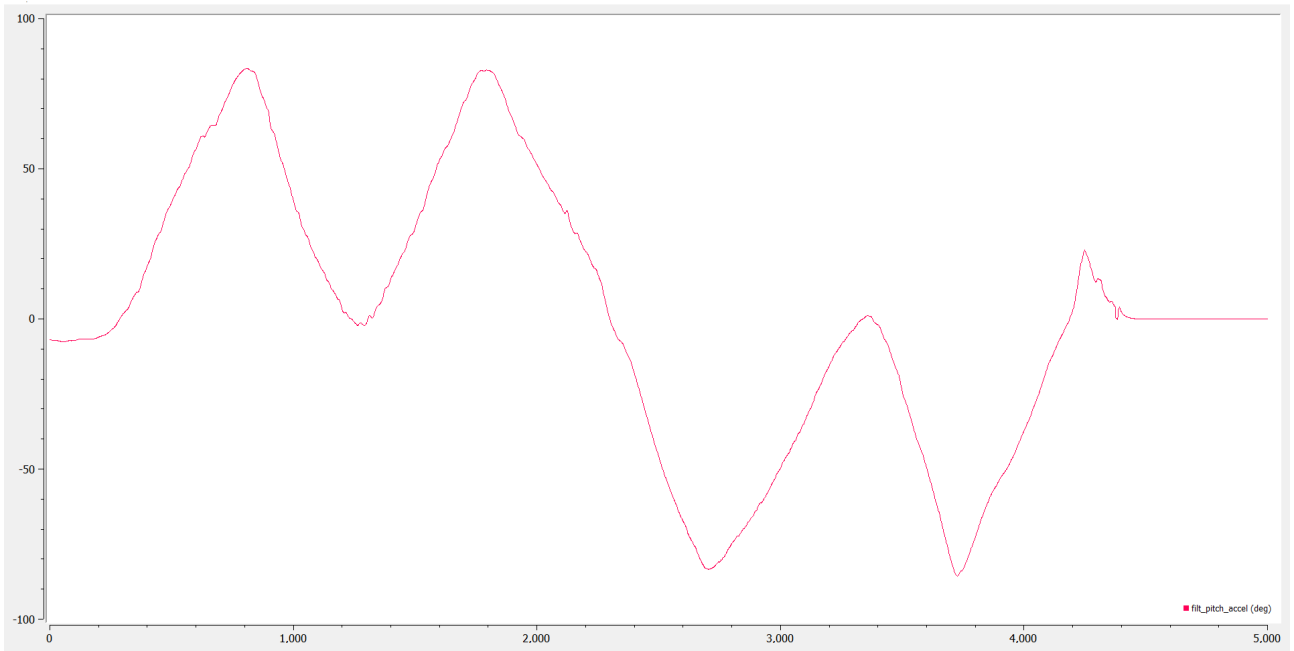


Figure 5.7: IMU accelerometer pitch. First two peaks are in the range from an actual pitch of  $0^\circ$  to  $180^\circ$  and the second two peaks are in the range from an actual pitch of  $0^\circ$  to  $-180^\circ$

### 5.2.2 Gyroscope Orientation Results

When collecting the results for the gyroscope orientation values (method described in section 3.5.2), the first results collected were the raw pitch, roll, and yaw outputs, displayed in Figure 5.8, 5.9, and 5.10 respectively. These results correspond to the 'Raw Pitch, Roll and Yaw ( $-180^\circ$  to  $180^\circ$ )' tests from the IMU Gyroscope Testing Plan, Table 8.3.

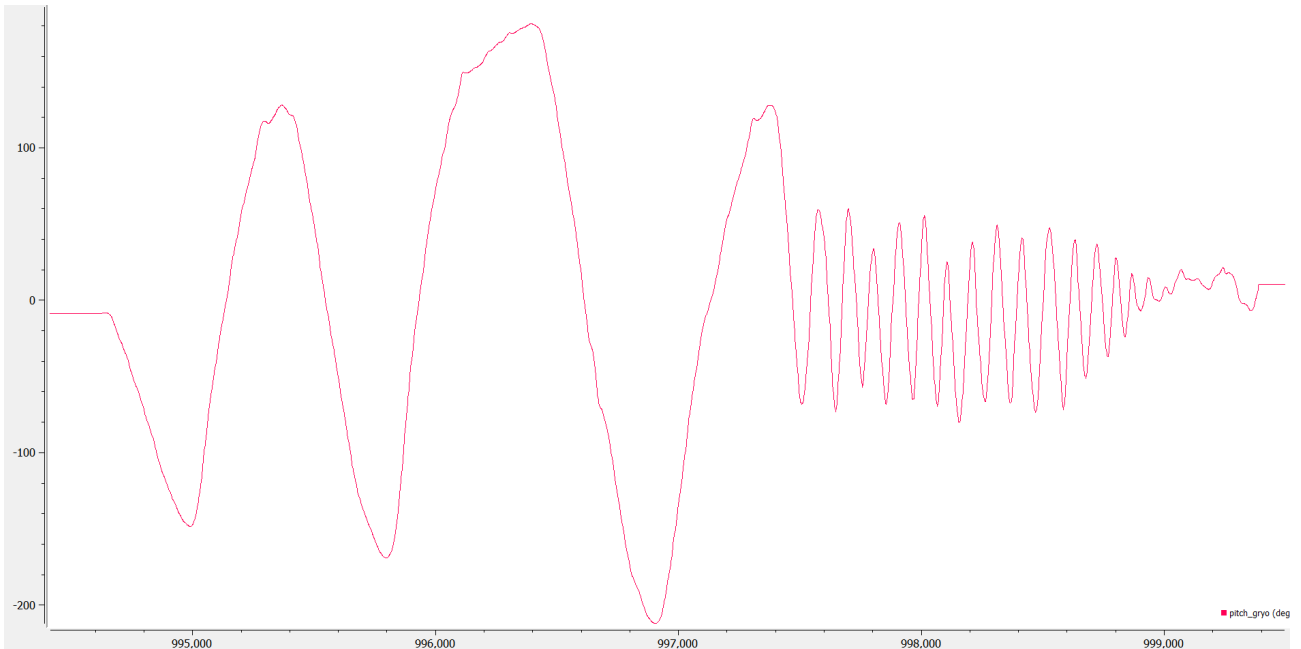


Figure 5.8: Raw pitch output from the gyroscope data. IMU was pitched within the  $-180^\circ$  and  $180^\circ$  range, followed by quick adjustments to the IMU pitch to determine the response speed

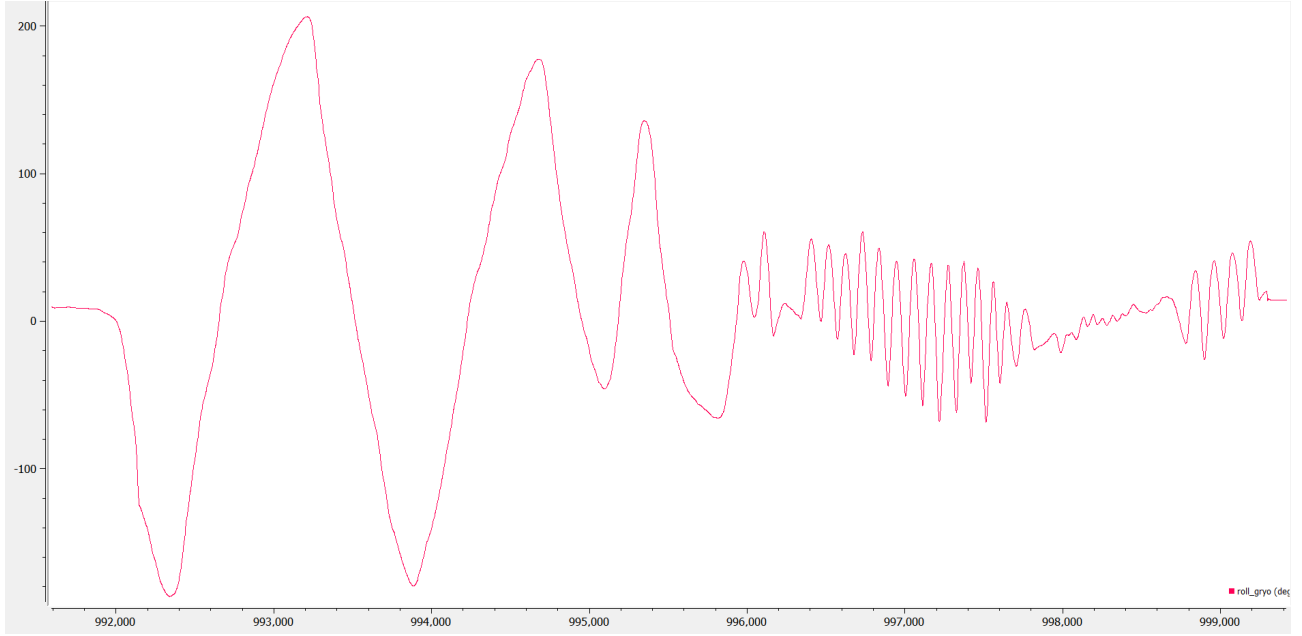


Figure 5.9: Raw roll output from the gyroscope data. IMU was rolled within the  $-180^\circ$  and  $180^\circ$  range, followed by quick adjustments to the IMU roll to determine the response speed

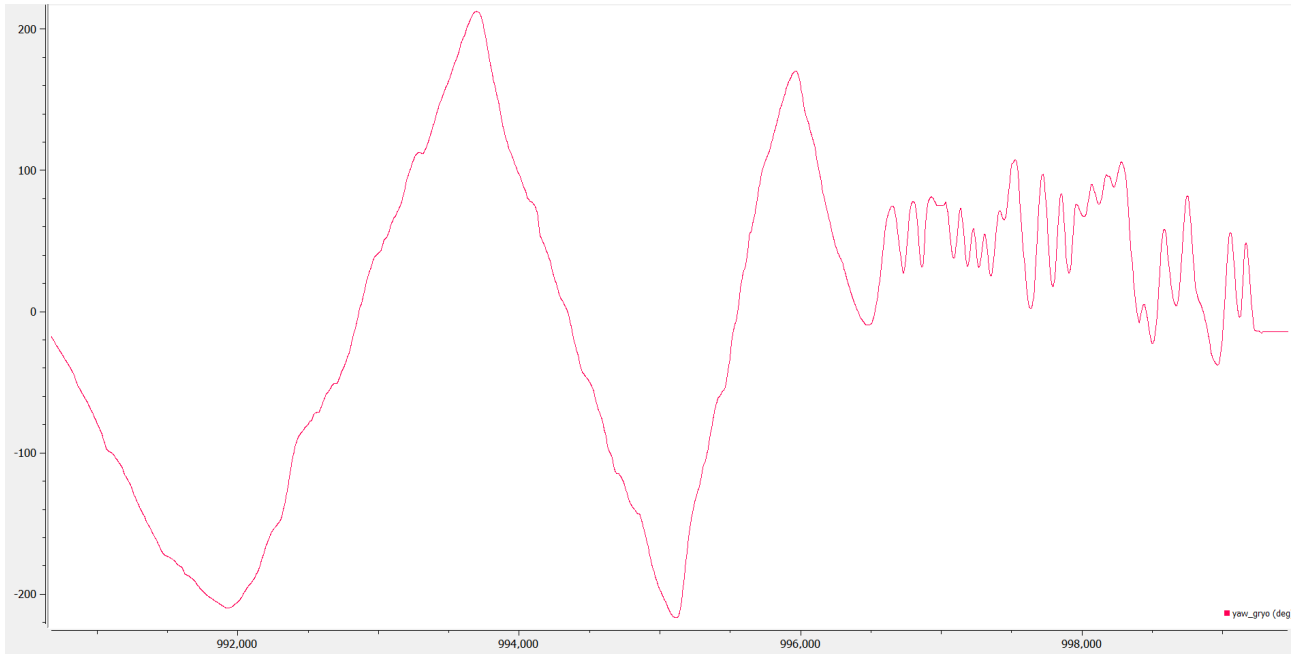


Figure 5.10: Raw yaw output from the gyroscope data. IMU was yawed within the  $-180^\circ$  and  $180^\circ$  range, followed by quick adjustments to the IMU yaw to determine the response speed

All three figures show that the gyroscope can track IMU orientation with no noise present in the data across the range of  $180^\circ$  to  $-180^\circ$ . The results also show that the gyroscope can effectively respond to sudden changes in IMU orientation, again, with no noise present in the resulting data.

The following test was used to observe the drift produced in the gyroscope output data when the IMU is subjected to a quick combination of orientation adjustments, this test corresponds to the 'Drift Observation' test within the gyroscope testing plan, and results are presented in Figure 5.11.

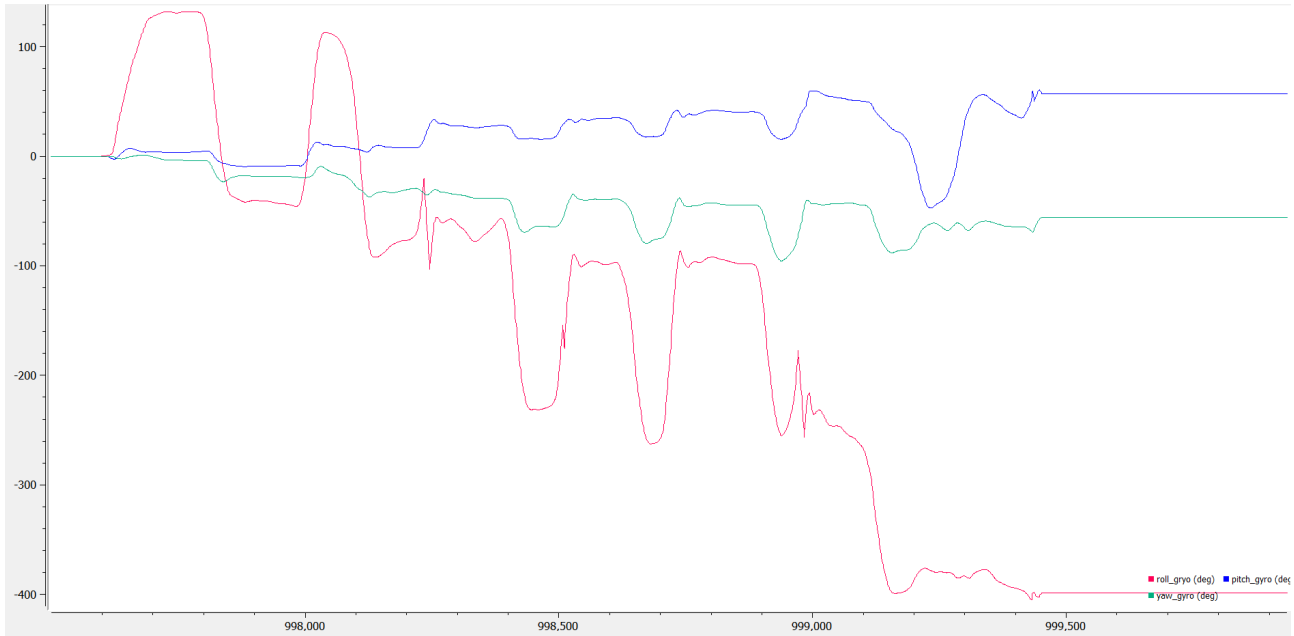


Figure 5.11: IMU subjected to sudden changes in IMU orientation to observe the effect of gyroscopic drift on the output orientation data

As discussed in the gyroscope methodology, 3.5.2, gyroscopes drift significantly over an elapsed time period which is displayed in Figure 5.11. Following the immediate changes in IMU orientation, significant drift was formed when the IMU was placed at rest with roll values drifting by  $-400^\circ$ .

The final gyroscope orientation test, 5.12, determines the error in recorded gyroscope orientation values, in line with the 'Pitch, Roll and Yaw Accuracy' test within the gyroscope testing plan.

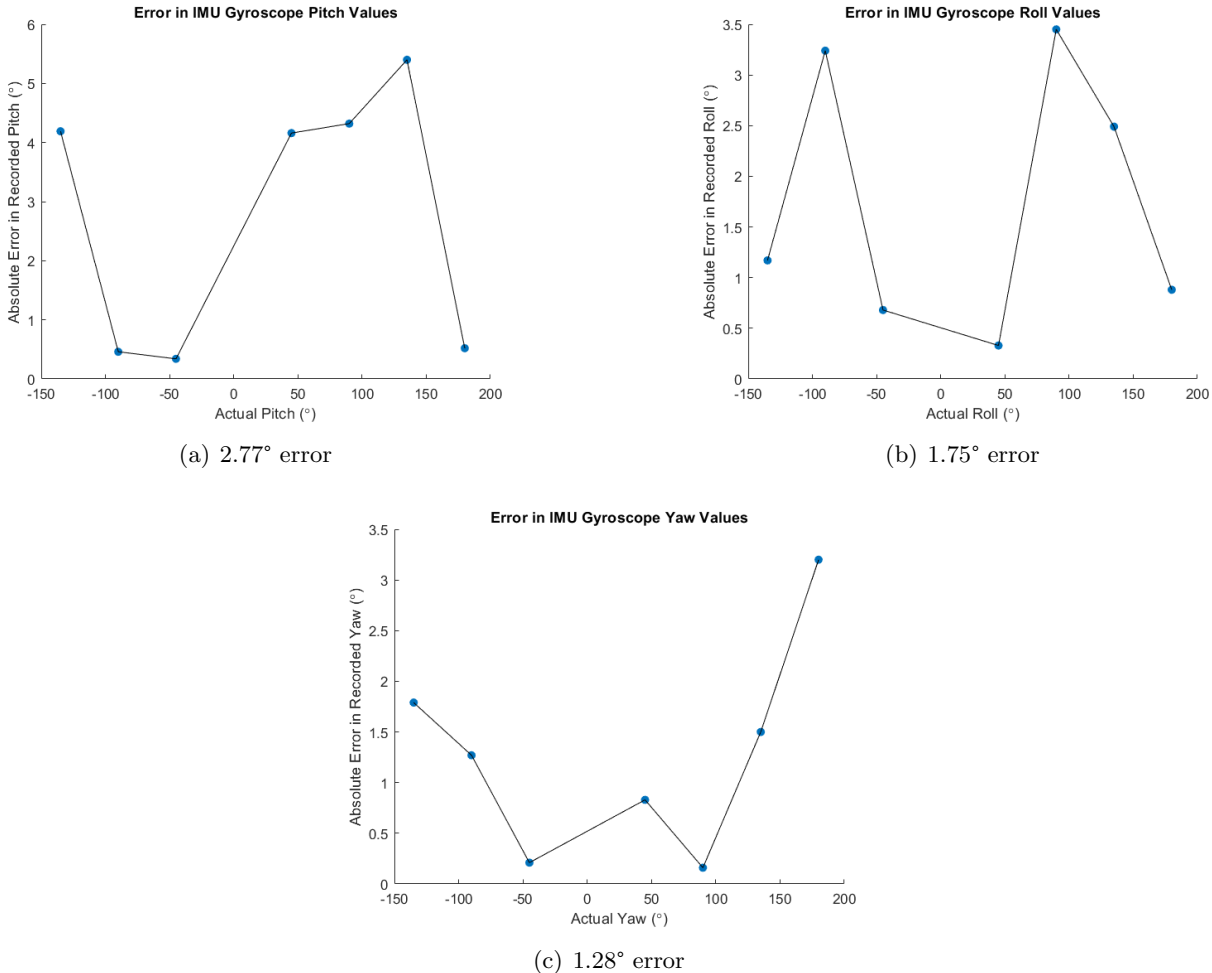


Figure 5.12: Error in recorded pitch, roll, and yaw from IMU gyroscope

It was found that there was an absolute error of  $2.77^\circ$ ,  $1.75^\circ$ , and  $1.28^\circ$  in pitch, roll, and yaw respectively for the gyroscope orientation data. Whilst gyroscopes are prone to drifting with recorded data, these error results show the impressive accuracy of this method. However, it is assumed that some drift error is present within these results.

### 5.2.3 Magnetometer Orientation Results

Since the magnetometer yaw equation, (3.19), is reliant on both roll and pitch to determine the horizontal and vertical components of the magnetometer, testing was conducted using the gyroscope roll and pitch values.

The first set of results collected were recorded in the range of  $180$  to  $-180^\circ$  yaw, which is in line with the 'Raw Yaw from Magnetometer (with Gyroscope Pitch and Roll) ( $-180^\circ$  to  $180^\circ$ )' test outlined in the magnetometer testing plan, Table 8.4. The results for this test are shown in Figure 5.13.

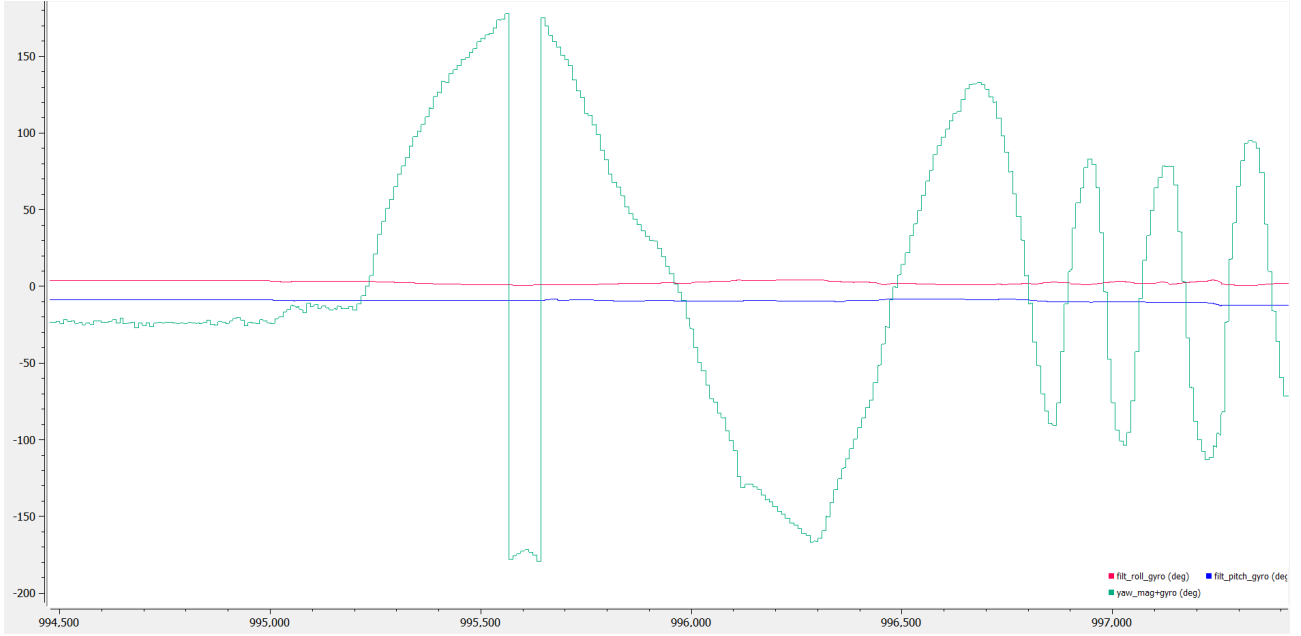


Figure 5.13: Magnetometer and gyroscope combination to calculate IMU yaw values. IMU was yawed within the  $-180^\circ$  and  $180^\circ$  range, followed by quick adjustments to the IMU yaw to determine the response speed

Results presented in Figure 5.13 are positive, showing accuracy with tracking the yaw values and a satisfactory response with prompt yaw adjustments. However, since the gyroscope is prone to drift, roll and pitch values used to determine the IMU yaw could be inaccurate, introducing error into the calculated yaw using the magnetometer.

Following this test, the effect of roll and pitch on the yaw output for the magnetometer and gyroscope combination was investigated, shown in Figure 5.14.

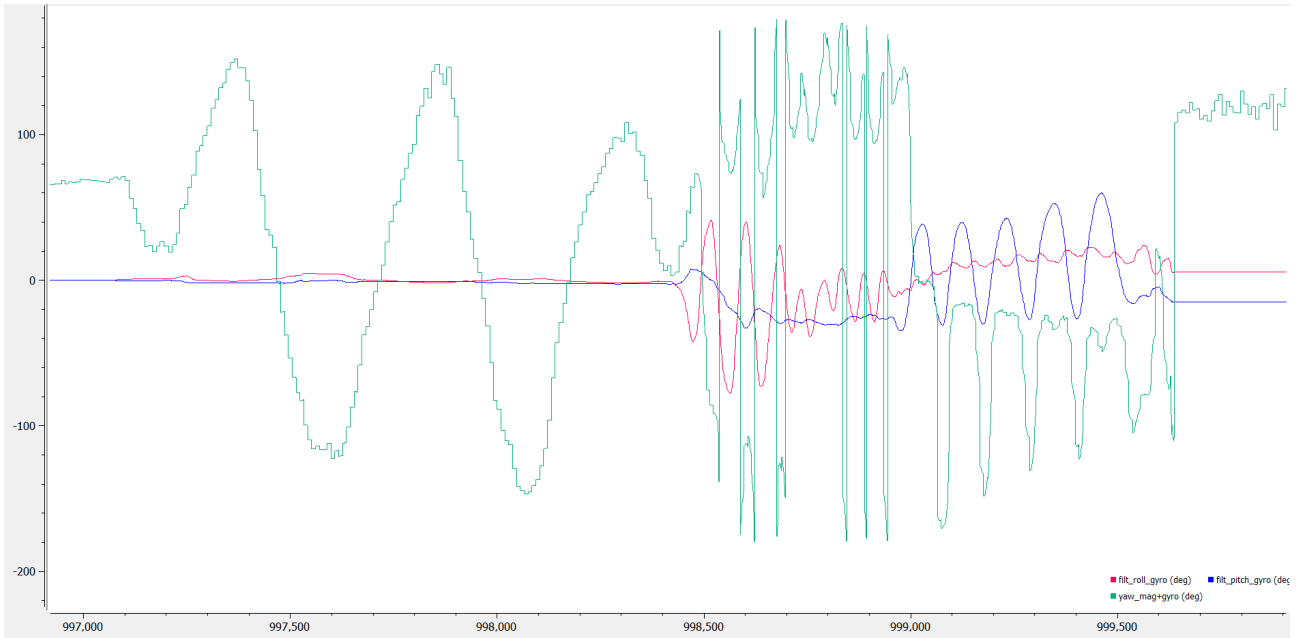


Figure 5.14: Magnetometer and gyroscope combination displaying the effect of roll and pitch on the yaw output

This figure shows that the gyroscope roll and pitch values have significant influence on the calculated magnetometer yaw output, resulting in a large number of high amplitude spikes in the plot. The effect of gyroscope drift is also shown in this figure where the roll and pitch plots (red and blue respectively) drifted from their starting value, causing the final yaw value to drift from the original starting yaw value (by approximately +40°).

The effect of electromagnetic interference was next tested since the main limitation of the magnetometer was due to iron biases, as stated in the methodology 3.5.3. Results produced for this test were in line with the magnetometer testing plan (Table 8.4), shown in Figure 5.15. This figure displays the immense influence electromagnetic interference has on the raw magnetometer yaw values causing the yaw output to reach 180° and -180° whilst remaining at an actual yaw value of 0°.

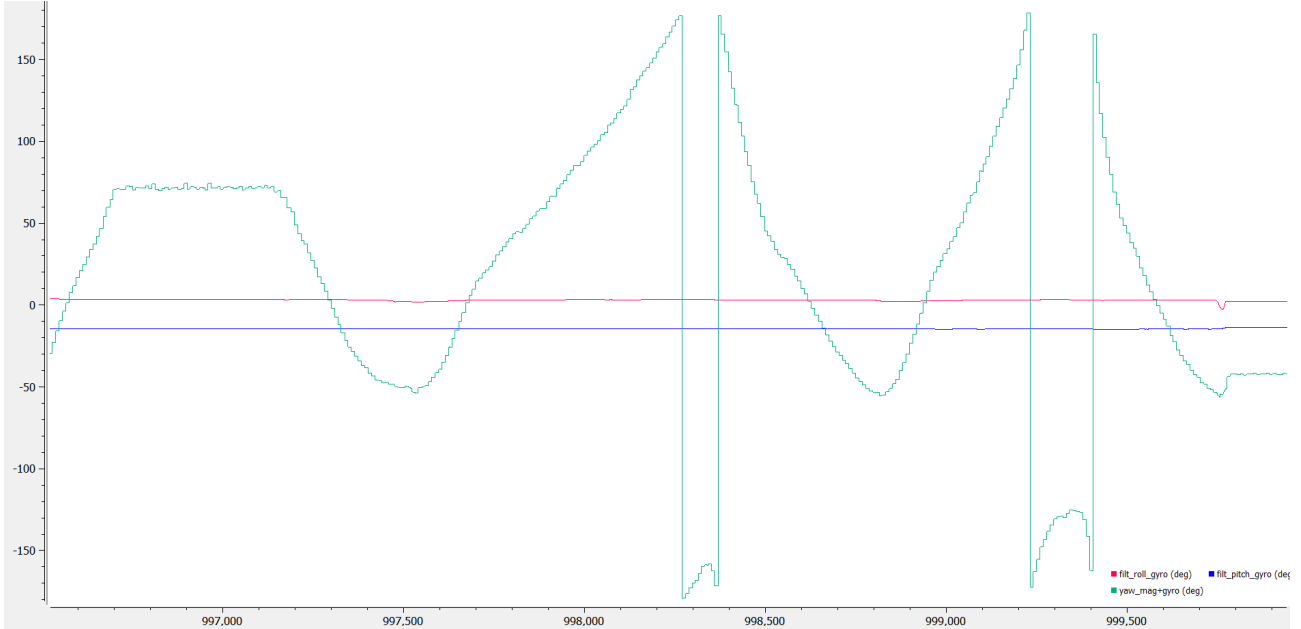


Figure 5.15: Magnetometer and gyroscope combination displaying the effect of electromagnetic interference on the yaw output

The final test conducted for the magnetometer and gyroscope combination was the 'Magnetometer Yaw Accuracy' outlined in the testing plan, Table 8.4. The results of this test produced an average absolute error of 2.03° in the resulting yaw values shown in Figure 5.16. This test produced promising results displaying high accuracy. However, there is a possibility that the accuracy of data could have been effected by electromagnetic interference, as shown in previous testing.

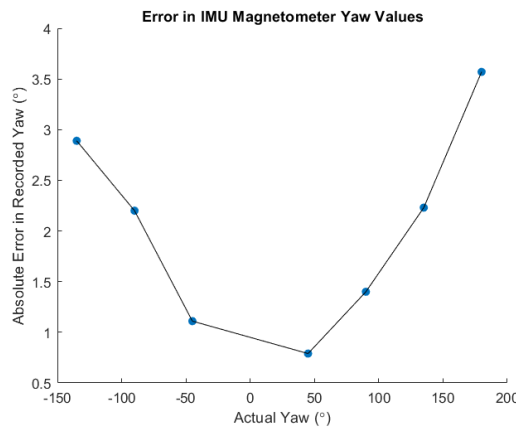


Figure 5.16: Average absolute error of 2.03° for the magnetometer and gyroscope combination to calculate IMU yaw

#### 5.2.4 Complementary Filter Orientation Results

This section of the results contains three separate tests to evaluate the effectiveness of the complementary filter design. The first test completed recorded the design's roll, pitch, and yaw values obtained in the range of  $180^\circ$  to  $-180^\circ$ . For testing the design's robustness to mechanical noise (vibrations) due to the accelerometer and drift from the gyroscope, the IMU orientation in all axes was adjusted rapidly. To validate the reduced effect of electromagnetic interference in yaw values from the magnetometer, an electronic device was placed near the IMU and positioned at various points during the test. These results are shown in Figure 5.17.

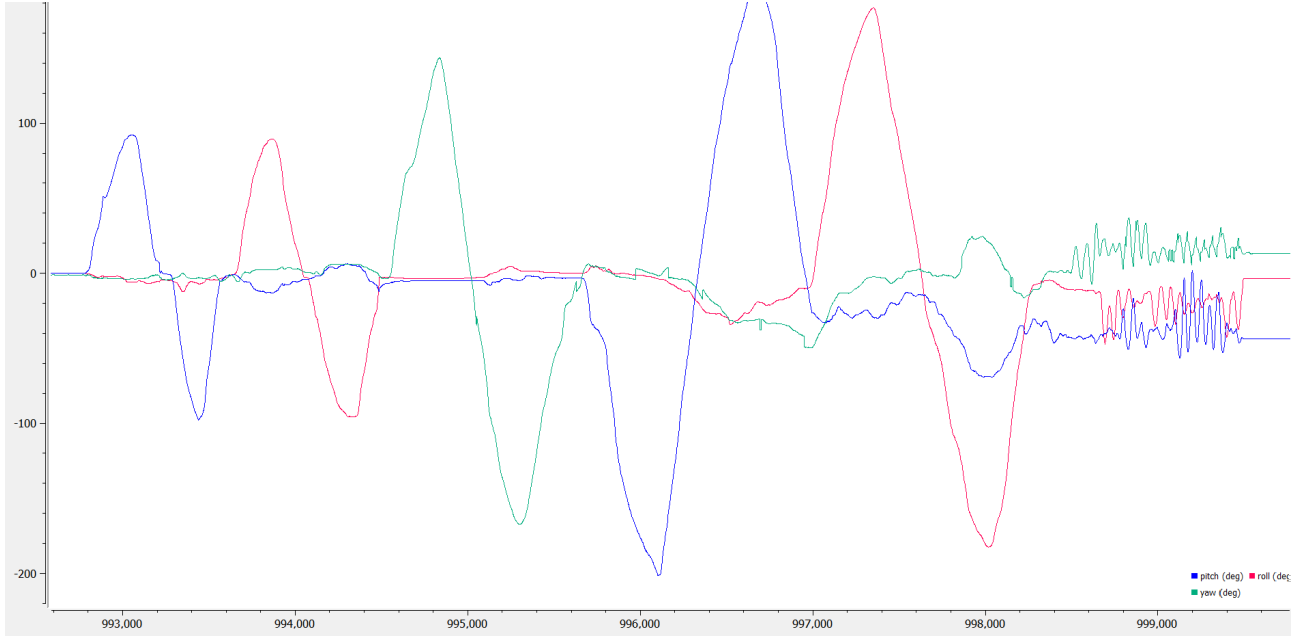


Figure 5.17: Complementary filter orientation results for roll, pitch, and yaw in the  $180^\circ$  and  $-180^\circ$  range. Results also show the effectiveness of the design against sources of error within the IMU sensor

Results displayed in Figure 5.17 shows that the complementary filter can track roll, pitch, and yaw in the range of  $180^\circ$  to  $-180^\circ$  with ease. In addition, the complementary filter removed the sources of error present in the other sensors' results, where little noise, electromagnetic interference, and drift was produced in Figure 5.17.

To support with the comparison of the complementary filter to the other methods to determine the IMU orientation, the accuracy tests were conducted, where the results for these tests are shown below in Figure 5.18. These results produced an average absolute error of  $0.63^\circ$  in pitch,  $2.00^\circ$  in roll, and  $1.43^\circ$  in yaw for this method, showing the significant gains in the accuracy through this sensor fusion method.

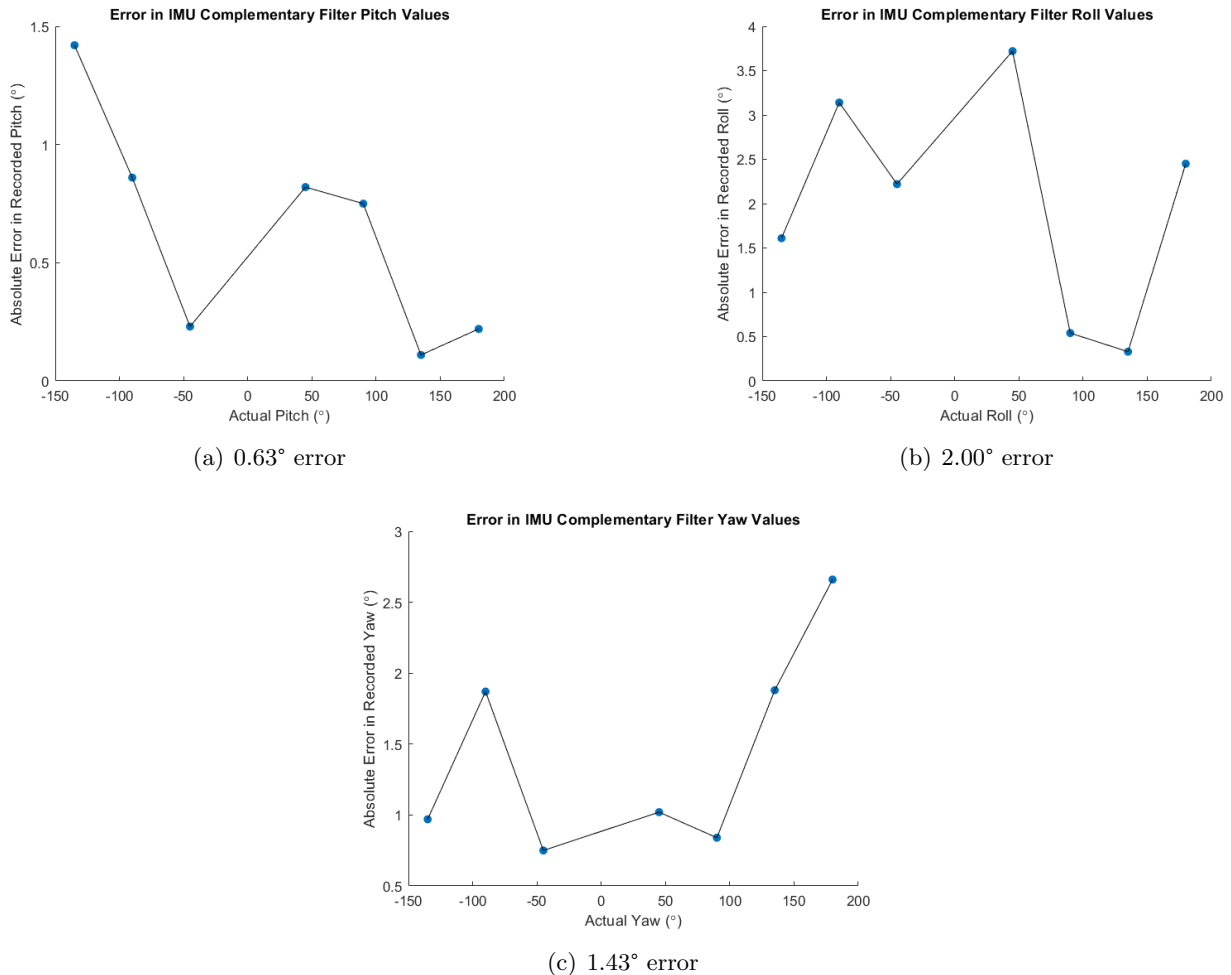
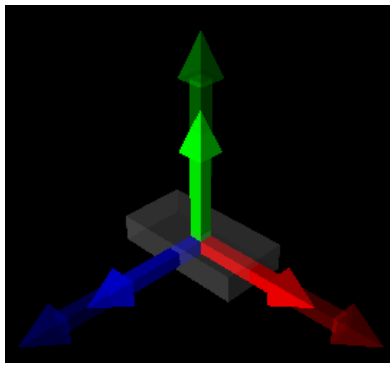
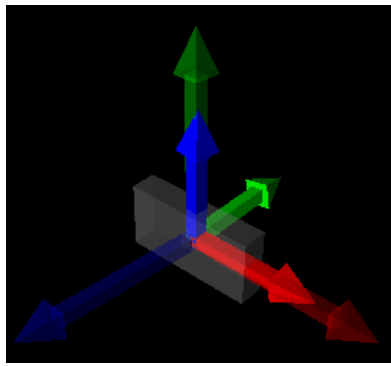


Figure 5.18: Error in recorded pitch and roll from IMU complementary filter

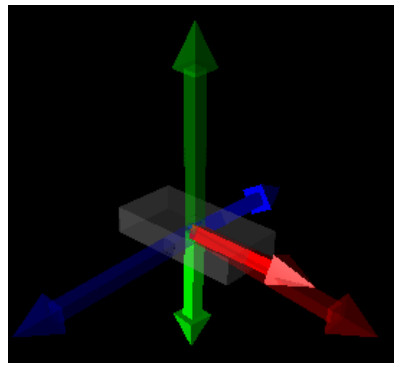
To further investigate into the performance of the complementary filter, a real-time 3-D rendering of the IMU was produced and animated to represent the real orientation of the IMU in space (Figure 5.19), as outlined in the complementary filter testing plan in Table 8.5.



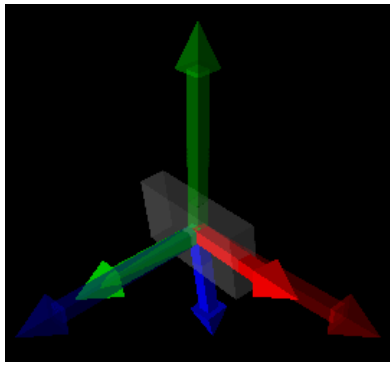
(a) 0° Roll, 0° Pitch, 0° Yaw



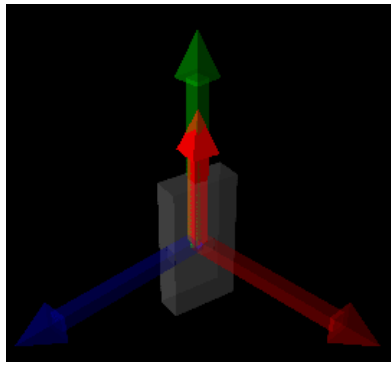
(b) 90° Roll, 0° Pitch, 0° Yaw



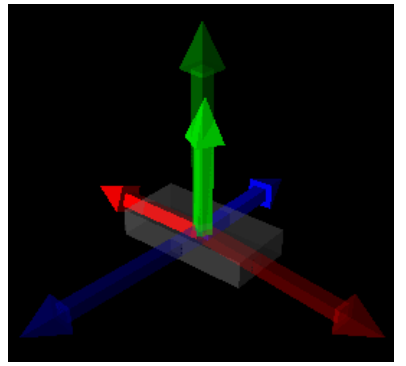
(c) 180° Roll, 0° Pitch, 0° Yaw



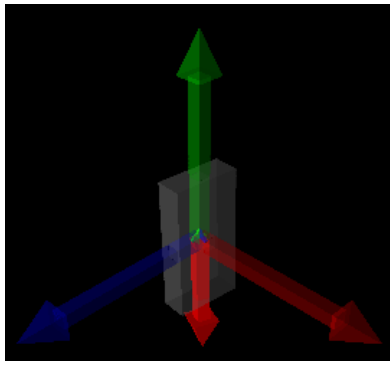
(d) -90° Roll, 0° Pitch, 0° Yaw



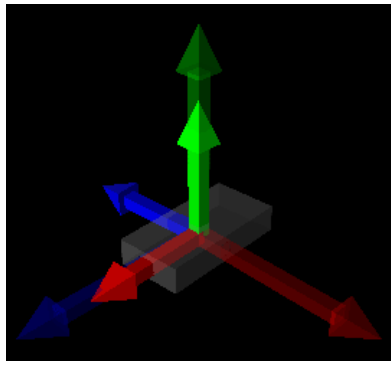
(e) 0° Roll, 90° Pitch, 0° Yaw



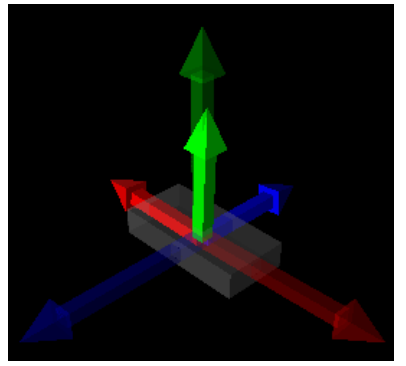
(f) 0° Roll, 180° Pitch, 0° Yaw



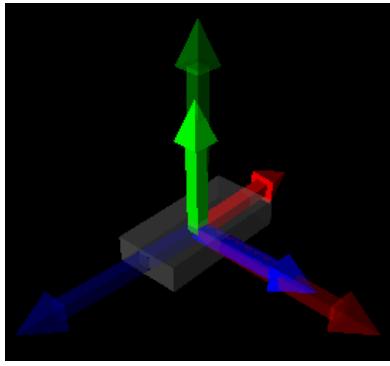
(g) 0° Roll, -90° Pitch, 0° Yaw



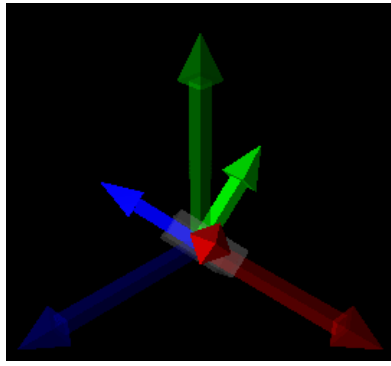
(h) 0° Roll, 0° Pitch, 90° Yaw



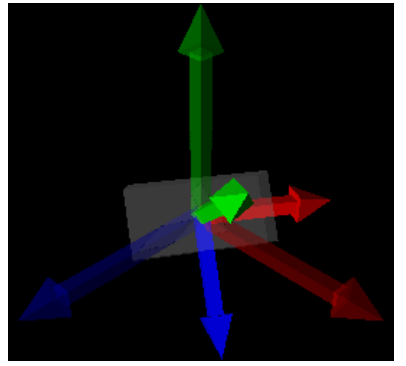
(i) 0° Roll, 0° Pitch, 180° Yaw



(j) 0° Roll, 0° Pitch, -90° Yaw



(k) 45° Roll, 45° Pitch, 45° Yaw



(l) -45° Roll, -45° Pitch, -45° Yaw

Figure 5.19: Live animation of numerous 3-D orientation plots from the complementary filter method (transparent axes are the reference axes for orientation adjustments)

Within Figure 5.19 above, plot (f) represents  $180^\circ$  in pitch, however, the plot shown is identical to that presented in plot (i) for  $180^\circ$  in yaw, this is an example of gimbal lock present within this system. Excluding this issue, all other plots are as expected, with success in a combination of rotations in the positive and negative directions, whilst the animation remaining relatively smooth and stable over a short time period. However, drift formed by the gyroscope was noticeable after a short period of time, increasing the difficulty of obtaining the desired orientation.

### 5.2.5 Quaternion Orientation Results

Similarly to the testing completed and results obtained from the other methods to determine IMU orientation, the quaternion orientation method (3.5.5) was also tested against the tests outlined in the testing plan, Table 8.6.

As stated in the testing plan, the first test completed was the 'Raw Pitch, Roll and Yaw (-180° to 180°)' test. This is where the IMU orientation was tested within the  $\pm 180^\circ$  range and for roll, pitch, and yaw at both gradual and rapid adjustments in orientation. Figures 5.20, 5.21, 5.22, 5.23, 5.24, and 5.25 were all produced to support with this testing.

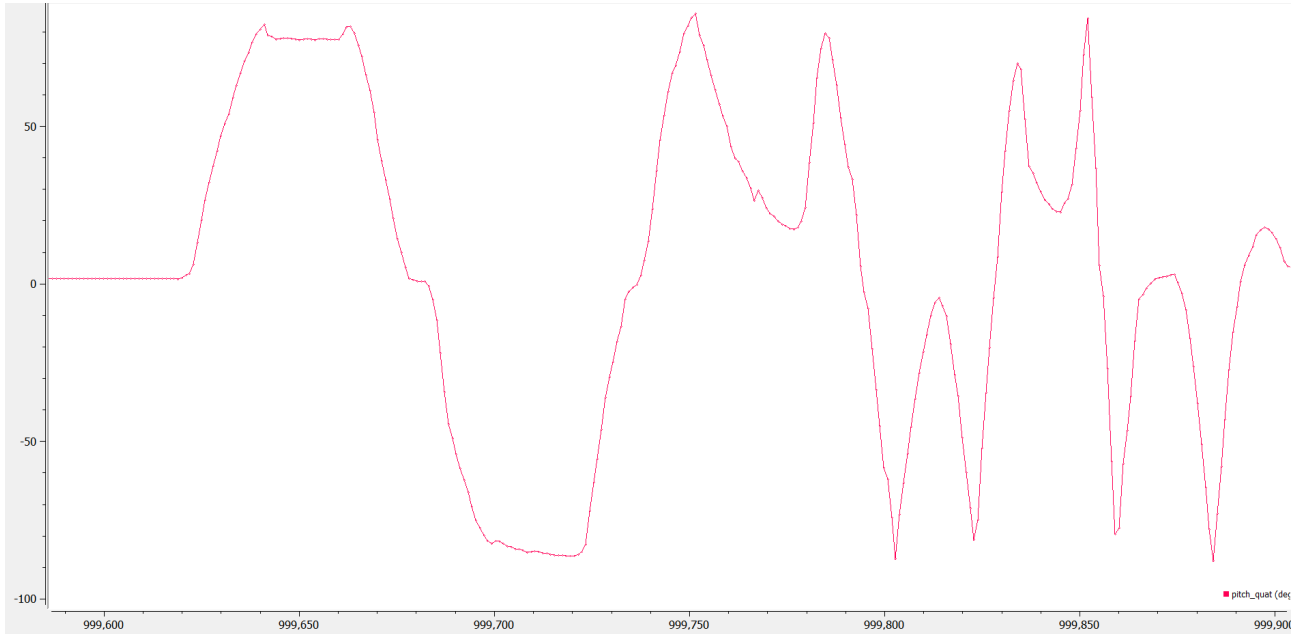


Figure 5.20: Pitch calculated from quaternion data. First positive and negative peaks are at an actual pitch of  $90^\circ$  and  $-90^\circ$ . The following sets of peaks are within the range of  $180^\circ$  to  $-180^\circ$

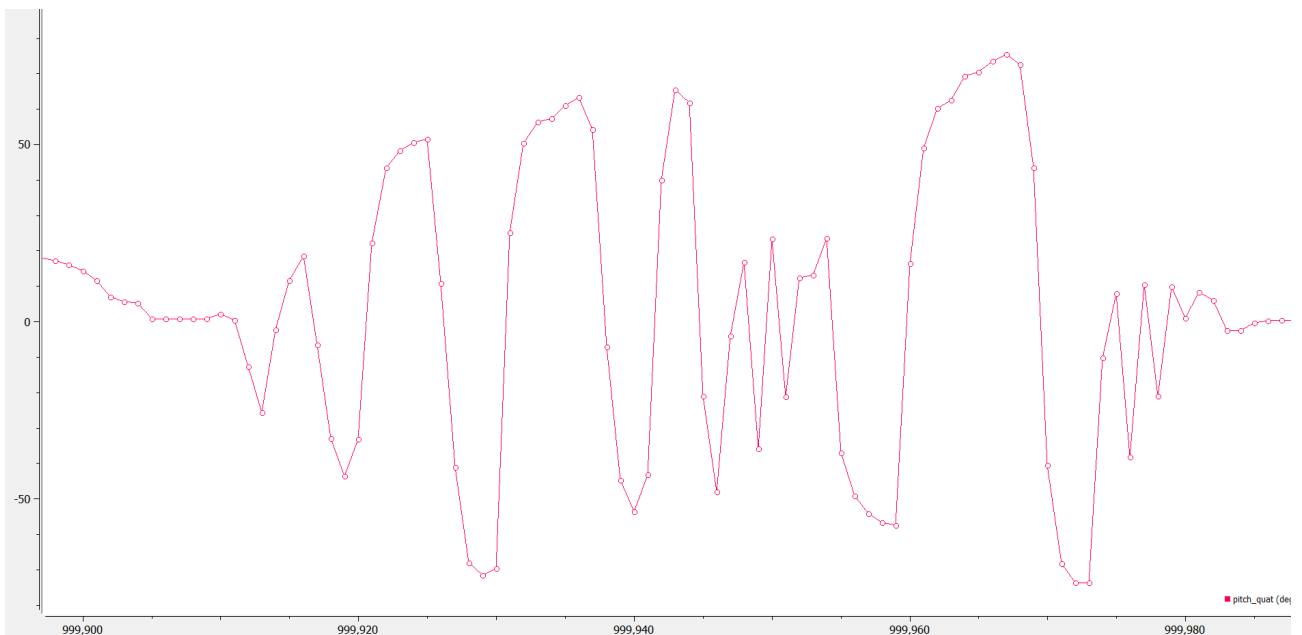


Figure 5.21: Pitch calculated from the quaternion data following instantaneous changes to IMU pitch within the range of  $90^\circ$  and  $-90^\circ$

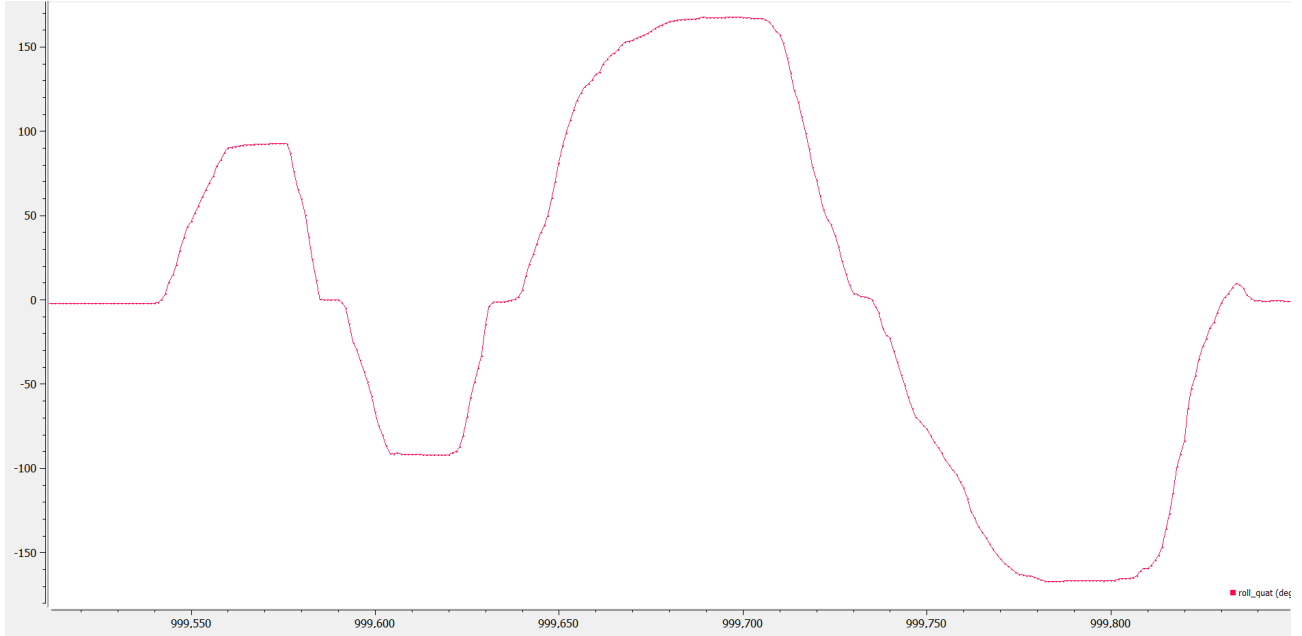


Figure 5.22: Roll calculated from quaternion data. First positive and negative peaks are at an actual roll of  $90^\circ$  and  $-90^\circ$ . The following sets of peaks are within the range of  $180^\circ$  to  $-180^\circ$

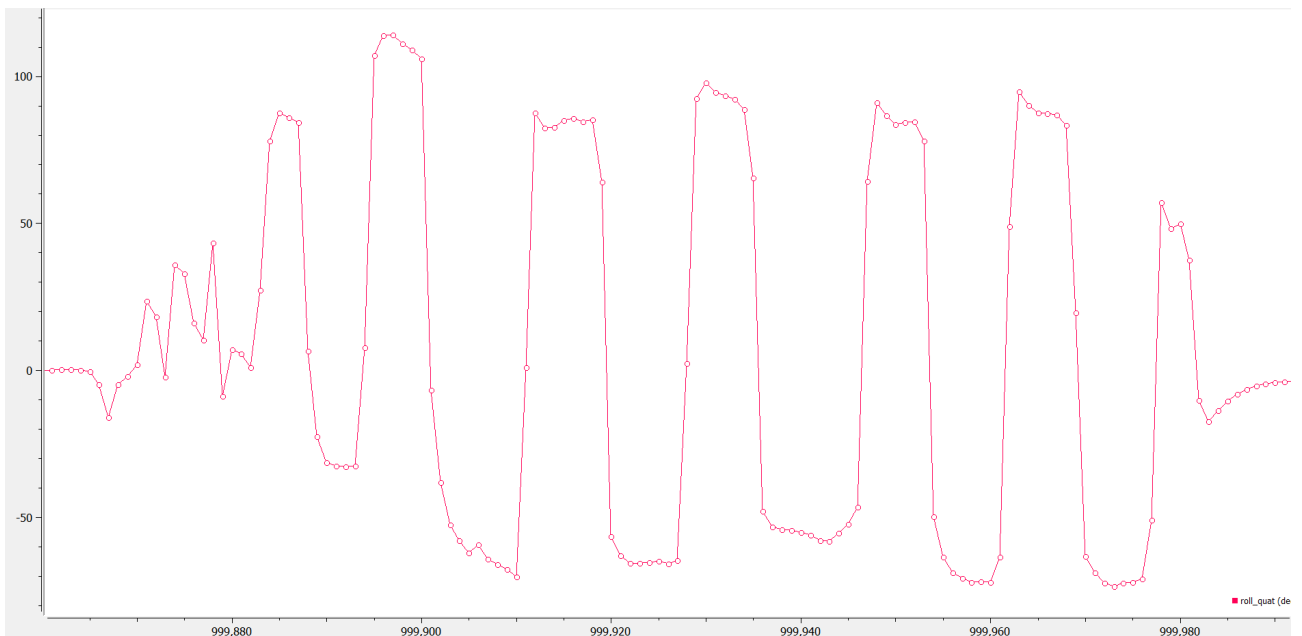


Figure 5.23: Roll calculated from the quaternion data following instantaneous changes to IMU Roll within the range of  $180^\circ$  and  $-180^\circ$

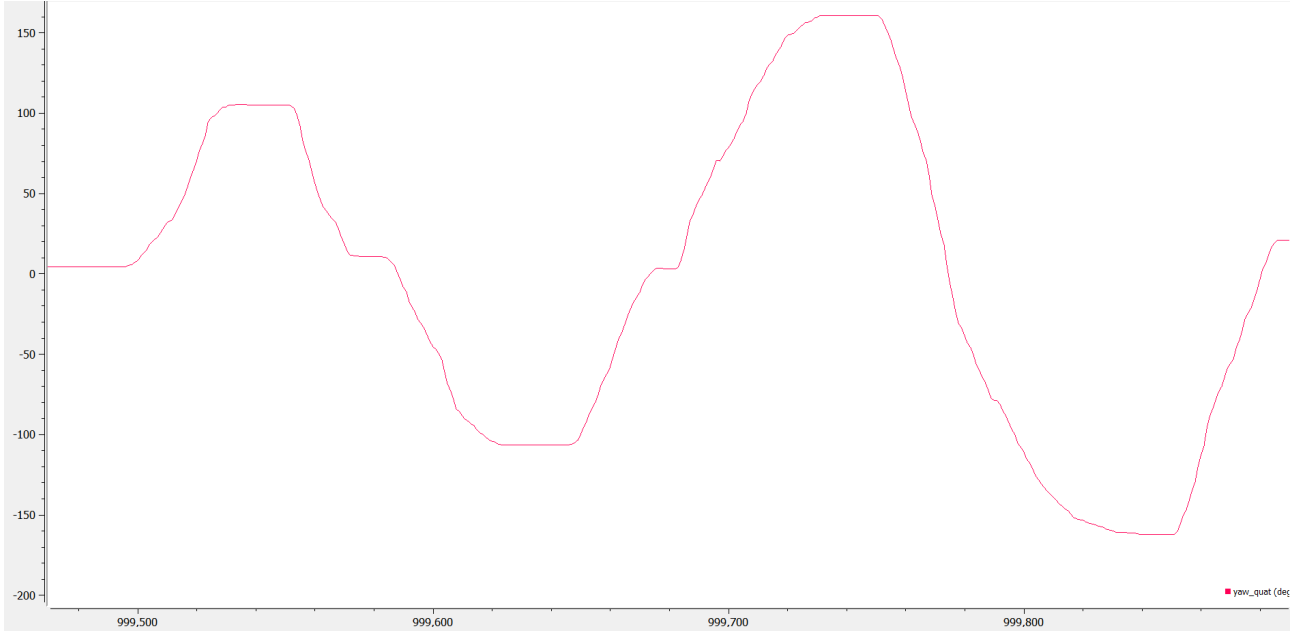


Figure 5.24: Yaw calculated from quaternion data. First positive and negative peaks are at an actual yaw of  $90^\circ$  and  $-90^\circ$ . The following sets of peaks are within the range of  $180^\circ$  to  $-180^\circ$

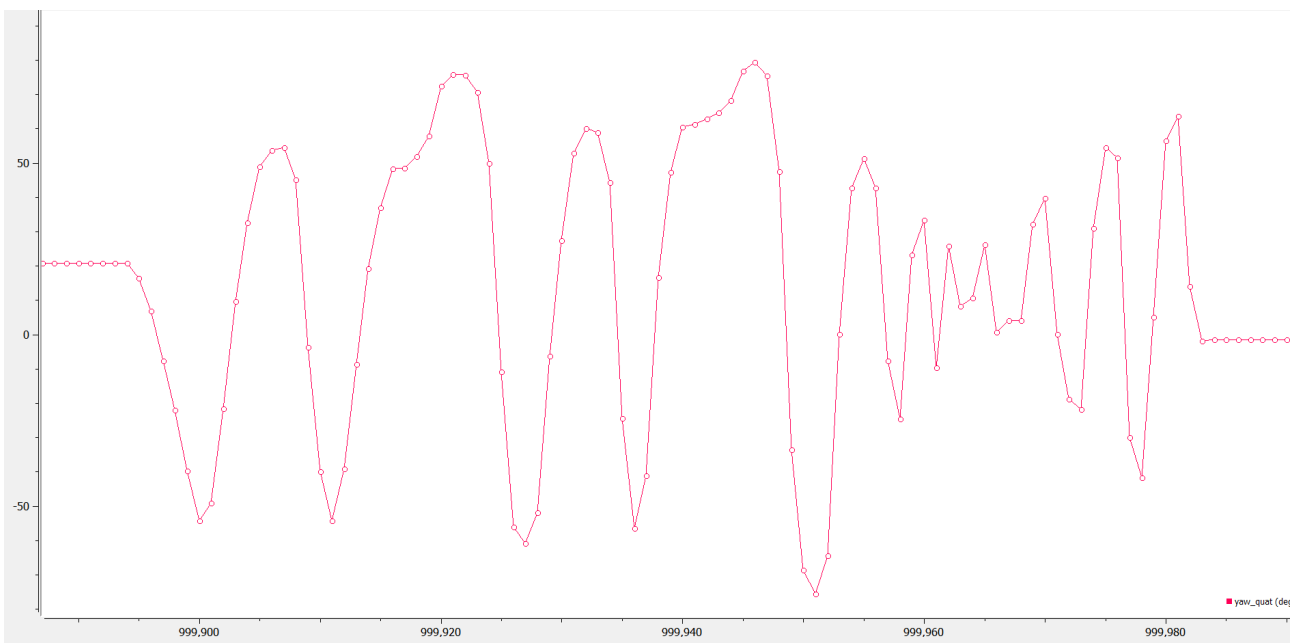


Figure 5.25: Yaw calculated from the quaternion data following instantaneous changes to IMU yaw within the range of  $90^\circ$  and  $-90^\circ$

All plots associated with displaying the output orientation from the quaternion method provide smooth output which followed the actual IMU orientation. The design responded rapidly to changes in the orientation (shown by the steep curves in Figures 5.23, 5.21, and 5.25) with no noise, drift or changes due to electromagnetic interference. The only plot that produced undesirable results was 5.20 where similar results were also produced in the accelerometer pitch testing in Figure 5.7.

To support with the comparison of the quaternion orientation method to the other methods explored, the 'Pitch, Roll and Yaw Accuracy' test was conducted in line with the testing plan. Results for this are shown below in Figure 5.26. These results produced an average absolute error of  $65.08^\circ$  in pitch,  $0.37^\circ$  in roll, and  $1.51^\circ$  in yaw for this method.

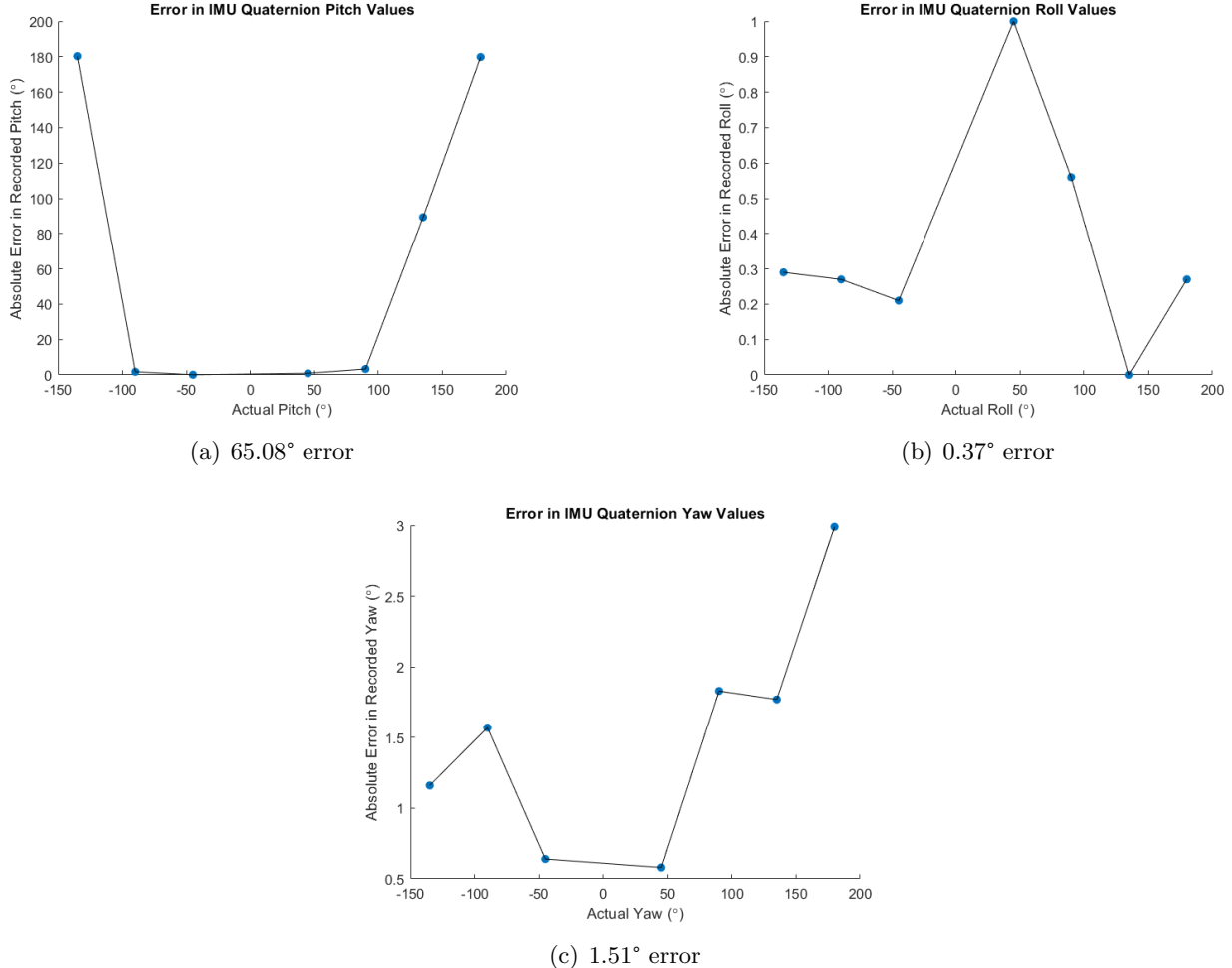
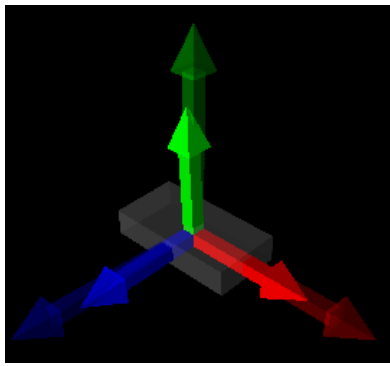


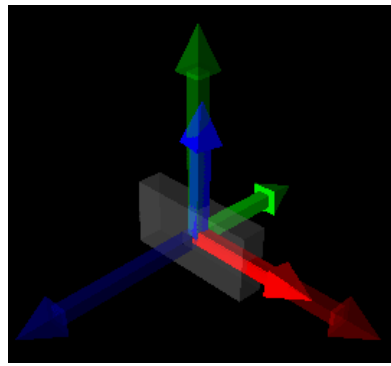
Figure 5.26: Error in recorded pitch and roll from IMU quaternions

The cause of high error in the quaternion pitch error is due to conversion from quaternions to Euler angles in equation (3.23) when actual pitch values are not within the range of  $\pm 90^\circ$ .

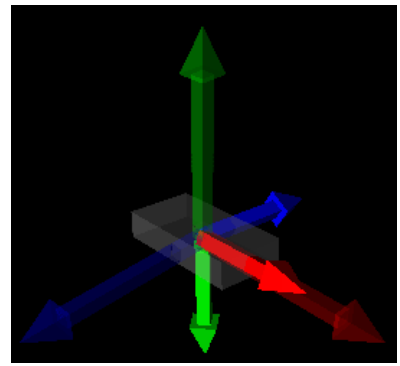
To further investigate into the performance of the quaternion orientation method, a 3-D rendering of the IMU was produced and animated to represent the real orientation of the IMU in space, as outlined in the quaternion testing plan in Table 8.6.



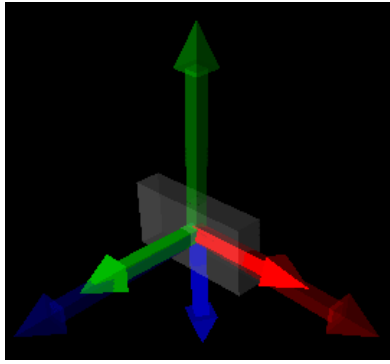
(a) 0° Roll, 0° Pitch, 0° Yaw



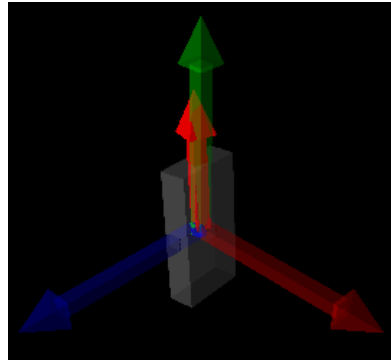
(b) 90° Roll, 0° Pitch, 0° Yaw



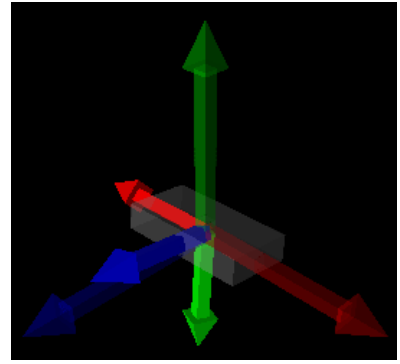
(c) 180° Roll, 0° Pitch, 0° Yaw



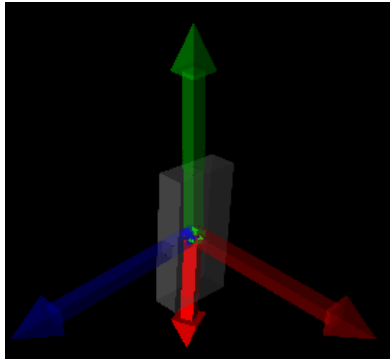
(d) -90° Roll, 0° Pitch, 0° Yaw



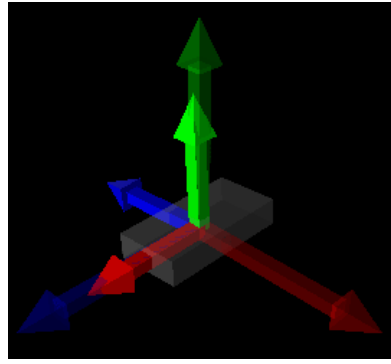
(e) 0° Roll, 90° Pitch, 0° Yaw



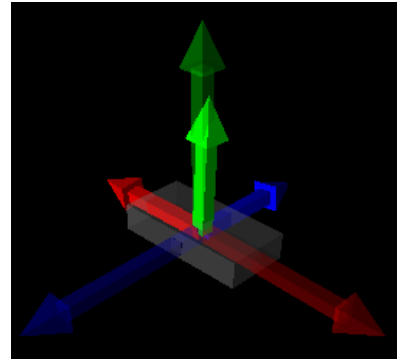
(f) 0° Roll, 180° Pitch, 0° Yaw



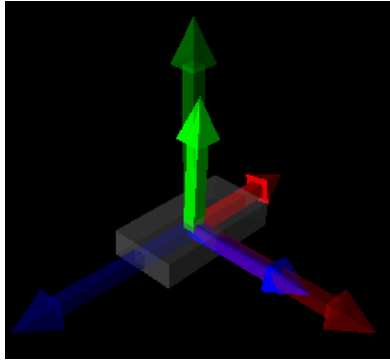
(g) 0° Roll, -90° Pitch, 0° Yaw



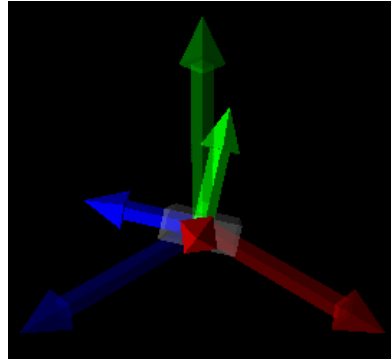
(h) 0° Roll, 0° Pitch, 90° Yaw



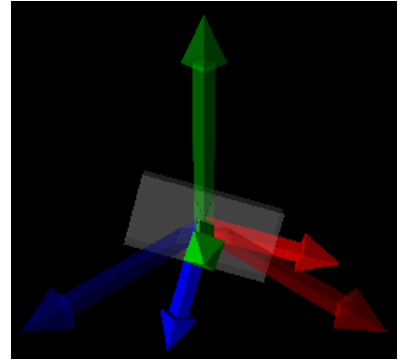
(i) 0° Roll, 0° Pitch, 180° Yaw



(j) 0° Roll, 0° Pitch, -90° Yaw



(k) 45° Roll, 45° Pitch, 45° Yaw



(l) -45° Roll, -45° Pitch, -45° Yaw

Figure 5.27: Live animation of numerous 3-D orientation plots from the quaternion method (transparent axes are the reference axes for orientation adjustments)

Results collected in Figure 5.27 were accurate to the actual orientation that the IMU was placed in. The animation ran flawlessly with no issues, stuttering, or drift in the output like that experienced in the complementary filter results, in Figure 5.19.

## 5.3 Onboard IMU Position Results

### 5.3.1 Euler and Quaternion Rotation Matrix Position Results

Using the rotation matrices derived by Euler angles and quaternions outlined in equations (3.8) and (3.11), the IMU position was derived using the accelerometer's acceleration values in the X, Y and Z directions. The test involves the translation of the IMU in a 30x30x30cm area reaching each corner (outlined in the testing plan), which produced Figures 5.28 and 5.29 below.

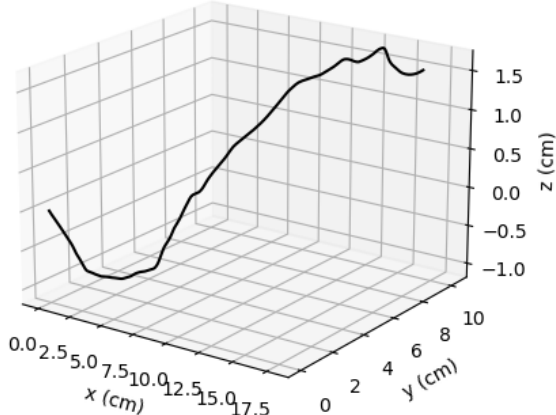


Figure 5.28: Euler Position Testing: 30cmx30cmx30cm

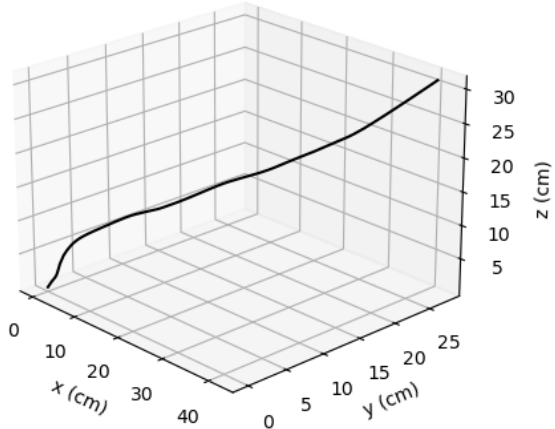


Figure 5.29: Quaternion Position Testing: 30cmx30cmx30cm

The results for the Euler rotation matrix were unsatisfactory, with the Z values dropping to -1cm and not exceeding 1.5cm, when the IMU was at an actual value of 30cm. The maximum X and Y values were also both inaccurate by 15cm and 20cm respectively.

For the same .csv data file, the quaternion plot produced more desirable results (Figure 5.29), where it produced a minimum X, Y, and Z value of 0cm and an approximate maximum value of 40cm, 30cm, and 30cm respectively. However, the actual 3-D trajectory on the plot did not follow the actual path the IMU was subjected to.

## Discussion

---

This section of the report discusses the results collected from their corresponding methods outlined in sections 2, 3, and 4.

### 6.1 IMU Orientation Results

#### 6.1.1 Accelerometer Orientation Results

The testing around the accelerometer method showed that the use of the LPF on the raw accelerometer data was extremely successful with removing noise from the results during both high and low vibration situations. Whilst this method was accurate when measuring roll ( $1.95^\circ$  average error), the method had a significant drawback when pitching the IMU outside of the  $\pm 90^\circ$  range, resulting in an average error of  $56.38^\circ$ . This was due to the accelerometer pitch value approaching  $0^\circ$  when the actual pitch value approached  $180^\circ$ . This is due a limitation within the equation (3.13) used to calculate the pitch values from the accelerometer. When the IMU is at  $0^\circ$  of pitch, the acceleration in the X direction is 0 when the IMU is stationary, therefore, with the numerator at 0, the resulting pitch value corresponds to  $0^\circ$  of pitch. As the IMU pitches towards  $90^\circ$ , the Z acceleration component tends to 0 and X acceleration component tends towards g (9.81), resulting in the calculated pitch value tending towards  $90^\circ$ . As the IMU is pitched beyond this point the reverse occurs and the calculated pitch tends towards  $0^\circ$  as the magnitude of the X acceleration component reduces and Z acceleration increases, highlighting a flaw with this pitch calculation.

#### 6.1.2 Gyroscope Orientation Results

As predicted, the gyroscope performed successfully when recording all Euler angles with a quick response to sudden changes. However, since the gyroscope is prone to drifting, this had a significant impact on the results, this is ultimately caused by the integration used to determine these Euler angles and a compound error present, significantly affecting the accuracy of long-term results. This method produced an average error across all Euler angles of  $1.93^\circ$  during short-term testing.

#### 6.1.3 Magnetometer Orientation Results

When calculating the yaw from the magnetometer and using the pitch and roll values from the gyroscope, desirable results were achieved. The method to determine the yaw was responsive to changes and provided accurate results, with an average absolute error of  $2.03^\circ$ . However, as previously stated, this method was incredibly prone to electromagnetic noise, significantly impacting the output results. In addition, the equations to calculate the yaw rely on the pitch and roll values, therefore, any changes in these effected the yaw value significantly.

#### 6.1.4 Complementary Filter Orientation Result

When fusing the different methods to calculate the orientation through the implementation of the complementary filter, results were significantly improved since this method solved numerous issues that were inherent in the other methods. When the IMU was pitched past the  $90$  and  $-90^\circ$  range, the system did not experience the same issues present in the accelerometer results shown in Figure 5.7, as it was using output pitch data from the gyroscope that did not encounter this issue. Issues with yaw values being affected by IMU roll and pitch were also removed using the gyroscope. The system was also unaffected by electromagnetic interference and mechanical noise whilst remaining responsive to immediate orientation change. The effect of drift in data was also reduced, where the drift of the final orientation data was significantly lower than the results shown in Figure 5.11. The results for this method produced an average error across all Euler angles of  $1.35^\circ$ , which is extremely positive as it is  $0.58^\circ$  more accurate than the standalone gyroscope method. However, this design experienced gimbal lock when visualising the real-time orientation in 3-D space, where  $180^\circ$  in actual pitch produced an output of  $180^\circ$  in yaw. The drift in the output data was also apparent when collecting these results as the output was very unstable after a prolonged period of time.

### 6.1.5 Quaternion Orientation Results

As predicted, this method was extremely successful. The output was not prone to noise, drift or electromagnetic interference, whilst remaining sensitive to orientation change. However, it did experience limitations with the pitch results, like that in the accelerometer pitch testing. This is due to the conversion used from quaternions to Euler angles using equation (3.23), however, this issue was not present when visualising the orientation of the IMU in Figure 5.27. The overall experience when rendering the real-time 3-D orientation of the IMU was smooth and responsive, resulting in a successful test.

## 6.2 IMU Position Results

For the position derivation results using both Euler and quaternion rotation matrix methods, the final 3-D position plots produced did not accurately represent the path of which the IMU had travelled. The Euler method was significantly more inaccurate compared with the quaternion results as the maximum values for the X, Y and Z positions were incorrect by 15cm, 20cm and 28.5cm. However, whilst the plotted path was not representative of the 'cube' path taken, the maximum Y and Z positions recorded for the quaternion method were within the 30cm range, while the maximum X value was approximately 40cm (10cm greater than the actual maximum).

The likely cause for the significant error within the Euler method is due to a fluctuating drifting orientation data. Since the method is reliant on the orientation calculations, any changes in this data can cause the position of the IMU to be incorrect, these fluctuations are represented in the oscillations in the trajectory plot that aren't present in the quaternion data.

Also, when reviewing the .csv data for this experiment the total system calibration was at a register value of 3 (calibrated), however, this dropped off instantly to 0 (uncalibrated) once the IMU was translated, the same was apparent for the accelerometer calibration (shown in Figure 6.1). This is likely the cause for the incorrect 3-D position plot for both methods since the position derivation integrates the acceleration data from the accelerometer twice to obtain position (Figure 3.8), if this data is slightly incorrect, the derived position will have significant error. To correct for this, an additional BNO055 IMU was purchased to ensure it was not a hardware error, and the same issue with calibration values occurred, meaning the robustness of the position detection design could not be validated.

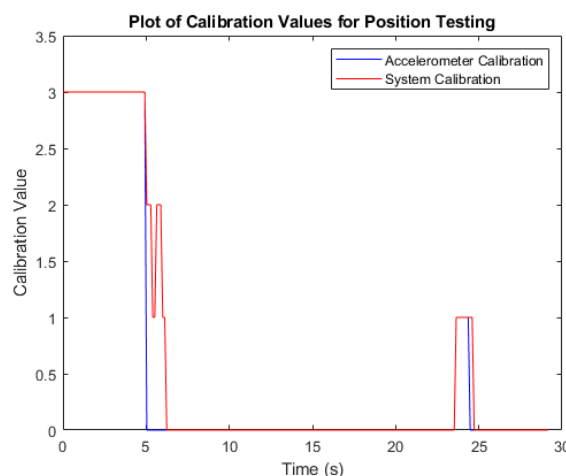


Figure 6.1: IMU accelerometer and system calibration values during the position testing using the quaternion data

### 6.3 Testing Setup

Whilst the orientation testing setup measured the actual and recorded IMU orientation values, it had some limitations and drawbacks that likely introduced error within the results. Since the actual IMU Euler angles were measured using a protractor and 'human eye', this possessed an uncertainty of  $\pm 0.5^\circ$  which can significantly alter the accuracy of these methods to measure orientation. Similar to the limitations with the orientation testing method, the accuracy of the IMU position calculation is likely effected by the inaccuracies present in the testing setup shown in Figure 3.12.

### 6.4 Project Aims and Objectives

This section reviews the overall success of the project in relation to the project aims outlined at the start of the report in Table 1.1.

Table 6.1: Review of project aims and objectives

Aim No.	Name	Description	Achieved
1	Calibration	System can be calibrated easily during use to ensure output data is correct	Somewhat
2	Data Acquisition	Data is recorded live from the system to provide relevant data with determining position in 3-D space	Yes
3	Accuracy	Position data is accurate to $\pm 0.10\text{m}$	No
4	Reliability	System performs reliably over an extended period with no significant error with the output data	Somewhat
5	Infrastructure	Minimal infrastructure required to allow the system to function and collect relevant data	Yes
6	Cost	Project cost remains under the allocated project budget	Yes
7	Safety	Use of LV across the system to prevent any risk to health	Yes

- Calibration:** IMU element of the system was calibrated with ease as shown in the results, Figure 5.1. However, since the UWB element of the system was not tested, calibration testing was not completed, so the project aim was not fully achieved.
- Data Acquisition:** position data and other supporting data (orientation) was collected using the IMU, therefore achieves the project aim.
- Accuracy:** 3-D position data was inaccurate with tracking the system trajectory during testing, therefore does not achieve the project aim.
- Reliability:** using the quaternion data, the orientation values were accurate over an extended period of time during testing, however, the position data was inaccurate (likely due to the IMU calibration issue), 3-D position testing was not reliable, therefore the project aim was not fully achieved.
- Infrastructure:** proof-of-concept design only requires the use of four UWB modules and one IMU which have small footprints and no additional mounts or stands to setup, therefore achieves the project aim.
- Cost:** overall, the project remained under budget by £29.10, therefore achieves the project aim. Further costing breakdown is presented in Table 8.9 in Appendix A.
- Safety:** complete system was designed using 3.3V (LV) which causes no risk to the user, therefore achieves the project aim.

## Conclusion and Future Work

---

### 7.1 Conclusion

This project proposes a proof-of-concept design to localise an object in 3-D space, with the aim to implement the system into a lacrosse ball to enhance the growth and safety within the sport. Giving teams and athletes the opportunity to review performance will increase the level at which the sport is played, enhancing the viewership experience. Having access to trajectory data provides broadcasters with the ability to improve viewer immersion, further growing the sport globally. Most importantly, data can be used by sports protection manufacturers to better safeguard players of the sport. Whilst this project is aimed at the sport of lacrosse, there are a plethora of other use cases where such data is desirable.

The proposed system utilised an IMU and UWB sensor to determine the position of the ball in space. To achieve this, the orientation of the ball was required to be calculated using the IMU data, where the system achieved an average error of  $1.35^\circ$  in all orientations. The system also visualised the orientation of the IMU through a real-time 3-D animation to compare to a set of reference axes, supporting with the validation of the system design. Using this orientation data and rotation matrices, the IMU's local acceleration was converted to the global coordinate system, allowing for position to be derived. The final proposed solution to determine the orientation was through using quaternion data as it was the most reliable method explored. When using this data to derive the position of the system in 3-D space, the maximum limits of the results remained within a  $\pm 10\text{cm}$  tolerance, however, had limitations with accurately tracking the actual IMU translations due to system calibration issues with the accelerometer.

### 7.2 Future Work

This project proposes a proof-of-concept design for position tracking in 3-D space. Based on the limitations and areas for improvement there is scope to develop and improve this design in future work. The following are areas considered for development to produce a more robust position tracking system.

- **The design and manufacture of a bespoke testing jig:** Rather than recording actual orientation values through the use of a protractor, a custom jig can be produced to reduce any human error to ensure accuracy testing results are correct and true, allowing for consistency across all tests. The same can also be done for the position testing to better validate the system design during position testing.
- **High speed and long range testing:** All testing conducted within the project was over a short distance and low speed which is not representative of the practical use case that the system would be subjected to, for example a lacrosse game. Conducting these tests helps to better understand limitations within the design through the results collected, therefore, identifying areas for improvement.
- **Environmental testing:** Testing the system in different conditions with varying temperature, wind speed, and humidity would better validate the design since these conditions will be present in the practical use case of this product. These tests will also determine the reliability and robustness when exposed to such conditions, better informing design decisions when selecting particular elements of the design.
- **Improved code efficiency:** Due to the limitations with the current design's code, the real-time position of the IMU in space could not be tracked, and position data had to be calculated from a pre-recorded data-set. In practice the system should track position live and therefore, should the system be optimised, live data analytics should be made possible.

- **Purchase UWB compatible microcontroller:** Should the makerfabs ESP32 UWB microcontroller have been purchased at the start of the project, greater resource time could have been dedicated to the trilateration method for position detection, therefore, allowing for testing to be conducted and design validated. For future work, a microcontroller supported by the UWB sensor should be used.
- **Alternative IMU:** To investigate into the calibration issue experienced during this project's testing and results, other IMU options should be explored.
- **Bespoke PCB:** To support with the first stage of integrating the system into a lacrosse ball, the system should be significantly reduced in size. One method to do so is through the use of smaller electronic components. This can be achieved through the design and development of custom PCBs (for the IMU, UWB and microcontroller).

## Bibliography

---

- [1] S. M. R. LLP., "Sports analytics market, a \$16.5 billion industry by 2030 with a cagr of 22.9 % - strategic market research," Available online: <https://www.globenewswire.com/en/news-release/2022/05/27/2452062/0/en/Sports-Analytics-Market-a-16-5-billion-Industry-by-2030-with-a-CAGR-of-22-9-Strategic-Market-Research.html>, 2022, [Accessed: May 02, 2023].
- [2] M. Potts, "How does hawk-eye work at wimbledon 2022?" Available online: <https://www.radiotimes.com/tv/sport/tennis/wimbledon-hawk-eye/>, 2022, [Accessed: May 02, 2023].
- [3] G. M. Arastey, "Impact of data analysis and technology in rugby union," *Sport Performance Analysis*, 2020. [Online]. Available: <https://www.sportperformanceanalysis.com/article/data-analysis-and-technology-in-rugby-union>
- [4] KINEXON, "Kinexon becomes world's first fifa preferred provider live player ball tracking," Available online: <https://kinexon.com/blog/fifa-preferred-provider-live-player-and-ball-tracking/>, 2022, [Accessed: Feb 25, 2023].
- [5] C. C. Z. L. A. M. J. . V. K. R. Vincent, H. K., "Shooting motion in high school, collegiate, and professional men's lacrosse players," *Sports biomechanics*, vol. 4, no. 14, p. 448–458, 2015. [Online]. Available: <https://doi.org/10.1080/14763141.2015.1084034>
- [6] PLL, "Lyle leads cannons over waterdogs, 16-10," Available online: <https://premierlacrosseleague.com/articles/lyle-leads-cannons-over-waterdogs-16-10>, 2022, [Accessed: Feb 25, 2023].
- [7] R. Comstock, D. Arakkal, A. T. Pierpoint, L. A. Fields, and S. K., "Are high school girls' lacrosse players at increased risk of concussion because they are not allowed to wear the same helmet boys' lacrosse players are required to wear?" *Injury Epidemiology*, vol. 7, no. 18, 2020.
- [8] B. Maron, J. Doerer, T. Haas, N. Estes, J. Hodges, and M. Link, "Commotio cordis and the epidemiology of sudden death in competitive lacrosse," *Pediatrics*, vol. 124, no. 3, pp. 966–971, 2009, pMID: 19706581.
- [9] J. Williamson, "Where are radar guns used in baseball? understanding the use of radar guns in the mlb and beyond," Available online: <https://tbonesbaseball.com/where-are-radar-guns-used-in-baseball-understanding-the-use-of-radar-guns-in-the-mlb-and-beyond/>, 2023, [Accessed: Feb 25, 2023].
- [10] E. Britannica, "determining the course of an aircraft," Available online: <https://www.britannica.com/technology/navigation-technology/Dead-reckoning>, 1994, [Accessed: May 02, 2023].
- [11] F. Franceschini, M. Galetto, D. Maisano, L. Mastrogiacomo, and B. Pralio, *Evaluation of Measurement Uncertainty*, 2011, pp. 189–219.
- [12] W. Wu, M. Xu, Q. Liang, L. Mei, and Y. Peng, "Multi-camera 3d ball tracking framework for sports video," *IET Image Processing*, vol. 14, no. 15, p. 3751–3761, 2020.
- [13] M. Bertoni, S. Michieletto, R. Oboe, and G. Michieletto, "Indoor visual-based localization system for multi-rotor uavs," *Sensors*, vol. 22, no. 15, p. 5798, 2022.
- [14] I. Toy, A. Durdu, and A. Yusefi, "Improved dead reckoning localization using imu sensor," in *2022 International Symposium on Electronics and Telecommunications (ISETC)*, 2022, pp. 1–5.
- [15] C. Yu, T.-Y. Huang, and H.-P. Ma, "Motion analysis of football kick based on an imu sensor," *Sensors*, vol. 22, p. 6244, 08 2022.

- [16] K. Merry and P. Bettinger, “Smartphone gps accuracy study in an urban environment,” *PLOS ONE*, vol. 14, no. 7, 2019. [Online]. Available: <https://www.ncbi.nlm.nih.gov/pmc/articles/PMC6638960/>
- [17] V. C. Drosos and C. Malesios, “Measuring the accuracy and precision of the garmin gps positioning in forested areas: A case study in taxiarchis-vrastama university forest,” *Journal of Environmental Science and Engineering B*, vol. 1, no. 4, 2012.
- [18] A. Poulose and D. S. Han, “Uwb indoor localization using deep learning lstm networks,” *Applied Sciences*, vol. 10, no. 18, 2020. [Online]. Available: <https://www.mdpi.com/2076-3417/10/18/6290>
- [19] H. Zhang, Q. Wang, C. Yan, J. Xu, and B. Zhang, “Research on uwb indoor positioning algorithm under the influence of human occlusion and spatial nlos,” *Remote Sensing*, vol. 14, no. 24, 2022. [Online]. Available: <https://www.mdpi.com/2072-4292/14/24/6338>
- [20] “Esp32-s3-devkitc-1 v1.1.” [Online]. Available: <https://docs.espressif.com/projects/esp-idf/en/latest/esp32s3/hw-reference/esp32s3/user-guide-devkitc-1.html>
- [21] M. Electronics, “Bosch bno055 intelligent 9-axis absolute sensor,” Available online: <https://www.mouser.co.uk/new/bosch/bosch-bno055-sensor/>, 2014, [Accessed: April 17, 2023].
- [22] M. Bognash and S. F. Asokanthan, “Stochastic stability of a class of mems-based vibratory gyroscopes under input rate fluctuations,” *Vibration*, vol. 1, no. 1, pp. 69–80, 2018. [Online]. Available: <https://www.mdpi.com/2571-631X/1/1/6>
- [23] Sparkfun, “What is a gyroscope,” Available online: <https://learn.sparkfun.com/tutorials/gyroscope/all>, [Accessed: April 17, 2023].
- [24] “What is an inertial measurement unit?” [Online]. Available: <https://www.vectornav.com/resources/inertial-navigation-articles/what-is-an-inertial-measurement-unit-imu>
- [25] Pdf, “Accelerometer and gyroscopes sensors: Operation, sensing, and applications.” [Online]. Available: <https://www.analog.com/jp/technical-articles/accelerometer-and-gyroscopes-sensors-operation-sensing-and-applications.html>
- [26] D. Vasquez, “Wireless zero-power ferromagnetic mems magnetometer,” 05 2023.
- [27] “Mikroe - 6DOF IMU 12 Click,” <https://www.mikroe.com/6dof-imu-12-click>, accessed: May 18, 2023.
- [28] “Adafruit 9-DOF Absolute Orientation IMU Fusion Breakout - BNO055,” <https://www.mouser.co.uk/ProductDetail/Adafruit/4646>, accessed: May 18, 2023.
- [29] B. Friebel, M. Schweins, N. Dreyer, and T. Kürner, “Simulation of gps localisation based on ray tracing,” *Advances in Radio Science*, vol. 19, pp. 85–92, 12 2021.
- [30] H. Parwana and M. Kothari, “Quaternions and attitude representation,” Aug 2017. [Online]. Available: <https://arxiv.org/abs/1708.08680>
- [31] W. R. Hamilton, “Vi. on quaternions; or on a new system of imaginaries in algebra,” *The London, Edinburgh, and Dublin Philosophical Magazine and Journal of Science*, vol. 29, no. 191, p. 26–31, 1846.
- [32] J. A. Farrell, *Aided navigation GPS with high rate sensors*. McGraw-Hill, 2008.
- [33] M. Pedley, “Tilt sensing using a three-axis accelerometer.” [Online]. Available: <https://www.nxp.com/files-static/sensors/doc/appnote/AN3461.pdf>

- [34] M. Caruso, “Applications of magnetic sensors for low cost compass systems,” *IEEE 2000. Position Location and Navigation Symposium (Cat. No.00CH37062)*.
- [35] M. Yoon, “A magnetometer-based complementary filter for small multi-rotor helicopters,” *International Journal of Engineering Research amp; Technology (IJERT)*, vol. 5, no. 9, Sep 2016. [Online]. Available: <https://www.ijert.org/research/a-magnetometer-based-complementary-filter-for-small-multi-rotor-helicopters-IJERTV5IS090288.pdf>
- [36] H. Chudá, “Universal approach to derivation of quaternion rotation formulas,” *MATEC Web of Conferences*, vol. 292, p. 01060, 01 2019.
- [37] M. Navarro, S. Prior, and M. Najar, “Low complexity frequency domain toa estimation for ir-uwb communications,” 10 2006, pp. 1 – 5.
- [38] S. L. Swamy, “I am the speed of light c, you ‘see’ ....!” *European Journal Of Physics Education*, vol. 5, no. 1, p. 51, 2013.
- [39] P. Sedlacek, P. Masek, and M. Slanina, “An overview of the ieee 802.15.4z standard and its comparison to the existing uwb standards,” 04 2019.
- [40] M. S. Utter, “Indoor positioning using ultra-wideband technology,” 2015.
- [41] H. Seo and H. Kim, “Four anchor sensor nodes based localization algorithm over three-dimensional space,” *Journal of information and communication convergence engineering*, vol. 10, 12 2012.
- [42] [Online]. Available: [https://static1.squarespace.com/english+rules+2019+\(final\).pdf](https://static1.squarespace.com/english+rules+2019+(final).pdf)
- [43] A. Jiménez and F. Seco, “Comparing ubisense, bespoon, and decawave uwb location systems: Indoor performance analysis,” *IEEE Transactions on Instrumentation and Measurement*, vol. PP, pp. 1–12, 04 2017.
- [44] M. Delamare, R. Boutteau, X. Savatier, and N. Iriart, “Static and dynamic evaluation of an uwb localization system for industrial applications,” *Sci*, vol. 1, p. 62, 10 2019.
- [45] [Online]. Available: <https://www.qorvo.com/products/p/DWM3000>
- [46] T. Polonelli, S. Schlapfer, and M. Magno, “Performance comparison between decawave dw1000 and dw3000 in low-power double side ranging applications,” *2022 IEEE Sensors Applications Symposium (SAS)*, 2022.
- [47] “ESP32 UWB DW3000,” <https://www.makerfabs.com/esp32-uwb-dw3000.html>, accessed: May 18, 2023.
- [48] “RS Components,” <https://uk.rs-online.com/web/p/communication-wireless-development-tools/2162643>, accessed: May 18, 2023.
- [49] “Mikroe - UWB Click,” <https://www.mikroe.com/uwb-click>, accessed: May 18, 2023.

## Appendix

---

### Appendix A: Project Testing Plans and Project Cost

Table 8.1: Testing Plans

Test Name	Test Description	Test Aims
Full System Calibration	Follow the steps outlined in the section 3.3 and observe the values for each calibration register	Ensure the system can be calibrated easily to provide accurate and reliable output data

Table 8.2: IMU Accelerometer Testing Plan

Test Name	Test Description	Test Aims
Raw Pitch and Roll (-90° to 90°)	<ol style="list-style-type: none"> <li>1. Place the IMU flat on a surface</li> <li>2. Gradually pitch the IMU to +90° and return to 0°</li> <li>3. Gradually pitch the IMU to -90° and return to 0°</li> <li>4. Repeat this process for roll</li> <li>5. Vibrate the IMU in roll and pitch axes</li> </ol>	Record raw orientation values from the accelerometer and observe the effect of noise on the outputs.
Raw Pitch and Roll Response	<ol style="list-style-type: none"> <li>1. Place the IMU flat on a surface</li> <li>2. Pitch the IMU instantaneously to +90° and return instantaneously to 0°</li> <li>3. Pitch the IMU instantaneously to -90° and return instantaneously to 0°</li> <li>4. Repeat this process for roll</li> </ol>	Observe the response time of the accelerometer to sudden changes in orientation.
Filtered Pitch and Roll	<ol style="list-style-type: none"> <li>1. Use filtered accelerometer data</li> <li>2. Place the IMU flat on a surface</li> <li>3. Gradually pitch the IMU to +90° and return to 0°</li> <li>4. Gradually pitch the IMU to -90° and return to 0°</li> <li>5. Repeat this process for roll</li> <li>6. Vibrate the IMU in roll and pitch axes</li> </ol>	Observe the effectiveness of a LPF on the accelerometer orientation output and compare it to the raw data (pre-filtering).
Pitch and Roll Accuracy	<ol style="list-style-type: none"> <li>1. Place the IMU at -135°, -90°, -45°, 0°, 45°, 90°, 135°, and 180° in pitch and record the readings from the serial plotter</li> <li>2. Calculate the absolute error (difference between the actual and recorded pitch)</li> <li>3. Plot the absolute error against the actual pitch values</li> <li>4. Repeat steps 1, 2, and 3 for IMU roll</li> </ol>	Record the accuracy of the accelerometer's method to determine pitch and roll values.

Table 8.3: IMU Gyroscope Testing Plan

Test Name	Test Description	Test Aims
Raw Pitch, Roll and Yaw (-180° to 180°)	<ol style="list-style-type: none"> <li>1. Place the IMU flat on a surface</li> <li>2. Gradually pitch the IMU to +180° and return to 0°</li> <li>3. Gradually pitch the IMU to -180° and return to 0°</li> <li>4. Instantaneously alter the IMU's pitch</li> <li>5. Repeat this process for roll and yaw</li> </ol>	Record raw orientation values from the gyroscope and observe the response time to sudden changes in orientation.
Drift Observation	<ol style="list-style-type: none"> <li>1. Place the IMU flat on a surface</li> <li>2. Perform a sudden combination of changes roll, pitch, and yaw IMU angles</li> <li>3. Place IMU flat on a surface</li> </ol>	Observe the effect of drift on the gyroscope orientation data following a combination of orientation changes.
Pitch, Roll and Yaw Accuracy	<ol style="list-style-type: none"> <li>1. Place the IMU at -135°, -90°, -45°, 0°, 45°, 90°, 135°, and 180° in pitch and record the readings from the serial plotter</li> <li>2. Calculate the absolute error (difference between the actual and recorded pitch)</li> <li>3. Plot the absolute error against the actual pitch values</li> <li>4. Repeat steps 1, 2, and 3 for IMU roll and yaw</li> </ol>	Record the accuracy of the gyroscope's method to determine pitch, roll and yaw values.

Table 8.4: IMU Magnetometer Testing Plan

Test Name	Test Description	Test Aims
Raw Yaw from Magnetometer (with Gyroscope Pitch and Roll) (-180° to 180°)	<ol style="list-style-type: none"> <li>1. Place the IMU flat on a surface</li> <li>2. Gradually yaw the IMU to +180° and return to 0°</li> <li>3. Gradually pitch the IMU to -180° and return to 0°</li> <li>4. Instantaneously alter the IMU's yaw</li> </ol>	Record raw yaw values from the magnetometer and gyroscope combination, and observe the response time to sudden changes in orientation.
Raw Yaw from Magnetometer with changing Gyroscope Pitch and Roll	<ol style="list-style-type: none"> <li>1. Place the IMU flat on a surface</li> <li>2. Alter roll and pitch values and observe changes in the recorded yaw</li> </ol>	Observe the effect of pitch and roll on the magnetometer yaw values.
Effect of Electromagnetic Interference on Magnetometer Yaw Values	<ol style="list-style-type: none"> <li>1. Place the IMU flat on a surface</li> <li>2. Move an electronic device towards and away from the IMU and observe the effect on recorded yaw values</li> </ol>	Observe the effect of electromagnetic interference on the magnetometer yaw values.
Magnetometer Yaw Accuracy	<ol style="list-style-type: none"> <li>1. Place the IMU at -135°, -90°, -45°, 0°, 45°, 90°, 135°, and 180° in yaw and record the readings from the serial plotter</li> <li>2. Calculate the absolute error (difference between the actual and recorded yaw)</li> <li>3. Plot the absolute error against the actual yaw values</li> </ol>	Record the accuracy of the magnetometer's method to determine yaw values.

Table 8.5: IMU Complementary Filter Testing Plan

Test Name	Test Description	Test Aims
Roll, Pitch, and Yaw from IMU Complementary Filter	<ol style="list-style-type: none"> <li>1. Place the IMU flat on a surface</li> <li>2. Gradually pitch the IMU to +90° and return to 0°</li> <li>3. Gradually pitch the IMU to -90° and return to 0°</li> <li>4. Repeat steps 2 and 3 for both roll and yaw</li> <li>5. Gradually pitch the IMU to -180° and return to 0°</li> <li>6. Gradually pitch the IMU to +180° and return to 0°</li> <li>7. Repeat steps 5 and 6 for both roll and yaw</li> <li>8. Rapidly alter the IMU orientation</li> <li>9. Place the IMU at rest on a flat surface</li> </ol>	Record roll, pitch, and yaw values from the IMU complementary filter, observe the response time to sudden changes in orientation, and determine the effect of gyroscope drift on the output data.
Roll, Pitch, and Yaw Accuracy from IMU Complementary Filter	<ol style="list-style-type: none"> <li>1. Place the IMU at -135°, -90°, -45°, 0°, 45°, 90°, 135°, and 180° in pitch and record the readings from the serial plotter</li> <li>2. Calculate the absolute error (difference between the actual and recorded pitch)</li> <li>3. Plot the absolute error against the actual pitch values</li> <li>4. Repeat these steps for both roll and yaw values</li> </ol>	Determine the accuracy of recorded pitch, roll, and yaw values from the IMU complementary filter.
3-D Visualisation of Actual IMU Orientation from Complementary Filter Data	<ol style="list-style-type: none"> <li>1. Run the IMU orientation visualisation code</li> <li>2. Place the IMU on a flat surface</li> <li>3. Roll the IMU at 90°, 180°, and -90° and observe the 3D animation</li> <li>4. Repeat steps 2 and 3 for pitch and yaw rotations</li> <li>5. Pitch, roll and yaw the IMU at 45° and -45° and observe the 3D animation</li> </ol>	Visualise the IMU's orientation in 3-D space to determine the accuracy and speed at which the animation responds to change.

Table 8.6: IMU Quaternion Testing Plan

Test Name	Test Description	Test Aims
Raw Pitch, Roll and Yaw (-180° to 180°)	<ol style="list-style-type: none"> <li>1. Place the IMU flat on a surface</li> <li>2. Gradually pitch the IMU to +90° and return to 0°</li> <li>3. Gradually pitch the IMU to -90° and return to 0°</li> <li>4. Gradually pitch the IMU to +180° and return to 0°</li> <li>5. Gradually pitch the IMU to -180° and return to 0°</li> <li>6. Instantaneously alter the IMU's pitch and yaw</li> <li>7. Repeat this process for roll and yaw</li> </ol>	Record orientation values from the IMU using quaternions and observe the response time to sudden changes in orientation.
Pitch, Roll and Yaw Accuracy	<ol style="list-style-type: none"> <li>1. Place the IMU at -135°, -90°, -45°, 0°, 45°, 90°, 135°, and 180° in pitch and record the readings from the serial plotter</li> <li>2. Calculate the absolute error (difference between the actual and recorded pitch)</li> <li>3. Plot the absolute error against the actual pitch values</li> <li>4. Repeat steps 1, 2, and 3 for IMU roll and yaw</li> </ol>	Record the accuracy of the quaternion method to determine pitch, roll and yaw values.
3-D Visualisation of Actual IMU Orientation from Quaternion Data	<ol style="list-style-type: none"> <li>1. Run the IMU orientation visualisation code</li> <li>2. Place the IMU on a flat surface</li> <li>3. Roll the IMU at 90°, 180°, and -90° and observe the 3D animation</li> <li>4. Repeat steps 2 and 3 for pitch and yaw rotations</li> <li>5. Pitch, roll and yaw the IMU at 45° and -45° and observe the 3D animation</li> </ol>	Visualise the IMU's orientation in 3-D space to determine the accuracy and speed at which the animation responds to change.

Table 8.7: IMU Position Testing Plan

Test Name	Test Description	Test Aims
Euler Position Testing: 30cmx30cmx30cm	<ol style="list-style-type: none"> <li>1. Record the output data in the form of .csv data from eulerPosTestCSV.ino file</li> <li>2. Place the IMU at (0,0,0)</li> <li>3. Gradually move the IMU to (30,0,0)</li> <li>4. Gradually move the IMU to (30,30,0)</li> <li>5. Gradually move the IMU to (0,30,0)</li> <li>6. Gradually move the IMU back to (0,0,0)</li> <li>7. Gradually move the IMU to (0,0,30)</li> <li>8. Gradually move the IMU to (30,0,30)</li> <li>9. Gradually move the IMU to (30,30,30)</li> <li>10. Gradually move the IMU to (0,30,0)</li> <li>11. Gradually move the IMU to (0,0,30)</li> <li>12. Finally, gradually move and place the IMU at rest to (0,0,0) to conclude the test</li> </ol>	Record IMU 3-D position values from the Euler method to observe the accuracy of the output data.
Quaternion Position Testing: 30cmx30cmx30cm	<ol style="list-style-type: none"> <li>1. Record the output data in the form of .csv data from quatPosTestCSV.ino file</li> <li>2. Place the IMU at (0,0,0)</li> <li>3. Gradually move the IMU to (30,0,0)</li> <li>4. Gradually move the IMU to (30,30,0)</li> <li>5. Gradually move the IMU to (0,30,0)</li> <li>6. Gradually move the IMU back to (0,0,0)</li> <li>7. Gradually move the IMU to (0,0,30)</li> <li>8. Gradually move the IMU to (30,0,30)</li> <li>9. Gradually move the IMU to (30,30,30)</li> <li>10. Gradually move the IMU to (0,30,0)</li> <li>11. Gradually move the IMU to (0,0,30)</li> <li>12. Finally, gradually move and place the IMU at rest to (0,0,0) to conclude the test</li> </ol>	Record IMU 3-D position values from the quaternion method to observe the accuracy of the output data.

Table 8.8: IMU Position Testing Plan

Test Name	Test Description	Test Aims
Euler Position Testing: 30cmx30cmx30cm	<ol style="list-style-type: none"> <li>1. Record the output data in the form of .csv data from eulerPosTestCSV.ino file</li> <li>2. Place the IMU at (0,0,0)</li> <li>3. Gradually move the IMU to (30,0,0)</li> <li>4. Gradually move the IMU to (30,30,0)</li> <li>5. Gradually move the IMU to (0,30,0)</li> <li>6. Gradually move the IMU back to (0,0,0)</li> <li>7. Gradually move the IMU to (0,0,30)</li> <li>8. Gradually move the IMU to (30,0,30)</li> <li>9. Gradually move the IMU to (30,30,30)</li> <li>10. Gradually move the IMU to (0,30,0)</li> <li>11. Gradually move the IMU to (0,0,30)</li> <li>12. Finally, gradually move and place the IMU at rest to (0,0,0) to conclude the test</li> </ol>	Record IMU 3-D position values from the Euler method to observe the accuracy of the output data.
Quaternion Position Testing: 30cmx30cmx30cm	<ol style="list-style-type: none"> <li>1. Record the output data in the form of .csv data from quatPosTestCSV.ino file</li> <li>2. Place the IMU at (0,0,0)</li> <li>3. Gradually move the IMU to (30,0,0)</li> <li>4. Gradually move the IMU to (30,30,0)</li> <li>5. Gradually move the IMU to (0,30,0)</li> <li>6. Gradually move the IMU back to (0,0,0)</li> <li>7. Gradually move the IMU to (0,0,30)</li> <li>8. Gradually move the IMU to (30,0,30)</li> <li>9. Gradually move the IMU to (30,30,30)</li> <li>10. Gradually move the IMU to (0,30,0)</li> <li>11. Gradually move the IMU to (0,0,30)</li> <li>12. Finally, gradually move and place the IMU at rest to (0,0,0) to conclude the test</li> </ol>	Record IMU 3-D position values from the quaternion method to observe the accuracy of the output data.

Table 8.9: Project Costing Table

<b>Item</b>	<b>Quantity</b>	<b>Cost</b>	<b>Total Cost</b>
Adafruit BNO055 IMU	2	£ 24.77	£ 49.54
ESP32-S3-DevKitC	4	£ 12.41	£ 49.64
DWM3000EVB	4	£ 28.04	£ 112.16
USB A to Male Micro USB B Cable	4	£ 2.39	£ 9.56
		<b>Total Cost</b>	<b>£ 220.90</b>
		<b>Remaining Budget</b>	<b>£ 29.10</b>